Theoretical characterization of point defects in semiconductors : from photovoltaics to quantum engineering applications

Sameer Gupta

▶ **To cite this version:**

Sameer Gupta. Theoretical characterization of point defects in semiconductors : from photovoltaics to quantum engineering applications. Material chemistry. Université Grenoble Alpes [2020-..], 2023. English. NNT : 2023GRALY030 . tel-04166887

HAL Id: tel-04166887
https://theses.hal.science/tel-04166887

Submitted on 20 Jul 2023

HAL is a multi-disciplinary open access archive for the deposit and dissemination of scientific research documents, whether they are published or not. The documents may come from teaching and research institutions in France or abroad, or from public or private research centers.

L'archive ouverte pluridisciplinaire **HAL**, est destinée au dépôt et à la diffusion de documents scientifiques de niveau recherche, publiés ou non, émanant des établissements d'enseignement et de recherche français ou étrangers, des laboratoires publics ou privés.

THÈSE

Pour obtenir le grade de

DOCTEUR DE L'UNIVERSITÉ GRENOBLE ALPES

École doctorale : PHYS - Physique
Spécialité : Physique des matériaux
Unité de recherche : Modélisation et Exploration des Matériaux

Caractérisation théorique des défauts ponctuels dans les semi-conducteurs : du photovoltaïque aux applications d'ingénierie quantique

Theoretical characterization of point defects in semiconductors : from photovoltaics to quantum engineering applications

Présentée par :

SAMEER GUPTA

Direction de thèse :

Pascal POCHET DIRECTEUR DE RECHERCHE, Université Grenoble Alpes	Directeur de thèse
Damien CALISTE INGENIEUR DOCTEUR, Université Grenoble Alpes	Co-encadrant de thèse

Rapporteurs :

GUIDO ROMA
Directeur de recherche, CEA CENTRE DE PARIS-SACLAY
LAURENT PIZZAGALLI
Directeur de recherche, CNRS CENTRE LIMOUSIN POITOU-CHARENTES

Thèse soutenue publiquement le **31 mars 2023**, devant le jury composé de :

NOEL JAKSE Professeur des Universités, GRENOBLE INP	Président
LAURENT RUBALD Ingénieur HDR, LYNRED	Examinateur
MICHELE AMATO Maître de conférences, UNIVERSITE PARIS-SACLAY	Examinateur
GUIDO ROMA Directeur de recherche, CEA CENTRE DE PARIS-SACLAY	Rapporteur
LAURENT PIZZAGALLI Directeur de recherche, CNRS CENTRE LIMOUSIN POITOU-CHARENTES	Rapporteur

THEORETICAL CHARACTERIZATION OF POINT DEFECTS IN SEMICONDUCTORS: FROM PHOTOVOLTAICS TO QUANTUM ENGINEERING APPLICATIONS

SAMEER GUPTA

A thesis submitted for partial fulfilment of the

degree of Doctor of Philosophy

Dedicated to my parents

"There is no special ingredient. To make something special, you just have to believe it's special."

– Kung Fu Panda Movie

Abstract

Les défauts ponctuels jouent un rôle essentiel dans les applications technologiques des semi-conducteurs, en fournissant des conditions de dopage appropriées. Dans le même temps, les défauts présentant des caractéristiques de piégeage des porteurs peuvent s'avérer préjudiciables aux performances et aux rendements des dispositifs à l'état solide. En raison de leurs implications sur les semi-conducteurs, en particulier sur les propriétés électroniques et optiques, les défauts ont fait l'objet de recherches approfondies au cours des dernières décennies.

Dans cette thèse, les impuretés ajoutées intentionnellement dans le tellurure de cadmium (CdTe) et leur interaction avec les défauts natifs ont été étudiées en utilisant des méthodes basées sur les premiers principes de thermodynamique. Le CdTe a plusieurs applications technologiques, telles que les cellules solaires, les détecteurs de radiation nucléaire, et la spectroscopie astronomique. Les propriétés du CdTe sont étudiées depuis plusieurs décennies. Cependant, le rôle des défauts dans le processus de croissance, pour le photovoltaïque et d'autres applications, évolue encore avec une meilleure compréhension des propriétés des défauts natifs et la connaissance des stratégies de dopage et d'alliage.

Les deux principaux sujets abordés dans cette thèse sont liés au matériau CdTe, pour le photovoltaïque et pour ses possibles applications dans le domaine quantique.

Le premier concerne la stratégie de conception de cellules solaires en CdTe polycristallin impliquant l'utilisation de selenium (Se), qui a permis d'augmenter l'efficacité des dispositifs en CdTe en couches minces à plus de 22 %. En termes de physique des défauts, les études expérimentales ont permis d'élucider le fait que l'atome de Se diffuse dans le CdTe massif et passive les pièges à porteurs intrinsèques qui y sont présents. La découverte du mécanisme de diffusion du dopant Se est très importante pour comprendre le profil en profondeur du dopant et le mécanisme de passivation des défauts natifs. Nous avons utilisé les calculs DFT basés sur les premiers principes pour identifier un mécanisme unique en deux étapes expliquant la diffusion du Se dans le CdTe massif.

Le processus de diffusion implique l'interaction du Se avec un Te interstitiel et permet la diffusion dans toutes les directions du Te interstitiel dans le CdTe massif. La barrière associée à la diffusion du Se a été calculée comme étant inférieure à 0,42 eV, reflétant la diffusion rapide du dopant Se dans le CdTe. Dans l'étape suivante, nous avons utilisé la trajectoire de diffusion du Se pour comprendre l'interaction du dopant avec les défauts natifs qui agissent comme pièges à porteurs, la lacune de Cd, et l'antisite de Te, ainsi que leur passivation, et la formation de complexes entre le Se et les défauts.

Les défauts ponctuels, en plus de leur forte implication dans les propriétés opto-électroniques des semi-conducteurs, ont également prouvé leur pertinence, ces dernières années, pour les applications quantiques telles que l'informatique et la détection. Les métaux de transition insérés dans des nanostructures semi-conductrices avec un spin localisé caractéristique, sont apparus comme des candidats appropriés pour ces applications, donnant lieu à un domaine émergent : la solotronique. Dans la deuxième partie de la thèse, nous avons étudié la structure électronique de défauts isolés de métaux de transition Cr et Mn dans le CdTe. Nous avons identifié l'effet du couplage électron-réseau sur la symétrie locale des dopants dans le réseau et établi sa correspondance avec la fonction d'onde électronique des défauts localisés. En utilisant l'énergie de liaison thermodynamique associée à l'interaction entre le dopant et les défauts natifs, calculée en DFT , nous établissons ensuite qu'il est difficile d'obtenir une configuration isolée du dopant Cr dans les nanostructures de CdTe car il se lie fortement aux défauts natifs. En revanche, le Mn, dans des conditions de croissance appropriées, peut être facilement obtenu dans une configuration isolée. Nous avons également proposé un modèle phénoménologique pour définir l'interaction des dopants de métaux de transition avec les défauts natifs. Enfin, nous avons expliqué le changement observé expérimentalement dans l'état de spin du Cr par rapport à la configuration de l'état fondamental du dopant isolé en utilisant l'interaction du Cr avec un défaut natif dans le CdTe.

Ensemble, ces deux études démontrent que la compréhension du mécanisme sous-jacent à l'échelle atomique peut être utilisée pour définir les phénomènes caractérisés expérimentalement à l'échelle macroscopique et concevoir des stratégies de croissance.

Point defects play an essential role in the technological applications of semiconductors, providing suitable doping conditions. At the same time, defects with carrier trap characteristics can prove to be detrimental to the performance and efficiencies of solid-state devices. Due to their implications on semiconductors, especially electronics and optical properties, defects have been the subject of extensive research for the last several decades.

In this thesis, intentionally added impurities in Cadmium Telluride (CdTe) and their interaction with native defects have been studied using first principles based methods. CdTe has several technological applications, such as solar cells, nuclear radiation detectors, and astronomical spectroscopy. The properties of CdTe have been studied for several decades. However, the growth process related to defects composition, for photovoltaics and other applications is still evolving with a better understanding of native defect properties and the knowledge of doping and alloying strategies.

The two main topics addressed in this thesis are related to CdTe photovoltaics and possible quantum application. The first one deals with the design strategy involving the alloying of polycrystalline CdTe solar cells with Se, which has pushed the efficiency of thin film CdTe devices above 22 %. In terms of defect physics, experimental studies have elucidated that the Se atom diffuses into CdTe bulk and passivates the intrinsic carrier traps present therein. Finding the Se dopant diffusion mechanism holds significant importance for understanding the depth profile of the dopant and native defect passivation mechanism. We have used the first principles based DFT calculations to identify a unique two-step mechanism to define the Se diffusion in the CdTe bulk. The diffusion process involves the interaction of Se with the Te self interstitial and the enhancement of Te interstitial diffusion in the CdTe bulk. The barrier associated with the Se diffusion was calculated to be lower than 0.42 eV, reflecting the fast diffusion of the Se dopant in CdTe. In the next stage, we used the Se diffusion trajectory to understand the interaction of the dopant with the carrier trap native defects, Cd vacancy, and Te antisite, and their passivation on interaction forming bound defect complexes with Se.

Point defects, along with their strong implication for opto-electronic properties of semiconductors, have also proven their suitability for quantum applications such as computing and sensing in recent years. Transition metal doped into semiconductor nanostructures with characteristic localized spin have emerged to be a suitable candidate for these applications, giving rise to the emerging field of solotronics. In the second part of the thesis, we studied the electronic structure of transition metal Cr and Mn solitary dopant defects in CdTe. We identified the effect of electron-lattice coupling on the local symmetry of the dopants in the lattice and established its correspondence with localized defect electronic wavefunction. Using DFT calculations of the thermodynamic binding

energy associated with dopant and native defects interaction, we then establish that achieving Cr isolated dopant configuration in CdTe nanostructures is challenging as it binds strongly with native defects. In contrast, Mn in suitable growth conditions can be readily obtained in an isolated configuration. We also proposed a phenomenological model to define the interaction of transition metal dopants with native defects. Finally, we explained the experimentally observed change in the spin state of Cr from that of the isolated dopant ground state configuration using the interaction of Cr with a native defect in CdTe.

Together these two studies demonstrate that understanding the underlying mechanism at the atomic scale can be used to define experimentally characterized phenomena at the macroscopic scale and devise growth strategies.

Acknowledgement

First and foremost, I would like to express my sincere gratitude to my supervisors Dr. Pascal Pochet and Dr. Damien Caliste. I sincerely thank Pascal for his unwavering guidance and encouragement throughout this journey. His expertise, coupled with his patience, motivation, and enthusiasm, significantly influenced the direction of my thesis and has instilled in me the skills and mindset of an independent researcher. I extend my heartfelt thanks to Damien for his unwavering support during challenging times. His guidance and motivation were instrumental in overcoming obstacles and maintaining my focus throughout the four years of my thesis. His presence and patient mentorship not only improved my research outcomes but also instilled in me the resilience and determination necessary to succeed in academia.

With utmost gratitude, I would like to thank the jury members of my thesis defense: Prof. Noel Jakse, Dr. Laurent Rubalodo, Dr. Michele Amato, Dr. Guido Roma, and Prof. Laurent Pizzagalli for their insightful discussion, valuable comments, and challenging questions. I want to thank them for taking the time and effort to evaluate this work. I would also like to thank my year-end evaluation CSI committee members Dr. Emmanuel Hadji, Dr. Alessandro Cresti, and Dr. Jing Li for their useful advice, feedback, discussions, and exciting questions which helped me to improve my communication and critical approach.

I am very thankful to our experimental collaborators Dr. Lucien Besmobes and Dr. Hervé Boukari for providing me with the opportunity to work with them. I would like to thank them and Dr. Vivekananda Tiwari for all the fruitful discussions and for helping me understand our calculations results better. I would also like to thank all other members of the ANR Mechaspin project for the fruitful discussions and sharing their knowledge.

I would like to thank ANR for funding my Ph.D. scholarship through the ANR Mechaspin project. This Ph.D. work would not have been possible without their financial support.

I would like to express sincere thanks to Dr. Selva for all his help and long scientific discussions on the projects on which we worked together during my Ph.D., especially on Se defects in CdTe. I would also like to thank him for helping me to improve my data analysis skills and for his invaluable input to my research. I am grateful to him for always being very supportive of my work.

I would like to extend my heartfelt appreciation and gratitude to my labmates, Lucila, Samuel, Camilo, Julia, Augustin, and Kajal, for their invaluable contributions to my research journey. Their unwavering support, engaging discussions, and the friendly environment they fostered in the lab made my experience truly enriching and memorable. In particular, I would like to express a special thanks to Lucila, Samuel, and Julia for the captivating conversations we shared during our lunch and coffee breaks. I also thank all other members of the L_Sim lab for their valuable contribution and support, in particular, Thierry Deutsch, Luigi Genovese, and Ivan Duchemin. I am also thankful to all the poles and services, administrative or technical from the CEA Grenoble.

I consider myself incredibly fortunate to have found great friends during my time in Grenoble. I would like to express my heartfelt gratitude to Sambit, Kaushik, Ankush, Namanu, Ranjith, Aashutosh, Ranjana, Martin, Louis, Sarvanan, Gosia, and Jhouben for the countless memories we have created together and for their unwavering support. They truly made my life in Grenoble an extraordinary and cherished experience that I will always hold close to my heart.

I would like to express my deepest gratitude to Dr. Ehesan Ali from INST Mohali and Dr. Debabrata Mishra from the University of Delhi for their unwavering support, motivation, and invaluable guidance throughout my research journey. Their mentorship has been instrumental in laying the strong foundation of my scientific career, and I am truly grateful for their assistance.

I extend my thanks to my friends from INST Mohali, Ashima, Aashish, Kalyani, Prabhleen, Aritra, Shikha, Rishu and Munish, and Manas from the University of Delhi for their contribution in my research journey. My special thanks goes to Dheerendra, Gaurav, Viru, Sachin, Rajesh, Amit, Vivek, Aaditya, and Avinash, who have remained as pillars of strength throughout this PhD journey and my life challenges.

Finally, I express my deep appreciation to my family members for their blessings and unconditional love. I am extremely indebted to my parents who have supported and guided me in life to follow my passion and to whom I dedicate this thesis. I thank you very much for everything and for being my strength, inspiration, and guiding light during autumn and spring alike. I want to thank my brothers and sisters, Rohit, Priyanka di, Anuradha di, and Kapil bhaiya for their constant love and support.

Lastly, I bow down to the Almighty for giving me the strength to pursue this path.

Contents

CHAPTER 1

Introduction

Semiconductors technology forms the basis of all modern electronics and is primarily based on transistors and diodes. Bardeen, Brattain, and Shockley received the Nobel prize for Physics in 1956 for building the first transistor, using the union of semiconductors containing free majority charge carriers of opposite signs[1]. The study of the physics of defects is a key aspect of understanding the physical properties of semiconductor materials. The source of point defects in materials can be intrinsic, atomic imperfections arising due to entropy, and intentionally or unintentionally introduced impurities into the crystal lattice. In semiconductor materials, point defects can impact the optical, electrical, and mechanical properties of the host material and give rise to many macroscopic properties, such as ionic, electronic, and thermal conductivity[2]. The functioning of semiconductor devices depends critically on the concentration of native defects and impurities introduced in the host lattice.

Defects can have an impact on the performance and efficiency of semiconductor functional materials used for microelectronics and photovoltaics applications. Point defects often introduce electronic levels in the band gap that can alter the position of the Fermi level. The defects that introduce electronic levels close to band edges may release extra carriers into the host and provide desired p-type and n-type conditions for the practical application of electronic devices. In contrast, the defects that introduce electronic levels deep in the band gap and localized on the defect can trap charge carriers (electrons and holes). Such defects have often a detrimental impact on the electronics and photovoltaic properties of the semiconductors, and may even pin the Fermi level

around midgap[3,4]. When the charge carriers get trapped at the defect centers, eventually, either it leads to a reduction in the carrier lifetime in the case of radiative recombination, or their disappearance due to non-radiative recombination activity. The energy released through recombination of charge carriers, in the latter case, gets accommodated into a local disruption of lattice at the defect site instead of resulting in a photon release.

The native point defects created due to entropy and the foreign element impurities introduced (unintentionally and intentionally) into a host crystal lattice increase its energy and thus have an associated activation energy required for their formation. The point defects also have a characteristic diffusion activation energy, which facilitates their migration to the surface of the crystal or allows them to recombine with the complementary defect to restore the local order at the lattice site. In the case of impurities, this diffusion characteristic allows their migration in the host lattice and to take up a substitutional site or to interact with native defects present in the crystal. Semiconductors are usually grown at high temperatures and intentional impurities are either introduced at these elevated temperatures or through high-energy processes like implantation. Therefore there is always a considerable possibility that impurity atoms interact with native defects and form bound complexes, in the case the activation energy of the defect complex favors so.

The defect complex has different properties than the compositional defects. Therefore, intentionally added foreign impurities can interact with unwanted native defects to passivate them. In opposition to this, unwanted defect complex formation can result in a decrease in the concentration of needed isolated defects. This can be a source of a challenge when a particular isolated configuration of a point defect is desired for a functional material.

The host native point defects are also responsible for the diffusion of impurities and the self-diffusion of component elements in the host bulk lattice. The migration of a substitutional impurity from one regular site to an adjacent site requires a high activation energy. Therefore, the migration of dopants is carried by vacancy and interstitial defects. The dopant migration is desirable to achieve the target profile in the host. At the same time, migration at room temperature with a very low activation barrier is undesirable as it can contribute to instability in the semiconductor device. The dopant diffusion mechanism is driven by intrinsic defects. Therefore it is necessary to understand the diffusion of the intrinsic defects present in the host lattice. This requires the knowledge of the intrinsic defects ground state, metastable states configurations, and the associated migration barrier. Self-interstitial defects have particularly shown to play an important role in dopant diffusion in the case of II-VI semiconductors.

Identifying a probable diffusion mechanism for dopants requires the identification

of the defect which acts as the driver of the dopant diffusion. Theoretical investigations of the defect complex formed by the native defects and dopants and the associated diffusion barrier can address the question regarding the dominant dopant (defect complex) migration process.

The first problem that we have addressed in this thesis is related to photovoltaic applications. In thin film solar cells, native defects play a very significant role in the working efficiency of the device. Native defects with carrier trap characteristics can reduce the concentration of photo-generated charge carriers and reduce their lifetime. Doping (and alloying) strategies involving the introduction of large concentrations of impurities can help in the passivation of the carrier traps through defect complex formation or shifting host band edges position. We specifically address the role of Selenium (Se) alloying of CdTe. Indeed, for the CdTe solar cell application, an improvement in efficiency from 17 to over 22 percent was achieved by the formation of $CdSe_xTe_{1-x}$ alloy[5]. Photoluminescence and experiments tracing the Se diffusion profile pointed to a 60 - 80 % reduction in the non-radiative recombination activity (defects) in both grain boundaries and CdTe interior grain on alloying with Se[6]. Direct interaction of Se with harmful native defects such as Cd vacancy and Te-antisite was proposed as the most probable reason for the decrease in non-radiative recombination[6]. However, the detailed underlying mechanism at the atomic scale was missing when we started our work.

The second addressed problem is related to quantum applications. Indeed, point defects present in semiconductors are also emerging as candidates for such applications[7]. The change in optical and electronic activity brought by the isolated point defects in semiconductor materials can be used for quantum sensing, communication, and computation[7–9]. The defect systems can demonstrate a large spin coherence time and single photon emission. Moreover, the spin associated with point defects can be manipulated using external stimuli with a great degree of control[9]. While it is challenging to isolate point defects hosted in a semiconductor crystal lattice from the surrounding matrix, using magnetic dopants inserted into semiconductor nanostructures has shown reproducible quantum properties and stability[7] and can provide a platform for a two-level energy system for quantum applications. This has been particularly shown for Mn in II-VI and III-V semiconductor quantum dots (QDs) through optical excitation and photo-luminescence probe[10,11]. Alongside, in the case of II-VI semiconductor QDs, Cr doping has also been shown to provide unique functionalities such as large spin-to-strain coupling[12,13]. In this second part of the thesis, we have focused on Mn and Cr dopants in the CdTe host for the study of ground-state electronic structure and their interaction with native defects.

Several experimental characterization techniques are present today, which are used to identify the point defects in semiconductors and the associated phenomena, such as the migration of dopants. Cathodoluminescence and Photoluminescence spectroscopy are used to study the optical signature, Deep level transient spectroscopy (DLTS), and temperature-dependent Hall measurement provide the knowledge of the electrical character and Electron paramagnetic resonance has been used to study the symmetry and hyperfine structure of point defects and impurities[14]. Experimentally, the diffusion mechanism of dopants is analyzed using the concentration profile, with techniques such as secondary ion mass spectroscopy (SIMS)[15]. All these methods have been successfully used to characterize the point defects in terms of associated physical properties. But they do not provide the full microscopic detail of the point defect and the associated phenomenon at the atomic scale.

In contrast, the first principles methods allows the study of individual defects in semiconductors and the identification of their atomistic and electronic structure with a high level of accuracy. The various phenomena, such as the electronic activity of defects and diffusion, can be understood at this microscopic scale. First principles methods, therefore, provide the ability to compare the computational results with the experimentally observed phenomenon and act as an analysis tool and a prediction tool in some instances as well.

1.1 Outline of thesis

This thesis work discusses the structural, energetic, and electronic properties of native defects and intentionally added Se, Cr, and Mn impurities (dopants) in CdTe. The main focus of the first part of the work is on the Se dopant diffusion mechanism and its interaction with native defects. The second part of the thesis deals with the interaction of Chromium (Cr) and Manganese (Mn) dopants with the CdTe native defects. A comprehensive understanding of native defects' electronic structure is required to study such interactions. Therefore a detailed description of native defects is provided. The results are obtained using *ab - initio* calculations based on density functional theory.

The work is organized in the following manner. In **Chapter 2**, we begin with a discussion of concepts related to point defects in semiconductors, such as the electronic states introduced by the defects in the band gap, the difference between shallow and deep character, and the role of defects in doping. The chapter ends with a brief description of the experimental characterization techniques used for the point defects in semiconductors.

In **Chapter 3**, a detailed review of the theoretical and computational quantum mechanics methods that form the base for our simulations is presented, covering major aspects related to Density Functional Theory (DFT) approach. In the second part of the chapter, we discussed the physical properties of the defects that can be calculated using DFT with reasonable accuracies, such as the formation energy, defects migration barrier, defect complex binding energy, and charge transition level. We concluded the chapter with a discussion on symmetry and Jahn-Teller distortion in point defects.

In **Chapter 4**, we have addressed the question related to the presence of Se impurity in the CdTe host bulk lattice. We begin with a discussion on the choice of our supercell size and DFT exchange-correlation functional used for calculating point defects and defect complexes' electronic structure, with Cd vacancy as the model case. We then discussed the electronic structure of native defects (Cd-vacancy, Te-antisite, and Te-interstitial) corresponding to the Te-rich limit growth conditions in detail. In the second part, we present a detailed analysis of the mechanism of Te self-diffusion and Se diffusion in the CdTe host lattice. In the final part of the chapter, using the Se diffusion defect trajectory, we studied the interaction of Se impurity with the major native defects present in Te-rich conditions in the CdTe host. Based on the calculated results, we provided a comprehensive explanation of the hybrid role played by Se in the alloyed $CdSe_xTe_{1-x}$ solar cells that have an efficiency of over 22%. The results presented in this chapter are published in Appl. Phys. Lett. **119**, 062105 (2021).

In the **Chapter 5**, we describe our investigation of Cr and Mn dopants in the CdTe host lattice. We present our interpretation of the local symmetry of the lattice around these impurities using the interaction of the transition metal Cr and Mn 3d- orbitals with the host lattice tetrahedral crystal field. In the second part, we present a detailed analysis of the interaction of Cr and Mn impurities with CdTe major native defects corresponding to both Te-rich and Cd-rich conditions. We have provided a detailed analysis of such interaction in terms of native defects electronic states and impurity 3d-orbitals. In the last part, we present the implications of these interactions on the impurity behavior and ground state electronic structure and related observed phenomenon by our experimentalist collaborators at Institut Neel located in CNRS, Grenoble. A small part of the results presented in this chapter is published in Phys. Rev. B **104**, L041301 (2021).

Finally, in **Chapter 6**, we present the summary of the results and discuss future perspectives in relation to our analysis of the interaction of dopants with native point defects in CdTe for solar cells and quantum applications.

CHAPTER 2

State of Art

2.1 Point defects in Semiconductors

The material scientist Colin Humphrey once stated about crystal defects that *"Crystals are like people: it is the defects in them that tends to make them interesting."* This statement stands true and is central to semiconductor physics, as it is defects that play a pivotal role in their application.

The Thermodynamics principle makes it impossible to produce a crystal with perfect atomic structure at finite temperature due to the competing effect of ordering (enthalpy) and disordering (entropy) forces. Therefore crystal growth is always accompanied by the formation of a certain amount of imperfections or defects of some sort. These imperfections are unavoidable even in cases where a highly developed fabrication process is already in place to produce high-purity crystals. As a result of entropy, defect concentration in a crystal is dependent on the temperature and can be expressed through a Boltzmann relation:

$$n = Ne^{-\Delta H_f / k_B T} \tag{2.1}$$

where N is the number of available sites in crystal, ΔH_f is the defect formation energy, k_B is the Boltzmann constant, and T is the temperature. The equation 2.1 suggests that the lower the formation energy, the higher the concentration of the defect will be in the crystal. The defect formation energy can be calculated using the first principle-based

calculations and the value for significant defects lies typically below 4 eV.

The point defects critically impact the electrical, optical, and mechanical properties of semiconductors. Alongside the native defects created in a crystal lattice due to entropy, inadvertent impurity point defects can also form during the growth process by foreign element atoms. These unintentional impurities can limit and negatively impact the performance of semiconductor devices. Growth processes are usually highly optimized to achieve high-purity semiconductors to avoid such imperfections. In contrast, impurities are also intentionally added to the semiconductors during the growth process to engineer and induce unique electrical, optical, and even magnetic properties, such foreign element atoms are called dopants. This thesis is mainly focused on the dopant defects intentionally introduced in the CdTe lattice (to improve performance and induce local magnetic anisotropy) and their interaction with native point defects. Such defects are associated particularly with one or two atoms in the crystal lattice, in contrast to extended defects, which include grain boundaries and dislocations.

Binary semiconductors, such as CdTe, have a relatively high defect density in comparison to elemental semiconductor crystals of Si and Ge, as the growth process involves more variables. The technological limitation on the part of the growth process to avoid these imperfections raised the need to search for possible ways to control and engineer the defect concentration and their impact on electrical and optical properties.

The point defects in equilibrium at the atomic scale induce local lattice distortions and electron energy levels in the semiconductor band gap that are decisive for the electron activity of the defect centers. In this section, we discuss the basic ideas regarding the point defects in semiconductors. The electronic eigenstates that appear in the crystal due to the local symmetry breaking (2.1.2), their impact on the electronic activity of the semiconductors (2.1.3), and link to the ability of point defects to generate free carriers in the host band (2.2.2).

2.1.1 Crystallographic defects

Crystalline solids are defined by characteristic symmetry with a periodic arrangement of atoms. This symmetry can be used by assuming the crystal to be made of perfectly repeating units to study associated properties employing first principle methods. However, this assumption of the perfect arrangement of lattice atoms is interrupted by naturally occurring imperfections in the crystal at atomic and mesoscopic scales, referred to as crystalline defects. The concentration of each defect in the crystal can be estimated under the thermodynamics equilibrium condition.

Crystal defects can be classified based on their dimensions as bulk defects (3D),

plane defects (2D), line defects (1D), or point defects (0D). Point defects correspond to a local imperfection in the crystal lattice, involving one or two atoms, with lattice perturbation of a few atomic sites. Primary point defects are of types: Vacancies, interstitials, and substitutions (Figure 2.1). Vacancy defects are formed in case an atom is missing/absent from a regular periodic lattice site. We will denote the vacancies as V_A, where A is the chemical identity of atomic specie absent from the lattice site. Interstitial defects represent an atom occupying a site in the host lattice, which is normally unoccupied in the regular periodic lattice. We have used the notation A_i for the interstitial of atomic species A. Substitutional defects are formed when an atom is found to replace a regular atomic site of the different atom, for e.g., impurity X substituting a Te site in CdTe lattice is denoted as X_{Te}. In the case of binary semiconductors, where a cation (anion) is found to substitute an anion (cation), it is referred to as antisite, for e.g., Te atom occupying a Cd-site in a regular CdTe lattice is referred to as Te-antisite (Te_{Cd}). Point defects can also bind to form a complex, such as in the case of a substitutional defect bind with an adjunct vacancy or interstitial defect. The case of defect complexes involving few atoms can be treated in the same formalism as point defects.

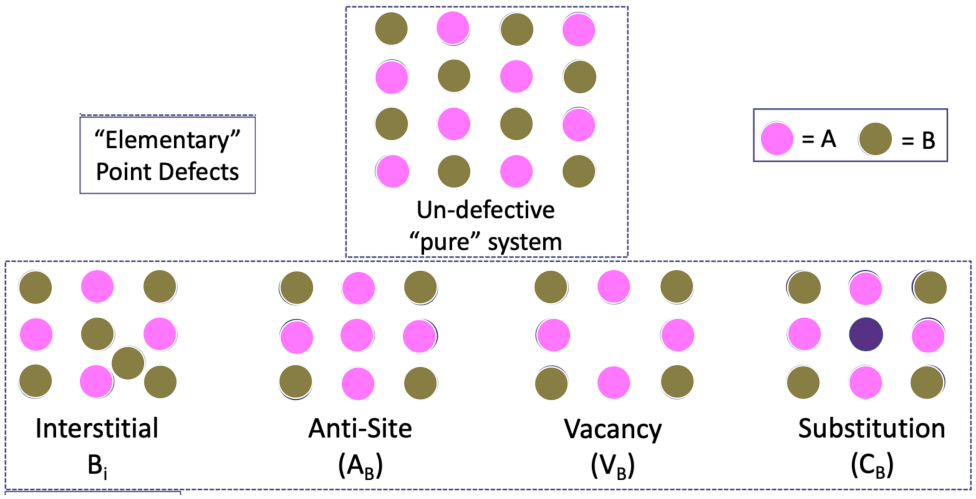

Figure 2.1: Schematic representation of common crystal point defects in AB type lattice. (a) is an interstitial vacancy, (b) is an antisite, (c) is a vacancy defect, and (d) is a substitutional defect (adapted from the the attached reference[16]).

An impurity can take up a substitutional site or be located in a position that is off from the regular periodic crystal site *i.e.* interstitial. In the case when impurities are present at an interstitial position, they are likely to be located in a position where they cause the least strain locally in the lattice. In II-VI semiconductor lattice, there are three

such interstitial sites: the two tetragonal sites, either coordinated to four group II or VI atoms, and the hexagonal site (coordinated to three atoms of each group). However, in some cases, a split interstitial configuration is also possible. In this configuration, two atoms share a common lattice site, such that a regular site atom is displaced from its initial position. In this case, electronic interaction among local defect electrons can lead to lattice distortions to accommodate these interactions and compensate for strain resulting from a split interstitial configuration.

In a compound semiconductor (AB), the degree of freedom of chemical stoichiometry, vacancy, and antisite defect concentration are highly interdependent. A slight abundance of one component element A can lead to the vacancy of other type V_B or the antisite A_B occupying the other site.

2.1.2 Point defects electronic levels

An ideal crystal lattice can be defined using a periodic arrangement of atoms extended infinitely with translation symmetry. Therefore, electrons in a crystal are subjected to a periodic potential of the form $V(r) = V(r + R)$, where R is the vector representing the periodicity of the so-called Bravais lattice. The single electron energies plotted against the wave vector form the material's band structure, where the definition of the electronic wavefunction is not unique due to symmetry and periodicity (Figure 2.2). Each eigenstate can be represented using a Bloch-like wavefunction.

Point defects result in a local disruption of the translation symmetry. Considering a vacancy defect at a position r_D in a crystal, the local periodic electron potential invariance at the defect site does not hold $V(r_D) \neq V(r_D + R)$. Therefore the wavefunction within this region of electronic potential perturbation cannot be represented using a Bloch-like eigenstate. Assuming point defects as local perturbations embedded in a crystal localized on a few atoms, they can be treated as small molecules subjected to the crystal field of the host material. Defects might induce localized defect states of molecular orbitals form, within the semiconductor band-gap or close to band edges. The corresponding wavefunction associated with the defect-induced state(s) is localized in the crystal lattice in contrast with bulk-like states (Figure 2.2).

The electronic occupation of such orbital(s) can induce atomic distortion locally at the defect site, presenting different geometry configurations and characteristic site symmetry. Experimentally it has been well established that the localized defect electronic states (densities) are strongly coupled to the lattice and can trap charge carriers accommodated in the form of local lattice distortions. The energy difference between the defect-induced states and host band edges defines the character of single particle

wavefunction of the electron(s) occupied at the defect level. A very small energy difference ($\sim k_B T$) reflects a dispersed wavefunction, whereas a sufficiently large difference ensures spatial localization on the defect site. The degree of localization is strongly dependent on defect type and the host material.

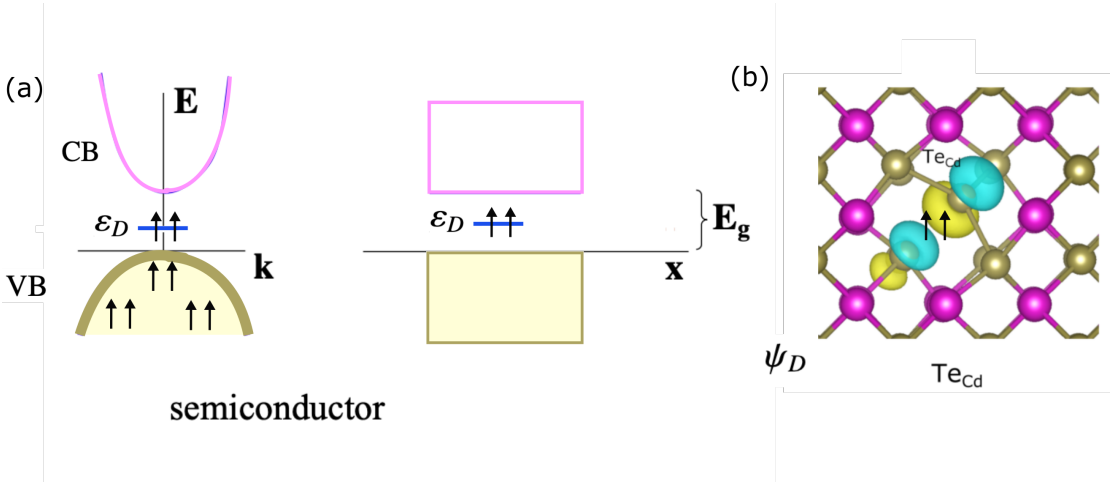

Figure 2.2: (a) Defect electronic eigenstate (ε_D) induced within a semiconductor bandgap due to the localized perturbation created by a common Te-antisite (Te_{Cd}) defect present in CdTe lattice. (b) The corresponding wavefunction (ψ_D) of the defect-induced state is shown.

We aim to understand the electronic character of defects based on simple molecular orbital approaches combined with the one-to-one comparison with point defects induced localized electronic states in the host band structure along with symmetry consideration.

2.1.3 Interaction of defects with charge carriers

Semiconductors have a characteristic gap of forbidden states separating occupied valence bands and empty conduction bands through an energy bandgap. The concentration of free charge carriers, i.e. the number of electrons present in the conduction band, n_c, and the number of holes in the valence band, p_v, at any given temperature, are the most important physical quantity of a semiconductor. The free-charge carriers in intrinsic semiconductors created through excitation by thermal energy or energy transfer from photons maintain the condition of charge neutrality ($n_c = p_v$), i.e., an equal number of electrons and holes are created in the absence of defects. This inherent symmetry between holes and electrons is problematic, since most of the semiconductor devices are

built using the components having one of the charge carrier concentrations dominant over the other ($n >> p$ or $p >> n$). The imbalance between the carrier concentration of electrons and holes is created by the presence of intrinsic defects or mainly through the introduction of a significant number of impurities (or dopants) in the host crystal.

The concentration and dynamics of free carriers in semiconductors are strongly dependent on the point defects concentration. Since, the Fermi level of the intrinsic semiconductor lies close to the mid-band-gap and thermal energy (k_BT) is insufficient to excite electrons and form charge carriers in an appreciable concentration in the absence of defects. Physically point defects introduce electronic levels in the band gap, which can capture charge carriers (electrons and holes), as shown in Figure 2.3. Defect states that lie close to the band edges can ionize readily, and the states that are present deep in the band gap can trap carriers. The charge states of defects are represented using a notation, e.g., a doubly negative charge vacancy defect of specie A with two trapped electrons can be represented as V_A^{-2}. Point defects play a central role to create charge carriers in appreciable concentration for industrial applications, e.g., in microelectronics and photovoltaics.

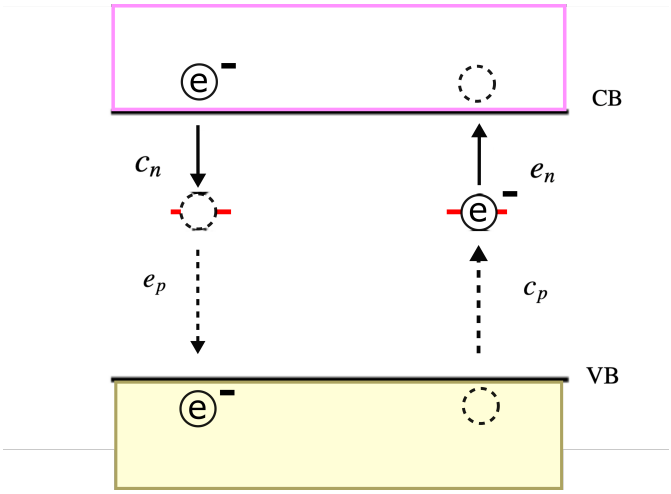

Figure 2.3: Schematic illustration of carrier capture and emission by a deep level defect-induced state. (On the left) An empty defect level can capture an electron from CB with the rate c_n and emit a hole to the VB with the rate e_p, (On the right), whereas a filled electronic level can emit an electron to the CB with the rate e_n and capture holes from VB with the rate c_p. The exchange of electrons with band edges is shown with solid arrows and that of holes with dashed arrows.

The electronic activity of the point defects is based on their ability to generate or capture charge carriers from host bulk bands in the region of lattice defined by the

defect-induced eigenstate wavefunction. The capture of the charge carrier involves the transfer of a free carrier from the valence band (VB) or conduction band (CB) to the trap electron level, ε_D, which lies within the bandgap. The impact of point defects on the concentration of free carriers can be determined using the position of the electronic level (ε_D), ionization level, electron capture cross-section (σ_n), and the hole capture cross-section (σ_p).

Not all point defects in the semiconductor host lattice are active in the sense that they induce electronic states in the forbidden band gap. The defect which introduces these electronic levels interacts with free-charge carriers and controls their concentration. Such point defects are referred to as defect centers or carrier traps.

2.1.4 Shockley Read Hall recombination

Defect-induced state(s) associated with an active character defect, impacts carrier dynamics such that when it is empty, it can capture an electron from CB with a rate of c_n or emit a hole with a rate e_p and vice versa when filled. The carrier capture rate is dependent on the character of the defect, the position of the defect-induced state with respect to band edges, the concentration of charge carriers, and temperature. The effect of the defect state on the semiconductor electronic activity is dependent on the relative magnitude of charge carriers' capture and emission rates. In the case where e_n, $e_p << c_n$, c_p, the defect may act as Shockley Read Hall (SRH) recombination centers, which are detrimental for photovoltaics applications[17,18]. In the case of c_n, $c_p << e_n$, e_p, the defect act as a carrier generation center and lead to carrier leakage issues. If the defect states mainly interact only with one of the CB or VB of the host, it will change the carriers' equilibrium concentration. The condition for a defect to act as an SRH center is most likely to be satisfied only when the defect-introduced electronic level(s) lie(s) close to the middle of the band gap so that both carrier capture rate for electron c_n and holes c_p are large enough (Figure 2.4). The successive capture of an electron and a hole at a SRH defect level results in a non-radiative recombination, contrasting to the radiative recombination in optoelectronic semiconductor devices. Therefore these defects are called deep non-radiative recombination centers.

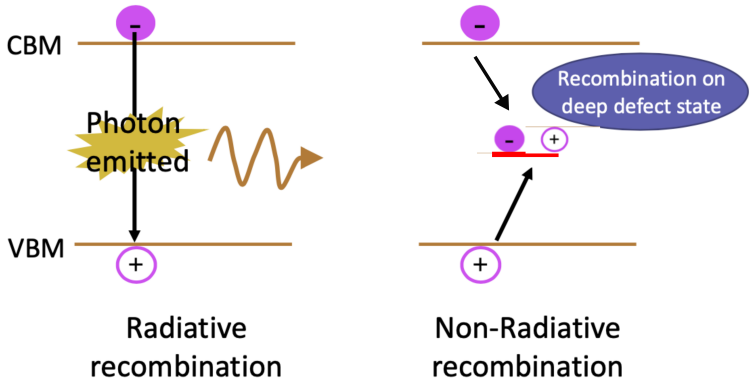

Figure 2.4: (a) Schematic representation of electron-hole recombination in an opto-electronic semiconductor device and (b) Non-radiative recombination of carriers at a deep electronic level associated with a Shockley Read Hall (SRH) recombination center (adapted from the the attached reference[16]).

2.2 Conceptualization of defects

2.2.1 Shallow vs deep centers

Point defects depending on the position of their defect electronic levels in the semiconductor band gap, can be classified as shallow and deep defects. The shallow defects introduce energy levels in the band gap located at $\sim K_BT$ (depending on band-gap or within $\sim 50\, meV$) from the bottom of the conduction band or top of the valence band.

Shallow defects can be described by hydrogen-like electrostatic potential and are often introduced intentionally into semiconductor host lattice as impurities. These intentionally added impurities are called dopants and contribute excess charge carriers to the VB and CB of the host. The shallow native defects or foreign impurities can contribute an electron to CB or trap electrons from VB. This charge carrier created by the ionized point defect will occupy a bulk-like eigenstate (Figure 2.5 (a)) that is highly delocalized (spread over a distance of tens of angstroms from the point defect). The electron or hole contributed to the host band edges by a shallow point defect is subjected to a spherical potential of (ionized) shallow defect, screened by the dielectric constant of the host material. The contributed charge carrier within the hydrogen model is considered to be weakly bound to the ionized defect with an extended effective radius (> 15Å). The hydrogen-like electrostatic potential created by the ionized dopant can be described using the following expression.

$$V(r) = -\frac{Q}{\varepsilon_r r} \tag{2.2}$$

where ε_r is the relative dielectric constant of the host material and Q the charge.

The effective radius of the wavefunction associated with the point-like shallow defects extends beyond the first and second neighbors (Figure 2.5 (c)), which can be estimated as

$$a^* = \frac{a_0 \varepsilon_r}{m^*} \tag{2.3}$$

The ε_r can be quite large due to the small band gap of semiconductors and, therefore, the potential decays in a few tens of angstroms from the impurity atom. The charge carrier contributed by the impurity to the host band should be treated as a free quasiparticle with an effective mass (m_e^* or m_h^*) rather than as a free carrier. The shallow defects are characterized by the ionization energy determined using the hydrogen model within the effective mass approximation, where quasiparticle charge carriers are defined by the binding energy of the carrier (E_b^c) with the host band such that $E_b^c << E_g$ (E_g is band-gap of host semiconductor). The ionization or charge state transition represents the transition between charge state q and $q + 1$ and is termed as $D(q + 1/q)$.

Charge carriers (electrons or holes) bound to shallow defects strongly interact with the band edges, with their wavefunction delocalized into the host lattice with respect to the position of the defect site. In contrast, deep levels cannot be described using a hydrogen-like potential and introduce highly localized defect states (Figure 2.5 (b)) with electronic wavefunction having an effective radius of 3.5 to 6.5 Å(Figure 2.5 (d)). Deep levels can originate from native defects or impurities that introduce a large disruption of the lattice at the defect site. Therefore the charge carrier can be trapped locally into the wavefunction associated with large lattice distortion. Deep defects trap the charge carriers and, therefore, potentially have a detrimental impact on the optoelectronic properties of semiconductors as they can reduce the net carrier concentration. Consequently, they can trap both electrons and holes and can also act as recombination centers. As the deep defects usually trigger large distortions of the neighboring lattice atoms, they have a characteristic optical transition signal. In some cases, deep acceptor defects can also trap holes on to the nearest neighbor anion atoms in a polaronic state. Cation site Zinc vacancy in Zinc Oxide (ZnO) is an example of such a point defect[19].

Along with defect-state electronic wavefunction and lattice distortions, shallow and deep defects are usually defined with ionization level. It takes in to account both the position of the defect electron level in the band gap and carrier capture and emission rates. The results from the first principle based calculations can be compared with

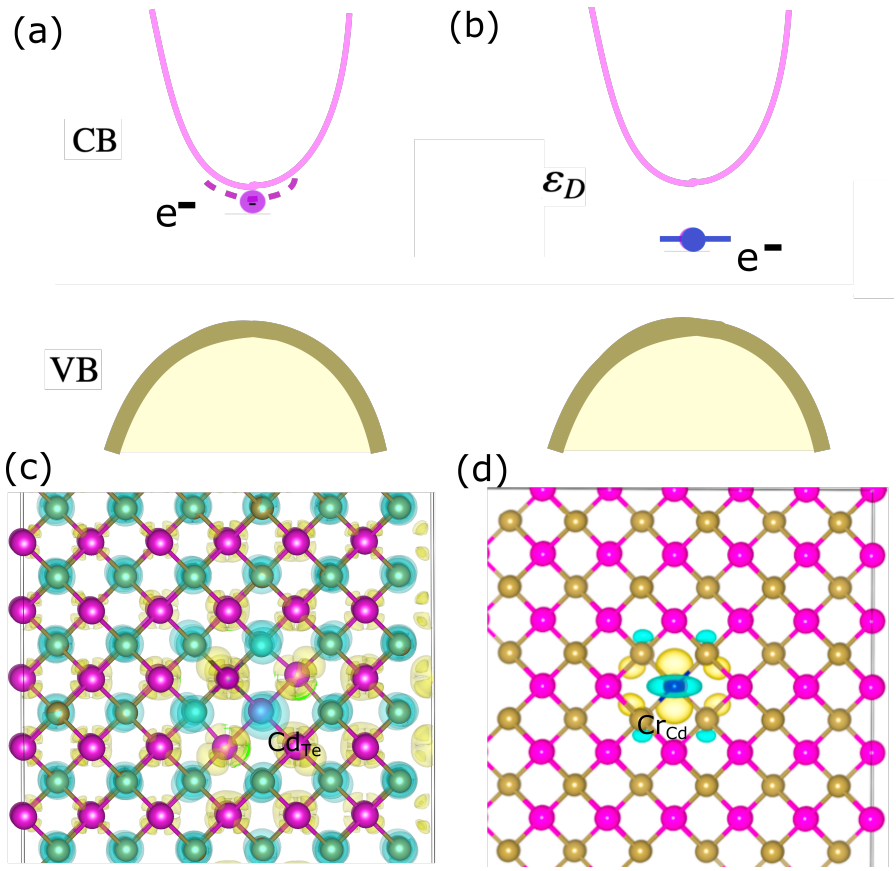

Figure 2.5: (a) Illustration of an effective-mass electron-donor defect state derived from the conduction band edge (indicated by a dotted line). (b) A defect state introduced by a deep electron donor within the band gap is indicated with a bold flat line representing strong localization. (c) An effective-mass like perturbed host state associated with a shallow defect Cd-antisite (C_{Te}) present in the CdTe lattice is shown, presenting electron density delocalized into the lattice region. (d) A localized deep defect state associated with Cr impurity in CdTe, (Cr_{Cd}) is shown, representing electron density localization at the defect site.

ionization activation energy measured from the experiments.

2.2.2 Role of defects in doping

Since the discovery of transistors in the late 1940s, semiconductors doped with impurities have remained a subject of ongoing research. The electronic properties of semiconductors can be controlled by engineering the type and concentration of impurities added to a perfect crystal to make a doped (extrinsic) crystal. The position of electron

chemical potential (μ_e) within the band gap of the semiconductor can be expressed as:

$$\mu_e^{int} = \varepsilon_v + \frac{1}{2}E_g + \frac{3}{4}k_B T ln\frac{m_h^*}{m_e^*} \tag{2.4}$$

Where ε_v is the energy position of the valence band edge, E_g is the band gap, and m_h^* and m_e^* are the effective mass of hole and conduction band electron, respectively. The effective mass of charge carriers depends on the density of states close to the host band edge. In intrinsic semiconductors (assuming the absence of native defects or very small concentration), the number of free electrons in the conduction band (n_c) is similar to the number of holes in the valence band (p_v). Therefore, the ratio of effective mass becomes, $\frac{m_h^*}{m_e^*} \simeq 1$, making the last term very small. Consequently, in this case, μ_e remains very close to the middle of the band gap.

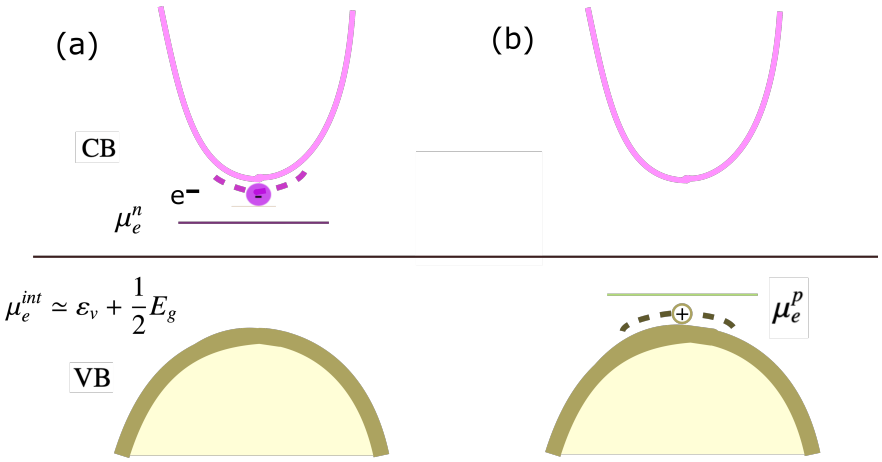

Figure 2.6: (a) Schematic representation of n-type doping condition resulting from a presence of shallow electron donor shifting the electron chemical potential (μ_e) from the initial position (μ_e^{int}) toward the conduction band (μ_e^n) and (b) n-type doping with a relative shift of μ_e towards the valence band caused by a shallow electron donor present close to the valence band.

Dopants can be classified either as electron donors or acceptors. Donor impurities introduce an occupied electronic state slightly below the conduction band edge, such that defect electrons can be excited thermally into the conduction band, creating a negatively charged quasi-particle with effective mass m_e^*. In contrast, an acceptor induces an empty state slightly above the valence band edge, and electrons can be excited to this eigenstate, leaving behind a positive charge carrier (hole) of effective mass m_h^* in the valence band. As a result of this introduction of dopants, the position of μ_e shifts from the intrinsic position towards one of the band edges (Figure 2.6). This is driven by

an increase in the concentration of one type of charge carriers (majority carriers) and a decrease in other type (minority carriers). Electron donor impurities naturally shift μ_e towards CB and acceptor impurities towards VB.

This shift in the position of μ_e towards one of the band edges can be expressed through the following expression:

$$\mu_e^{n(p)} = \varepsilon_{c(v)} + \frac{1}{2}E_g + \frac{3}{4}k_B T ln\frac{m_h^*}{m_e^*} - (+)K_B T ln\frac{N_{c(v)}}{N_{D(A)}} \tag{2.5}$$

$\mu_e^{n(p)}$ is the electron chemical potential of doped crystal, $N_{D(A)}$ is the concentration of donor (acceptor) impurities, and $N_{c(v)}$ is the effective density of states in the conduction (valence) band, dependent on the effective mass m_e^* and m_h^*.

When a large concentration of acceptors is present or introduced into a semiconductor, an appreciable population of positively charged holes is present in the valence band leading to a p-doped condition. Concurrently, an n-doped semiconductor has a large concentration of donors, leading to a high number of electrons present in the conduction band.

Native defects are always present in a semiconductor host lattice and, in many cases, can be present in a large enough concentration to impact the number of charge carriers present in the host. For *e.g.*, in the case of III-nitrides binary semiconductors, vacancy defects have very low formation energy and can lead to a large concentration of charge carriers of one type (either hole or electrons)[20]. A large concentration of native donors present in a semiconductor will make it difficult to dope the material p-type, as the donors will recombine with intentionally added acceptor impurity atoms. This is known as self-compensation. For instance, many new promising semiconductors can only be doped either p-type or n-type due to this self-compensation phenomenon[21,22]. The capacity to dope a semiconductor material is referred to as 'dopability' and is a very important issue for current and future solid-state technologies.

For an impurity atom, one can predict to some extent whether it will behave as an acceptor or donor depending on the number of valence electrons. In a II-VI semiconductor, e.g. a group III atom substituting on the cation (group II atom) site and a group VII atom on the anion (group VI) lattice site will act as donors. For native defects, it is not possible to infer in priori the character and the position of defect levels with respect to host band edges.

2.2.3 Experimental defect characterization

The impact of point defects on the material properties can be very significant at the macroscopic level and therefore, their presence is readily identified. However, the experimental characterization of the defects to know the element type and the accurate position of the corresponding electronic level in the band gap is challenging. Some of the common characterization techniques used to identify the point defects in semiconductors are quickly discussed in this section, with an emphasis on the figures that will be compared to our theoretical results in the next chapters.

Optical absorption and luminescence

Optical absorption is among the first characterization techniques that have been used to study defects in solids, employed first by R. W. Pohl to identify F-centers present in alkali halide solids[23]. The color of the sample containing defects was explained to be resulting from the absorption of visible light by electrons localized on the anion vacancy site. In the case of semiconductors, point defects with carrier trap electronic levels present in the band gap, allow the electronic excitation (induced by light absorption) or spontaneous emission of a photon (luminescence) triggered by de-excitation of electron (leading to electron-hole recombination). Consequently, in the case of deep defects with localized eigenstate wavefunction, an electronic transition between the defect state and host band edge by means of absorption may produce a measurable photocurrent. The associated optical absorption and luminescence can be used to characterize point defects with localized wavefunction present in lattice.

Electron paramagnetic resonance (EPR)

EPR is a powerful spectroscopy technique that can be used to characterize paramagnetic centers or point defects with localized unpaired electron(s), present in a perfect diamagnetic crystal[24]. It can give information about the local environment (and local defect site symmetry) present around the unpaired electron(s). This involves analyzing the relativistic interaction of the unpaired electron with an externally applied magnetic field and the surrounding nuclei. The experiment uses the absorption of a photon having energy resonant to the Zeeman energy splitting resulting from the unpaired electron(s), subjected to a static magnetic field, to identify the defect. In a more realistic model, the shift induced by the hyperfine interaction of electron and magnetic dipole is also taken into account. In this thesis, we have compared the local symmetry of point defects in CdTe, as reported from the experimental EPR results, with our ground state calcula-

tions for several native and impurity defects such as Cd vacancy, Te-antisite, Cr and Mn single impurity in CdTe.

Deep level transient spectroscopy (DLTS)

DLTS characterization technique to identify defects was first proposed by D. V. Lang in 1974[25]. DLTS allows to observe the capacity of deep defect trap levels to emit electrons at a given temperature. This then gives an estimate of the relative position of deep defect electronic level with respect to host band edges. The electronic activity of trap centers through DLTS is characterized by measuring the activation energy required for the deep defect to release an electron. This activation energy is equivalent to the binding energy of the negatively charged quasiparticle associated with a shallow donor. The technique is based on the fundamental operation of the p-n junction. A p-n junction is formed by joining p-doped and n-doped semiconductor components. The carrier traps present in the depletion region of the p-n junction can contribute to the so-called p-n junction capacitance at a given temperature. The variation in capacitance (transient capacitance) caused by the release of an electron by a deep defect is measured to find the activation energy of the carrier trap present in the p-n junction. However, the atomic scale composition of the deep defect presenting the DLTS signal is not presented by the technique. The activation energy of the deep defects can then be compared with the first principle based calculations of the ionization level of the defects present in the material to predict the defect responsible for the DLTS signal.

CHAPTER 3

Computational Methodology

3.1 The Density Functional Theory

The description of the electronic structure of both molecules and periodic solid systems requires an understanding of the behavior of nuclei, electrons, and their interaction with each other. At the atomic scale, quantum nature governs the electronic behavior and is explained using the time-dependent Schrödinger wave equation.

$$i\hbar\frac{\partial}{\partial t}\Psi(\mathbf{r},t) = -\frac{\hbar^2}{2m_e}\nabla^2\Psi(\mathbf{r},t) + V\Psi(\mathbf{r},t) \tag{3.1}$$

It is important to specify that the above equation is for a single electron. Here, $\hbar$ is Planck's constant, m_e is the mass of an electron and V is some external potential, $\Psi(\mathbf{r},t)$ is the wavefunction of the electron, where $|\Psi|^2$ defines the probability distribution of the electron. In *ab-initio* methods, concerning static state and involving T = 0 K, the time dependence part is commonly neglected, which changes equation 3.1 as follows:

$$-\frac{\hbar^2}{2m_e}\nabla^2\Psi(\mathbf{r}) + V\Psi(\mathbf{r}) = \hat{H}\Psi(\mathbf{r}) = E\Psi(\mathbf{r}) \tag{3.2}$$

Here, E is the energy eigenvalue of the electron. Therefore $\hat{H}$, the Hamiltonian operator, defines the eigenstate and energy of the electron.

3.1.1 Many body problem issues and Hartree-Fock theory

All the practical problems involve systems containing multiple electrons and nuclei, the Schrödinger equation is then defined by a so-called many-body equation

$$\hat{H}\Psi(r_1, r_2, ..., R_1, R_2, ...) = E\Psi(r_1, r_2, ..., R_1, R_2, ...) \tag{3.3}$$

where $\Psi(r_1, r_2, ..., R_1, R_2, ...)$ is the many-body wavefunction, r_i corresponds to the position of electrons and R_i is the analogous position for the i^{th} nuclei. The Hamiltonian operator $\hat{H}$ operator can be represented as the sum of the operator of kinetic energy ($\hat{T}$) and potential energy ($\hat{V}$) of the electrons (e) and nuclei (N)

$$\hat{H} = T_e(r) + T_N(R) + V_{e-e}(r) + V_{e-N}(r, R) + V_{N-N}(R) \tag{3.4}$$

These terms can be written in terms of Laplacian operator ∇^2 and coulomb interaction as in the following equation

$$\hat{H} = -\sum_{i}^{N_e} \frac{\hbar^2}{2m_e}\nabla_i^2 + \sum_{i}^{N_N} \frac{\hbar^2}{2m_I}\nabla_I^2 + \frac{1}{2}\sum_{i\neq j}^{N_e} \frac{e^2}{4\pi\varepsilon_\circ r_{ij}} - \sum_{i,I}^{N_e,N_N} \frac{e^2 Z_I}{4\pi\varepsilon_\circ R_{iI}} + \frac{1}{2}\sum_{I\neq J}^{N_N} \frac{e^2 Z_I Z_J}{4\pi\varepsilon_\circ R_{IJ}} \tag{3.5}$$

The first two terms in equation 3.5 represent the kinetic energy of the electrons and nuclei with the respective mass of m_e and m_I, defined on index i for electrons and I for nuclei, respectively. The third term represents the Coulomb interaction between i and j electrons excluding self-interaction ($i = j$). The fourth term describes electrostatic interaction between electron i and nuclei I, and the fifth term is between I and J nuclei. Nuclei have charge $+Z_I e$, where Z_I is the number of protons present in the nucleus. The third and fifth terms are factored by $1/2$ to remove the double counting of electrons and nuclei.

The exact numerical solution of the many-body Schrödinger equation is analytically not possible and computationally feasible for only a few electrons. Therefore approximations are relied up on to reduce the number of variables involved in the equation. In this section, these approximations, which have been implemented to make possible use of the first principle, Density functional theory (DFT) based calculations of complex systems, will be discussed.

The first of these is the *adiabatic approach* as assumed under the Born-Oppenheimer approximation[26]. It is based on the fact that the mass of nuclei is several orders larger than the mass of electrons. This makes the relative motion of nuclei with respect to electrons static and therefore, the dynamics of nuclei could be neglected by assuming

them as frozen with respect to electrons. This approximation thus allows to separate electronic, and nuclei wavefunction, and the total wavefunction can be written as their product.

$$\Psi = \Psi_e(r_1, r_2, ...)\Psi_N(R_1, R_2, ...) \tag{3.6}$$

Therefore the total energy of the many-body system can be written as the sum of electronic and nuclei energy.

$$E = E_{electronic} + E_{nuclei} \tag{3.7}$$

For a given ionic configuration, the many body problem reduces to

$$\hat{H}_e\Psi_e = E\Psi_e \tag{3.8}$$

with many-body Hamiltonian written as

$$\hat{H}_e = -\sum_i^{N_e} \frac{\hbar^2}{2m_e}\nabla_i^2 + \frac{1}{2}\sum_{i\neq j}^{N_e} \frac{e^2}{4\pi\varepsilon_\circ r_{ij}} - \sum_{i,I}^{N_e,N_N} \frac{e^2 Z_I}{4\pi\varepsilon_\circ R_{iI}} \tag{3.9}$$

Hartree-Fock theory

The Born-Oppenheimer approximation helps in simplifying the many-body Schrödinger equation involving nuclei and electrons to a many-body problem involving electrons only. However, there are several degrees of freedom associated with each interacting electron and their spin. The dimension of the many-body equation electronic equation are further reduced using the Hartree approximation introduced in the year 1928, which is one of the earliest proposed approaches. The most challenging part of the many-body electronic Hamiltonian is the Coulomb electron-electron interaction. The Hartree approximation allows to reduce the many-body problem to the one-electron problem. The approximation is based on the assumption that the N-body wavefunction of a system can be approximated by a product of single electron wavefunctions.

$$\Psi_{tot}(r_1, r_2, ..., r_n) = \Psi(r_1)\Psi(r_2), ..., \Psi(r_n) \tag{3.10}$$

where each of the wave functions $\Psi(r_i)$ satisfies the single electron Schrödinger equation.

The challenging part of electron-electron repulsion that makes the separation of electron coordinates and individual treatment of each electron difficult, is tackled by

expressing this interaction in an average manner. Hartree assumed that instead of calculating the coulomb repulsion terms separately for all the electron pairs, we could calculate the effective repulsion experienced by an electron due to the average field of electrons. Therefore the Hamiltonian, as a result of the Hartree approximation, is written as the sum of one electron operators:

$$\hat{H}_e = \sum_{i=1}^{N_e} f(x_i) \ , \ f(x_i) = -\frac{\hbar^2}{2m_e}\nabla_i^2 - \sum_{I}^{N_N} \frac{e^2 Z_I}{4\pi\varepsilon_\circ R_{iI}} + V^{HF}(r_i) \tag{3.11}$$

where V^{HF} is the average electrostatic potential experienced by ith electron due to all the other electrons. $f(x)$ is the one-electron operator, called the fock operator.

The Hartree-Fock (HF) potential depends up on the total wavefunction, and the solution of the wavefunction is achieved in a self-consistent field (SCF) manner. The Hartree approximation does not consider the spin of the electron explicitly, which is taken into account in the Hartree-Fock approximation. The Pauli exclusion principle considers the anti-symmetric nature of electronic wavefunction, and the Hartree-Fock total wavefunction can be expressed as an anti-symmetric product of single particle wavefunction in the form of $N \times N$ Slater determinants as

$$\Psi^e_{HF}(x_1, x_2, ...x_N) = \frac{1}{\sqrt{N!}} \begin{vmatrix} \chi_1(x_1) & \chi_2(x_1) & \cdots & \chi_N(x_1) \\ \chi_1(x_2) & \chi_2(x_2) & \cdots & \chi_N(x_2) \\ \vdots & \vdots & & \vdots \\ \chi_1(x_N) & \chi_2(x_N) & \cdots & \chi_N(x_N) \end{vmatrix} \tag{3.12}$$

Here, $\chi_i(x)$ is one-electron wavefunctions, where each of them is a function of three spatial coordinates and one spin coordinate written as $\chi_i(x) = \psi_j(r)\varsigma(s)$. The anti-symmetric nature of HF wavefunction expressed using the Slater determinant introduces some degree of correlation between electrons of the same spin, which is called exchange-correlation. However, it does not account for the correlation between electrons with opposite spins. The correlation component for both the same spin and opposite spin electrons can be approximated by an alternative method of Density functional theory (DFT), discussed in next section 3.1.3. Using the quantum mechanics variational principle, Hartree-Fock equations can be solved with the self-consistent field cycle. However, a full set of single-particle wavefunctions is still required to produce the non-local potential in the HF approach, making the treatment of solid-state problems computationally challenging. Therefore it leaves a need for an approach that significantly reduces the number of variables and takes care of electron correlation energy to enable the electronic properties calculations for larger multi-electron systems with a

high degree of accuracy.

3.1.2 Hohenberg-Kohn Theorems

A possible way to reduce the number of variables and degree of freedom is provided by Density functional theory (DFT). Hohenberg and Kohn in 1964 laid the foundation of the DFT[27]. They showed that the ground state electron density $n(r)$ is directly related through a functional (a function of function) to the total energy of the system and its physical properties. In contrast to Hartree-Fock theory which deals with many-body N electron wavefunction dependent on 3N spatial coordinated and N spin coordinates, DFT is fundamentally based on only three variables associated with electron density $n(r)$. The two Hohenberg-Kohn equations form the basis of DFT and are given as follows :

Theorem 1 *For a system of N_e interacting particles, under the influence of external potential $V_{ext}(r)$, the potential $V_{ext}(r)$ is uniquely determined by the ground state electron density $n_0(r)$ (up to an additive constant)*

Theorem 2 *Consider a functional E[n(r)] relating system energy to electron density $n(r)$, which is valid for any external potential $V_{ext}(r)$. The exact ground state energy of the system is given by the global minimum value of functional, and the corresponding electron density $n(r)$ is the exact ground state density $n_0(r)$.*

The ground state energy functional for a given external potential $V_{ext}(r)$ in terms of electron density $n(r)$ can be written as

$$E_{V_{ext}}[n(r)] = F[n(r)] + \int V_{ext} n(r) d^3r \tag{3.13}$$

Hohenberg-Kohn theorems direct that the exact solution of the many-body problem is possible only if universal functional $F[n(r)]$ is known. However, the precise form of the universal functional relating a system of interacting electrons with the energy of the system is not known; therefore raises the need for approximation. Moreover, the calculations for interacting electrons will be expensive with an approximate functional as well.

3.1.3 Kohn-Sham one particle picture

Kohn and Sham devised an approach to replace the interacting electrons system with an auxiliary non-interacting electrons system (that interacts only through an effective

potential)[28]. The key to the Kohn-Sham approach is that it requires that the auxiliary system of non-interacting electrons has the same ground-state electron density $n_0(r)$ as the interacting system. In this case, the Hohenberg & Kohn universal functional takes the form

$$F[n(r)] = T_0[n(r)] + \frac{e^2}{8\pi\varepsilon_0}\int \frac{n(r)n(r')d^3rd^3r'}{|r-r'|} + E_{xc}[n(r)] \tag{3.14}$$

where $T_0[n(r)]$ is the kinetic energy of the non-interacting particles, $E_{xc}[n(r)]$ is the so called exchange correlation energy functional. The effective potential, sensed by the interacting particles can be expressed as

$$V_{eff}(r) = V_{ext}(r) + \frac{e^2}{4\pi\varepsilon_0}\int \frac{n(r')d^3r'}{|r-r'|} + V_{xc}(r) \tag{3.15}$$

The second term on the right side of equation 3.15 describes the mean-field electrostatic interaction of non-interacting particles. The last term accounts for the many-body effect of the physical, interacting electron system. This term can be defined through the functional derivative of exchange-correlation energy functional

$$V_{xc}(r) = \frac{\delta E_{xc}[n(r)]}{\delta n(r)} \tag{3.16}$$

The minimizing electron density $n(r)$ can be obtained by solving the Kohn-Sham equations of N non-interacting particles through the variational principle

$$\left(-\frac{\hbar^2}{2m}\nabla_i^2 + V_{eff}(r)\right)\varphi(r) = \epsilon_i\varphi(r) \tag{3.17}$$

with

$$n_0(r) = \sum_i^N \mid \varphi_i^2(r) \mid \tag{3.18}$$

$n_0(r)$ is the ground state electron density, which in the one-particle picture is determined by one-particle Kohn-Sham orbitals φ_i. Kohn-Sham one-particle picture can therefore be interpreted as a single electron being subjected to a mean-field effective potential defined by the ground state electron density of the physical system. Kohn-Sham equations provide a complete solution of ground state electron density and energy of the interacting many-particle system.

3.1.4 Exchange-correlation functional

The exchange-correlation energy accounts for the following energy terms: the kinetic correlation energy, exchange energy (arising from the antisymmetry of electron wave-function), Coulombic correlation energy (associated with inter-electronic repulsions), and a self-interaction correction (SIC). Conventionally, the functional E^{XC} is expressed as the sum of exchange energy functional E^X and correlation energy functional E^C as

$$E^{XC}[\rho] = E^X[\rho] + E^C[\rho] \tag{3.19}$$

The Kohn-Sham equations allow approximation of exchange and correlation functional that are local or semi-local in character, such that effective potential depends on the electron density and its derivative. **Local density approximation (LDA)** proposed by Kohn-Sham is the simplest and most widely used approximation (in the case of crystals) to exchange and correlation energy $E_{xc}[n(r)]$, defined as

$$E_{xc}^{LDA}[n(r)] = \int e_{xc}^{unif}(n(r))n(r)d^3r \tag{3.20}$$

where $e_{xc}^{unif}(n(r))$ is the exchange-correlation energy per particle of uniform electron gas of density $n(r)$. The exchange contribution was defined using the analogy from the Thomas-Fermi approximation to the kinetic energy of the homogenous electron gas and the correlation energy was calculated from accurate Monte-Carlo calculations. The generalization of LDA for spin-polarized systems where the spin of the electrons can be considered explicitly is commonly referred to as the **local-spin-density approximation (LSDA)**[29,30].

A slight improvement over the LDA functional to account for non-uniformness in the density of physical systems was proposed by introducing the dependence on the derivatives of density through **Generalised gradient approximation (GGA)**[31]. In GGA, exchange-correlation energy is expressed as a function of the gradient of electron density

$$E_{xc}^{GGA}[n(r)] = \int f(n(r), \nabla n(r))d^3r \tag{3.21}$$

The functional proposed by Perdew, Burke, and Ernzehrof is the most commonly used GGA-based functional and is popularly known as PBE[32] and has a form

$$E_{xc}^{GGA}[n(r)] = \int e_x^{unif}(n(r))F_{xc}(n(r), \nabla n(r))d^3r \tag{3.22}$$

Exchange-correlation energy functionals based on Kohn-Sham formalism have shown

tremendous predictive power and consistently provides accurate results in various range of solid-state physics problems. However, they fail to account for the self-interaction of Kohn-Sham particles and lead to an underestimation of the semiconductor band gap.

Hybrid functionals were introduced to circumvent this problem by replacing a part of (semi)-local exchange energy with Hartree-Fock (HF) or exact exchange energy of Kohn-Sham particles. This is due to the well established fact that the total correlation has a predominant contribution from the exchange energy of electrons with the same spin. The most common of the hybrid functionals is PBE0 functional, which is based on PBE GGA functional. The exchange-correlation energy in case of PBE0[33] is written as

$$E_{xc}^{PBE0} = \alpha E_x^{HF} + (1-\alpha)E_x^{PBE} + E_c^{PBE} \tag{3.23}$$

α is the mixing parameter of HF exchange, which is most typically set as $\alpha = 1/4$ based on various physical arguments. SIC, in the case of hybrid functionals, cancels out due to the contribution from HF exchange and KS exchange energy terms.

3.1.5 Pseudopotentials

In atoms, electrons can be divided in to two categories: core electrons which are tightly bound to the nucleus, and valence electrons which are further away from the nucleus. The electronic wavefunction has a $1/r$ singularity at the position of each nucleus and oscillates rapidly close to the nuclei in the system and thus requires a large number of basis functions to model accurately. This makes all-electron calculations very computationally demanding. The core electrons are weakly affected by the electronic environment. It is generally only the valence electrons that participate in chemical bond formation and reaction, thus it is reasonable to assume that the core electrons' wavefunction remains unaffected by the electrons present in bonded atoms (when two atoms are put together).

Pseudopotential approximation is based on the key idea of considering the tightly bound core electrons as 'frozen' and replacing them with an effective (pseudo) potential, which attenuates the coulomb potential close to the nucleus, satisfying the $1/r$ singularity[35]. Pseudopotentials are built to replace/reflect the potential of the nucleus outside the sphere of a certain radius called the cut-off radius r_c, while inside that sphere, they are artificially smoothed. This helps in getting rid of the oscillation of wavefunction in regions close to nuclei while keeping a correct description of valence electrons in all other regions of space (Figure 3.1). The main advantage of the pseudopotential approximation is that it removes the orthogonality constraint on the valence electrons' wavefunction with that of the core electrons. This thus reduces the nodes in the ra-

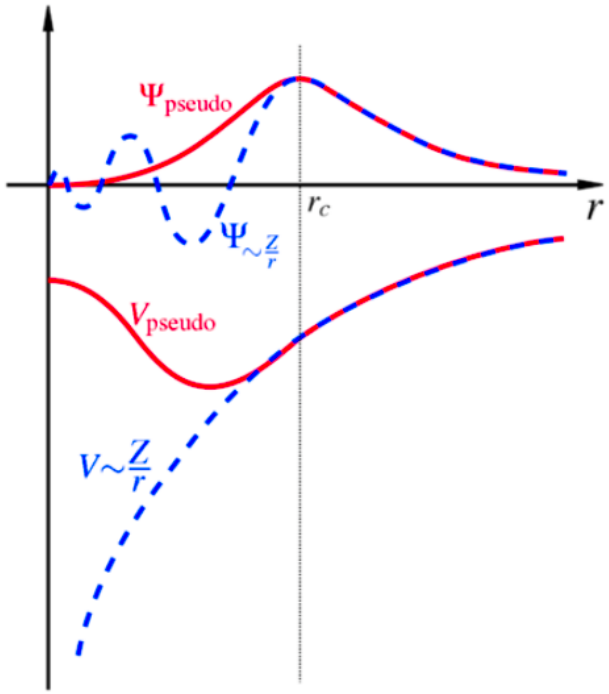

Figure 3.1: Schematic illustration of all electron potential having form $V \sim Z/r$, shown with blue color dashed curve and the pseudopotential V_{pseudo} shown with a solid red curve. The corresponding wavefunctions are shown alongside. Pseudopotential V_{pseudo} and the corresponding wavefunction reflects the all-electron potential outside of the cut-off radius r_c. The Figure is reproduced from the the attached reference[34]

dial part close to the core, being replaced by pseudo wavefunction and leading to a valence electrons wavefunction that varies smoothly in the core region by smoothing the coulomb potential to cut-off radius r_c. The relation between all electrons wavefunction and pseudo wavefunction under the pseudopotential approximation is shown in Figure 3.1. The smooth wavefunction for core electrons is computationally less demanding as it can be approximated by either a truncated basis expansion or real-space grid representation.

The pseudopotential method, therefore, considers the potential of the bare atomic nuclei plus the core electrons, taking into account the screening of nuclei by core electrons. In this manner, the many-body electron problem is now simplified to a problem dealing only with valence electrons. During the course of this thesis, all calculations were performed using norm-conserving Hartwigsen-Goedcker-Hutter potential[36]. In the so-called norm-conserving pseudopotential, the integrated electron density in the

pseudo wavefunction corresponds to the original wavefunction, and, for $r > r_c$; the pseudopotential must coincide with the original all-electrons wavefunction.

3.1.6 Geometry optimization algorithms

The total energy of a system calculated using DFT formalism depends on the atomic configuration $E^{DFT}(R_1, R_2, ..., R_N)$. The position of different nuclei, therefore, forms a potential energy surface depending on the nuclei coordinates. Identification of a stable configuration of the system of interest, which reflects the physical state and helps in studying associated properties, is important. The study of point defects involves identifying ground state (GS) and metastable configurations along with the transition state (TS) configuration associated with the minimum energy path (MEP) connecting two neighboring GS configurations.

The potential energy surface is defined as $E(\mathbf{x})$, where x is a point on the PES map corresponding to the atomic configuration defined by coordinates of nuclei $(R_1, R_2, ..., R_N)$. The shape of the PES can then be investigated to find critical points such as minima, metastable minima, and transition state (saddle point) by solving Kohn-Sham equations, starting with different initial guess configurations. For a given configuration, a self-consistent charge density is calculated using DFT. The forces on each atom are defined using the energy calculated from the electron density (equation 3.24). The ground state atomic structure (and meta-stable configurations) can be identified by using DFT to find points on the PES, such that all atomic forces are minimized and for which adjacent points on the PES are energetically less favorable.

The stable configurations present across the PES are identified using energy-minimizing optimization methods. The optimization methods can be put in to two categories. The first approach is based on the gradient of energy functional, and the second on the Hessian matrices of the double derivative of energy functional. Energy gradient methods require forces, i.e., the first order of derivative of the energy functional on atomic configurations, to be minimized. For a given atomic configuration, force on i^{th} nuclei is given as

$$F_i = \frac{-\delta E(R_1, R_2, ..., R_N)}{\delta R_i} \tag{3.24}$$

The second-order derivative of energy functional is defined using the Hessian matrix. This approach requires the terms in the Hessian matrix to be minimized. Although, the Hessian matrix based approach provides a more accurate description as they give energy value as well as the slope of the PES at a given point, they are often too computa-

tionally expensive. We have used an approach based on the gradient based optimization method in this thesis, which is described briefly in the next sub-section.

Energy Minimization algorithm

To identify the stable configuration of point defect local electronic structure on the PES, we have used an optimization method known as fast inertial relaxation engine (FIRE)[37]. The scheme relies on inertia. This method is based on a molecular dynamics approach. The trajectory of molecular dynamics (MD) optimization is evolved at each step of the self-consistent field (SCF) optimization cycle, by modification of the velocities in an energy-downhill manner. For a system of N nuclei of mass m, with coordinates $\mathbf{x} \equiv (x_1, x_2, ...x_{3N})$, the potential energy surface $E(\mathbf{x})$ only depends on the relative position of the nuclei and thus can be thought of as 3N dimension map. The equation of motion for nuclei in the system under the FIRE algorithm can be defined by a corrected acceleration given as:

$$\dot{v}(t) = F(t)/m - \gamma(t)||v(t)||[\hat{v}(t) - \hat{F}(t)] \tag{3.25}$$

here t denotes time, m is nuclei mass, $\mathbf{v}(t)$ is the velocity of the particles ($\mathbf{v}(t) = \dot{\mathbf{x}}(t)$), $F(\mathbf{x}(t))$ is the force acting on the system i.e. is the gradient of the potential energy $F(\mathbf{x}(t)) = -\nabla E(\mathbf{x}(t))$ and $\gamma(t)$ is scalar function of time. The first term of the equation 3.25, on the right side represents classical Newtonian dynamics. The second term directs the trajectory of the system at a particular $\mathbf{x}(t)$ on PES towards the steepest descent by reducing the angle between $\mathbf{v}(t)$ and $F(\mathbf{x}(t))$. The basic principle of FIRE is to perform dynamics that allow downhill motion on this map. The function $\gamma(t)$ controls the direction and acceleration of the trajectory. A global quantity referred to as power factor $P(t) = F(\mathbf{x}(t)).\mathbf{v}(t)$, which corresponds to the power delivered to the nuclei by force acting on them, is used to monitor and direct the energy minimization process. A negative value of $P(t)$ suggests the system is moving in an uphill motion on the PES map. If this occurs at a certain time step, the velocity is set to zero, and the scaling parameter $\gamma(t)$ is adjusted to ensure downhill motion on the PES map. It has to be noted that the FIRE algorithm, optimizes only nuclei position keeping the volume and lattice parameter unchanged.

The FIRE algorithm works efficiently in the case of rough PES, where even popular Broyden-Fletcher-Goldfart-Shanno (BFGS) minimization based on the Hessian matrix often fails[37]. The optimization methods present the energy minima configurations, which are local rather than global minima. Therefore, several initial configurations are required to find the structure with the lowest energy.

Along with the local minima search in the case of a point defect system, the determination of saddle point or transition state (TS) configurations is another geometry optimization problem. The TS optimization approach used in this thesis is briefly mentioned later in sub-section 3.2.5.

3.2 Ab-intio calculations of point defects properties

3.2.1 Supercell approach

An ideal crystal is made up of an infinite number of periodic repetitions of the unit cell and all the physical properties of the crystal can be calculated using a small unit cell (Figure 3.2 (a)). For the electronic structure calculation of point defects, the introduction of a point defect leads to translation symmetry breaking of the lattice locally at the defect site and thus disrupting the electronic band structure. The two standard methods that are usually employed to calculate electronic structure are based on an approach of embedding the point defect into a finite-size cluster with free boundary conditions or a supercell with periodic repetition of the host material. Both methods have their advantages and disadvantages. In the case of the cluster approach, dependence on the size and shape of the cluster, along with surface dangling bond passivation, results in an undesirable effect on the calculated point defect properties. In this thesis, the supercell approach for the calculation of point defects electronic structure is used. The relevant drawbacks and the strategies to overcome those issues (to a great extent) are discussed here briefly.

The supercell approach with periodic boundary conditions (PBC) eliminates the need for surface passivation. But the supercell approach is also impacted by the limitation on the number of (bulk-like) atoms that can be considered under PBCs. The supercell method correctly describes the band structure of the host crystal and is ideal for the calculation of the electronic structure of point defects with highly localized defect-induced electronic states. However, PBCs used in the supercell approach leads to the interaction of the point defect with its periodic images. This electronic interaction impacts the position of localized defect states and points defect properties (such as transition levels). Another implication arises in the case of charge point defects, as there is no absolute reference for the calculation of electrostatic potential in the periodic structure. This makes the description of electronic chemical potential ambiguous, and the comparison of different configurations of point defects in terms of structure and charge requires a potential alignment term. These two issues of image charge interaction and ambiguous description of electrostatic potential are not present in the cluster approach

and thus are identified as advantages of the cluster approach. However, these two issues can be circumvented to a great extent by considering a large enough supercell, which attenuates the periodic image charge interaction, and by applying a correction to electrostatic potential.

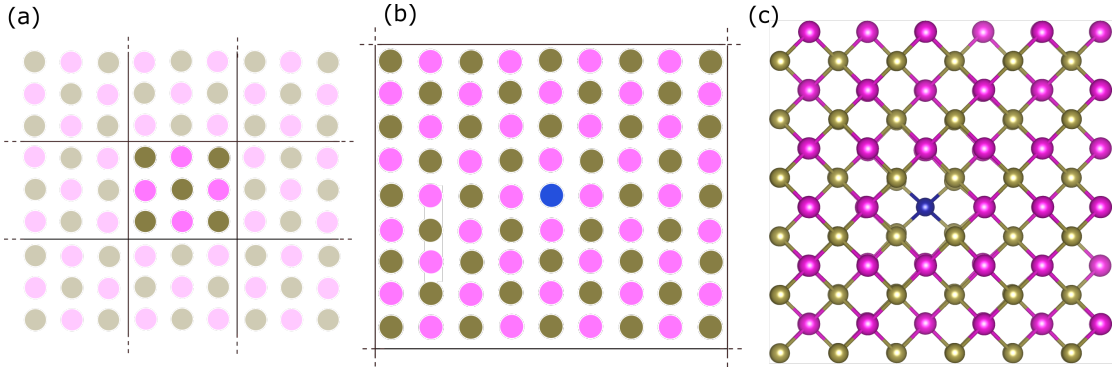

Figure 3.2: (a) A schematic 2D representation of a hypothetical unitary cell with periodic boundary conditions (periodic images are shown in the light shade). (b) The corresponding supercell formed by extending the unitary cell three times in the plane with an impurity defect atom (blue) present in the lattice. (c) Example of a 216-atom CdTe supercell (110 plane view) with the presence of an impurity defect.

For the study of semiconductor crystals, band structure and physical properties are modeled using unitary cells containing one or a few atoms with PBCs. To minimize the interaction of image charges, unitary cells with a relatively large number of atoms called supercell is employed. The supercell method is presented in Figure 3.2 (b). In a supercell, a perfect lattice is obtained by repeating a unitary cell of the host material (e.g., eight atoms in zinc-blende lattice) and then embedding the defect in the supercell (as shown in the Figure 3.2 (c)). Increasing the size of the (unitary) supercell reduces the interaction between the defect and periodic images as they are placed further apart. One thus obtains a superlattice of periodically repeated unit cells with the embedded point defect (and periodic images). In the case of charged point defects, the jellium background charge is introduced to neutralize the supercell, circumventing the divergence of electrostatic energy between periodic charge defect images. In realistic crystals, point defects are found in a dilute regime, such that the defects are isolated and non-interacting. To obtain accurate results, large supercells are required. However, the computational cost limits the number of atoms that can be considered. In our calculations discussed in this thesis, we have used 64 ($2 \times 2 \times 2 \times 8$), 216 ($3 \times 3 \times 3 \times 8$), and 512 ($4 \times 4 \times 4 \times 8$) atoms supercell with zinc-blende lattice. In most of the cases, 216 atom supercell results have provided good results for our qualitative description.

3.2.2 Formation energies

The primary physical quantity associated with the point defects is the formation energy; however, its description is not straightforward. The defect formation energy (E_f) can be regarded as the energy required to embed a defect in a pristine crystal (in the dilute limit) by a combination of addition, removal of defect atoms, and local rearrangement. Following the definition given by Zhang and Northrup, E_f under the supercell treatment is defined as the difference between the total energy of the host supercell containing defect (E^{def}) and the same supercell of the pristine bulk system (E^{bulk})[38]. Taking into consideration the addition and removal operation of atoms needed to create the defect with no net charge, the following expression defines E_f

$$E_f = E^{def} - E^{bulk} - \sum_i \Delta n_i \mu_i \tag{3.26}$$

where i labels the atomic species, Δn_i is the difference in the number of atoms of i^{th} atomic specie between defective supercell and pristine bulk supercell, and μ_i is the chemical potential of i^{th} atomic specie in a theoretical external reservoir. Any particle(s) added or removed in the process of embedding (creating) a defect in a perfect semiconductor crystal is considered to come from or being moved to a particle reservoir of a certain chemical potential.

The chemical potential associated with each atomic species is needed to be defined for non-stoichiometric defects. For example, considering the case of vacancy defect in binary semiconductors, we need to subtract the contribution of the atom removed (to create a vacant site) from the energy of pristine bulk. The definition of chemical potential is not trivial and will be discussed later in detail in the section 3.2.4. The stoichiometric defects are the ones where there is $\Delta n_i = 0$ *i.e.* no change in the number of atomic species or where all atomic species are added or removed in stoichiometric proportions, as in the case of Frenkel defects.

In the case of charged defects, E_f is also dependent on the semiconductor bulk electronic chemical potential μ_e as given by the following expression:

$$E_f^q = E^{def,\,q} - E^{bulk} - \sum_i \Delta n_i \mu_i + q\mu_e \tag{3.27}$$

where q is the charge of the system, and μ_e is the Fermi level, which in the case of semiconductors is present in the band-gap and is dependent on other defects present in the crystal and the external potential applied to the system. The μ_e is consequently defined in terms of its relative position to the valence band maximum (VBM) and can take value from 0 eV to the conduction band minima (CBM) value with respect to VBM

ε_v.

$$\mu_e = \varepsilon_v + \Delta\mu_e \tag{3.28}$$

This definition of μ_e also allows to align the density of states of the defect supercell with that of the pristine bulk supercell in order to correct the spurious electron potential shift.

3.2.3 Charge transition levels

The electronic levels as induced by point defects in semiconductors are fundamental for understanding their character and comparison with the experimental results. However, the electron activity levels as measured in the experiments, do not correspond to one electron eigenvalues calculated using DFT Kohn-Sham formalism. In experiments, transition levels associated with a state change are measured. Charge transition levels (CTLs) corresponding to point defects are the most common experimental identification signatures.

Baraff *et. al.* defined the charge state transition levels $E(q_1/q_2)$ as the value of electron chemical potential μ_e (with respect to pristine bulk valence band edge ε_v), where there is a crossover point of the defect formation energies of two charge states q_1 and q_2 [39]. As the Fermi level is raised, the most stable charge state changes from q_1 to q_2 (Figure 3.3).

Once the choice of chemical potential values of atomic species is made, defect formation energies can be studied as a function of μ_e. In terms of the formation energies calculated for the ground state configurations corresponding to charge state q_1 ($E_f^{q_1}$) and q_2 ($E_f^{q_2}$) at $\mu_e = 0$; CTL can be equated using the following equation.

$$E(q_1/q_2) = \frac{E_f^{q1}(\mu_e = 0) - E_f^{q2}(\mu_e = 0)}{q_1 - q_2} \tag{3.29}$$

$$= \frac{E^{q1} - E^{q2} - (q_1 - q_2)\varepsilon_v}{q_1 - q_2} \tag{3.30}$$

Here, E^{q1} and E^{q2} are the total energy of the defect supercell with charge state q_1 and q_2, respectively. Therefore, $E(q_1/q_2)$ is simply the energy difference between the two charge state of the defect system on the transfer of a single electron from/to electron reservoir, i.e., $|q_1 - q_2| = 1$.

For the CTL calculations, the ionic configurations are independently relaxed and correspond to the ground state. In cases where ionic configurations significantly differ

for two charge states, refer to the deep character of the defect.

The charge state stability transition levels can be represented by a plot (Figure 3.3) showing the defect formation energy of the most stable charge state as a function of electron chemical potential μ_e. As suggested by Equation 3.28, the formation energy of each charge state varies linearly with μ_e with a slope equal to charge. It is important to mention that CTLs are commonly referred to as defect levels and represent a different electronic occupation of defect-induced states.

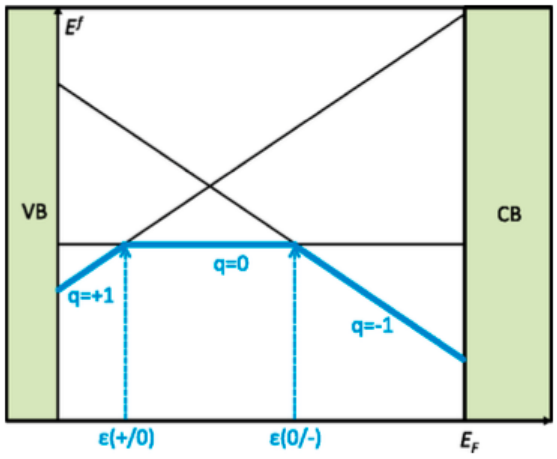

Figure 3.3: Schematic diagram presenting the variation of formation energy of a (hypothetical) defect with the value of electron chemical potential (Fermi energy) in charge state (q) +1, neutral, and −1. The thick blue solid lines represent the thermodynamically most stable charge state for a given Fermi energy. The charge transition levels (CTLs) within the band gap representing a change in the most stable charge state are marked with dashed lines. The Figure is reproduced from the the attached reference[40]

The calculated CTLs correspond to the defect levels as measured in quasi-equilibrium experiments such as deep-level transient spectroscopy (DLTS) and temperature-dependent measurements of resistivity and Hall data. The position of the CTLs with respect to host band edges reflects the shallow or deep character of the defect.

DFT calculations performed using DFT-LSDA calculations do not give a correct quantitative estimate of CTLs due to the underestimation of band-gap. However, a good qualitative description of the CTL position with respect to band edges can be obtained in general[41].

Since CdTe is a II–VI binary semiconductor, defects tend to be either neutral or have a ±2 charge. In the case of (de-)excitation of a valence electron (from)to a defect state, it becomes less likely for the next electron to be excited to the same defect state

due to coulomb repulsion. However, in the case of CdTe point defects, the energy lowering induced by local ionic perturbation overcomes the coulomb energy making it more favorable for the second electron(hole) to occupy the same electronic defect state. This is known as Anderson's negative-U effect; U stands for electron-electron repulsion[42].

3.2.4 Chemical potential

It is non-trivial to define the chemical potential for binary semiconductors and the system with impurities, as there is no unique way to choose, and the values depend on the experimental growth conditions (such as temperature and pressure). However, the upper bound and lower bound can be defined without taking the growth conditions into consideration. As mentioned in the previous section 3.2.2, the chemical potential values depend on the atomic species external reservoir from which defect atom(s) are being removed to or taken from. A reasonable choice in the case of binary semiconductors could be the elemental phase of atomic species being the reservoir. In such a case, *e.g.* for a point defects present in CdTe bulk, atomic pair Cd-Te pair energy can be obtained using a simple supercell calculation of pristine bulk. However, it is ambiguous how to define the energy contribution between individual atomic species, i.e. Cd and Te. The relation of the Cd-Te pair (μ_{CdTe}) chemical potential in CdTe bulk under thermodynamic equilibrium with the individual chemical potential of Cd (μ_{Cd}) and Te (μ_{Te}) in CdTe is defined as

$$\mu_{CdTe} = \mu_{Cd} + \mu_{Te} \tag{3.31}$$

$$\mu_{Cd} = \mu_{Cd}^{bulk} + \Delta\mu_{Cd} \tag{3.32}$$

$$\mu_{Te} = \mu_{Te}^{bulk} + \Delta\mu_{Te} \tag{3.33}$$

where $\Delta\mu_{Cd}$ and $\Delta\mu_{Te}$ are the deviation in the value of μ_{Cd} and μ_{Te} in CdTe from the elemental bulk phase. The upper bound on the μ_{Cd} and μ_{Te} can be defined noting the fact that neither of these chemical potential values can be higher than the per atom energy of each species (Cd and Te) in elemental phase. This then leads to

$$\mu_{Cd} \leq \mu_{Cd}^{bulk} \tag{3.34}$$

$$\mu_{Te} \leq \mu_{Te}^{bulk} \tag{3.35}$$

where μ_{Cd}^{bulk} and μ_{Te}^{bulk} is the energy per atom of Cd and Te bulk in most stable elemental phase. By combining these two inequalities lower bound on the chemical potentials can be defined as well in this manner

$$\mu_{Cd} \geq \mu_{CdTe} - \mu_{Te}^{bulk} \tag{3.36}$$

$$\mu_{Te} \geq \mu_{CdTe} - \mu_{Cd}^{bulk} \tag{3.37}$$

These upper and lower bound corresponds to the experimentally defined (extreme) Cd-rich and Te-rich conditions. In extreme Te(Cd)-rich conditions, Te(Cd) chemical potential corresponds to bulk Te (Cd), equation 3.36 (3.37). Therefore it is important at times to set the upper bound defining corresponding rich condition. Under this upper bound limit for the chemical potential of one constituent atomic specie, constitutional defects can be defined. In the case of Te-rich (Cd-rich) conditions, the constitutional defect can either be V_{Cd} (V_{Te}) or Te_{Cd} (Cd_{Te}). This can be determined by comparison of corresponding formation energies.

For impurities, it is not simple to define the reservoir. The reservoir choice depends on the source of the impurity and the compounds formed by the impurity with the bulk host constituent atoms. Although an upper bound can be defined by energy per atom of impurity bulk elemental phase. This thesis deals majorly with the interaction of impurity atoms with intrinsic points defects present in CdTe. In chapter 4, Se impurity-related defect complexes have been discussed; we have defined the impurity-related defects using the relative formation with respect to constitutional (V_{Cd}) defect in Te-rich limit. We used the most stable configuration of the Se impurity interstitial defect to define the Se chemical potential.

Defect complexes are formed when isolated defects present in close vicinity bind together in such a way they are placed adjacent in the lattice.

In chapter 5, transition metal (TM) impurity defect interactions with constitutional defects in Te-rich and Cd-rich are defined by the binding energy of defect complexes. The binding energy can be defined without the need to define the chemical potential of component defects. This way, we get over the need to define the chemical potential for TM impurities. The definition of binding energy for defect complexes is given in the following section 3.2.6.

3.2.5 Diffusion barrier and Nudged Elastic band method

Knowledge of the dopant diffusion mechanism on the microscopic level is important to understand the dopant diffusion profile and defect interaction in the host lattice. Dopant diffusion, in the majority of cases, is assisted by the interaction with native defects such as vacancies and self-interstitial. Diffusion with the help of interstitial can take place with two different mechanisms, either through interstitialcy mechanism, in this case, substitutional impurity and self-interstitial diffuse as a pair, or kick-out mechanism where the impurity is kicked out from a lattice site and diffuses as an isolated interstitial.

The diffusion coefficient D_A of impurity is temperature dependent and given by a Boltzmann relation, expressed as

$$D_A = D_A^0 exp\left(-\frac{E_a}{k_b T}\right) \tag{3.38}$$

where D_A^0 is the pre-exponential factor that contains temperature-independent contributions, and E_a is the activation energy, which is roughly the sum of formation energy and the diffusion barrier.

As pointed out in equation 3.38, the diffusivity of impurities (defects) in the semiconductor host lattice depends on the formation energy E_f of the mobile defect and the corresponding migration barrier E_{mb} for diffusion. The calculation of E_f is already defined in the previous subsection 3.2.2. The barrier E_{mb} can be determined using DFT calculations employing a theoretical framework based on the harmonic transition state theory (HTST). The E_{mb} is defined using the minimum energy path (MEP) connecting two energy minima on the PES of the mobile defect (interstitial) as the associated barrier related to the movement from initial to final configuration through a unique transition state (saddle point). The work by Vineyard et. al. provides (laid) out the theoretical foundation for nudged elastic band method (NEB) commonly used for DFT calculation of point defect mobility[43,44].

The diffusion of impurities in a crystal is simply the migration of associated point defects in the lattice. The defect moves from site A to B (adjacent stable (metastable) configurations) by means of thermal energy. The barrier can be obtained by establishing the minimum energy path (MEP) on the PES $E(R_i)$ (PES depends on the coordinate of nuclei of the point defect system). The algorithms used to define the MEP reduce the multidimensional character of the PES to establish the diffusion path.

In search of the minimum energy path, once the saddle point configuration is found, the gradient of energy downhill in both forward and backward directions of unstable mode can establish the diffusion path trajectory.

Nudged Elastic band method (NEB)

NEB algorithm is the method used to find the MEP between local minima on a PES[44,45]. The algorithm is based on the transition state theory, following which a set of replicas configurations connecting two adjacent local minima configurations is created along a guess energy path. These replicas are assumed to be connected through springs, which forces the configurations to be equidistant along the transition path.

The entire chain of replica configurations attached through springs joining initial and final configurations is then relaxed, keeping the endpoints fixed. The forces on the images are minimized through an approach where images are 'nudged' perpendicular to the local tangent of the path, ensuring relaxation with respect to the true force in that direction. Following such an approach, the force on each image contains the parallel component of spring force expressed as

$$F_i^s|_{\|} = k(|R_{i+1} - R_i| - |R_i - R_{i-1}|)\hat{\tau}_i \tag{3.39}$$

and the total force on each replica is:

$$F_i = F_i^s|_{\|} + F_i^t|_{\perp} = k(|R_{i+1} - R_i| - |R_i - R_{i-1}|)\hat{\tau}_i - \nabla E(R_i)|_{\|} \tag{3.40}$$

The tangent at an image i is estimated from the position of two adjacent images R_{i+1} and R_{i-1} along the path, as follows:

$$\tau_i = \frac{R_i - R_{i-1}}{|R_i - R_{i-1}|} + \frac{R_{i+1} - R_i}{|R_{i+1} - R_i|} \tag{3.41}$$

where $\hat{\tau}_i$ is the unit vector.

Force on each replica is minimized to establish MEP and provide an initial guess for the transition state configuration.

Improved implementation of NEB referred to as climbing image NEB uses a Intermediate step to speed up the search of the saddle point. In this case, the image with the highest energy is identified and made to move uphill along the elastic band by considering that only the inverted parallel component of true force acting on it.

Transition state optimization

The optimization of TS is performed using the Direct Inversion in the Iterative subspace (DIIS) algorithm[46]. This method is used to minimize the forces on a given atomic configuration, once the initial guess is close to the target (metastable/unstable) configuration. Therefore a reliable initial guess for the TS that is in the quadratic region (of

energy gradient) of the first-order saddle point is required. This initial guess of the TS is obtained using the NEB method. The saddle point configuration in case of point defect migration usually has a regular symmetry, and thus an initial guess can be made.

3.2.6 Binding energy

The binding energy of defect complex AB with respect to component defects A and B can be calculated using the formation energies of isolated defects A ($E_f(A^{q_A})$) and B ($E_f(B^{q_B})$), and that of defect complex AB ($E_f(AB^{q_{AB}})$) as

$$E_b(A^{q_A}B^{q_B}) = \left[E_f(A^{q_A}) + E_f(B^{q_B})\right] - \left[E_f(AB^{q_{AB}})\right] \tag{3.42}$$

where $q_{AB} = q_A + q_B$. The defect formation energies of component defects are calculated in separate supercells, which are identical except for the embedded defect is under the dilute limit.

Therefore, according to equation 3.42, the binding energy is not dependent on the chemical potential of impurity as it cancels out in the above expression. The positive binding energy of a defect complex AB suggests that the complex formation is driven by thermodynamics and is energetically favorable. The negative binding energy suggests that the defect complex will not form.

The binding energy of a defect configuration where component defects A and B are separated and are present within the same supercell can be compared with defect complex AB configuration to understand the stability trend. In this case, the equation becomes,

$$E_b(AB^{q_{AB}}) = E(A^{q_A} + B^{q_B}) - E(AB^{q_{AB}}) \tag{3.43}$$

Where E(A+B) is the total energy of the supercell containing the two separated component defects. In this case, q_A and q_B cannot be controlled and may show the change in the charge state of one of the component defects as controlled by the other component defect with respect to the most stable charge state of isolated component defects (and $q_{AB} = q_A + q_B$ situation may not hold).

3.2.7 Symmetry and Jahn-Teller distortion

An infinitely extended perfect crystal have a periodic arrangement of atoms with translational symmetry invariance. Electron number density n(r) in such an arrangement follow the periodic potential and can be described as n(r) = n(r+T). The introduction of

point defects in an otherwise perfect infinite lattice leads to the breaking of the translation symmetry of the lattice structure. Vacancy defects are the most common point defects present in a semiconductor lattice and are the most studied. Therefore local electronic structure changes brought by point defects are generally defined using the models proposed for vacancy defects. The translation symmetry breaking resulting from the presence of a point defect is accompanied by a strong chemical change in the small region around the defect as a result of (in the case of a vacancy) the creation of the dangling bonds/broken bonds on under-coordinated atoms. These dangling bond host unpaired electrons whose electronic wavefunctions are very different from the Bloch-like eigenstate of electrons present in perfect crystal potential and are rather localized. Electrons in dangling bonds interact and recombine to create localized states in the host band structure.

Experimental measurements and theoretical calculations consistently suggest that atoms hosting dangling bond electrons undergo strong re-arrangement to attain a configuration with lower energy. The major interactions at play are electron-electron Coulomb interaction, Jahn-teller distortion[47] (electron-lattice/phonon coupling), and elastic deformation resulting as a reaction to distortion induced from the electronic effect. Such electron-electron and electron-lattice interaction induce large atomic displacements of first neighbor atoms and as a consequence, second or even third neighbors of the vacancy. The range of the defect-associated distortion and the consequent elastic deformation depends strongly on the charge state of the defect, atoms hosting dangling bond electrons, and semiconductor physical properties. These issues related to different defects are are usually need to be addressed specifically for an individual defect.

Previosuly, local distortions around vacancy defects have been studied in detail, with particular emphasis on Si and diamond vacancy defects. Ab-initio calculations of point defects in semiconductors generally understand the electronic structure in terms of the Coulson-Kearsley defect molecule model[48]. In the subsequent subsection, we will briefly discuss the defect molecule model.

Defect molecule model

The defect molecule model exploits the molecular character of the vacancy point defect, considering the point defect could be approximated as a local perturbation embedded in to a host lattice. In such a situation, the defect system is assumed to be de-coupled from the host lattice and can be defined only by the electronic orbitals, which are most perturbed because of the creation of vacancy defect/removal of an atom from the lattice. The model is originally proposed to understand the color centers related to vacancy

defects in the Diamond lattice. In a diamond lattice with covalent bonds, the removal of a single atom from the lattice leaves behind one out of four valence electrons in broken/dangling bonds on each neighboring atom. The model makes two assumptions related to the electron that the vacancy electrons are highly localized, and the atomic orbital eigenstate associated with electrons do not diffuse in to host lattice. Thus the model is limited to the covalent bonded systems and the vacancy defects, which are deep in character where dielectric effects are greatly reduced.

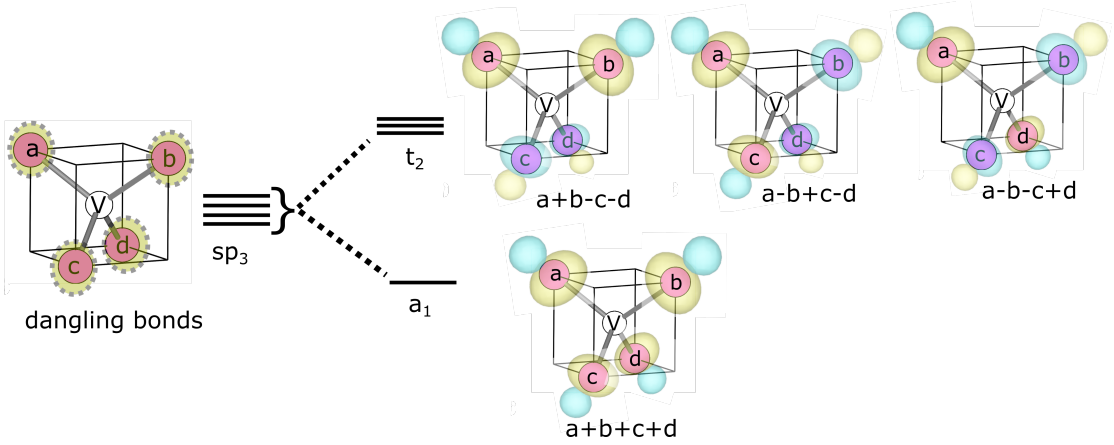

Figure 3.4: Electrons in the dangling bonds of vacancy defect resulting in to sp^3 type linear combination of atomic orbitals (a, b, c, d) where singlet a_1 is formed by symmetric in-phase contribution and triply degenerate orbitals are formed by combination of in and out of phase contributions.

The four one-electron atomic orbitals associated with dangling bonds pointed toward the vacancy site form the basis of the model. Considering such orbitals a, b, c, and d hosting electrons on atoms A, B, C, and D atoms as shown in Fig.X (a). In a diamond-like lattice, the defect molecule has a tetrahedral (T_d) symmetry, and the wavefunction of the defect can be expressed using molecular orbital (MO) theory with the molecular orbitals expressed as a linear combination of the atomic orbitals (LCAO) of the one-electron eigenstates a, b, c, and d. Adopting the T_d symmetry (considering T_d symmetry transformation) and sp_3 coordination, four MOs result from the combination of atomic orbitals. The resulting MOs are shown with their respective energy in Fig.X(b). The lowest energy state results from symmetric contribution from the atomic orbitals and transforms as (a+b+c+d) is consequently node-less. Three combinations result from different phase(±) relationships of the atomic orbitals expressed as a+b-c-d, a-b-c+d, and a-b+c+d. These states are degenerate in energy and are represented as t_2 for triple-fold degeneracy, whereas the symmetric defect state is represented as a_1

in the point group symmetry scheme. The vacancy configurations with partially occupied orbital t_2 degenerate states depending on charge state are subjected to the uplifting of degeneracy leading to symmetry breaking caused by lattice distortion as a result of the Jahn-Teller theorem. The distortion is brought out by electron-phonon/lattice coupling. The distortion around the vacancy defect can be defined in terms of distances d_{ij} between the atoms, where i and j represent one of the four nearest neighbors of vacancy.

The point group symmetry of the defects is generally modeled using the defect molecule approximation and the group theory principles. We have consistently used one-to-one correspondence between the Kohn-Sham wavefunction of defect eigenstates and the LCAO as suggested through defect molecule representation, to model and interpret the local electronic structure of point defects considered in this thesis.

Watkins' Model

Watkins' proposed a scheme to explain the Silicon vacancy local structure symmetry and distortion induced by the electronic interaction for different charge states based on the symmetry-adapted orbitals from the defect molecule model. The model is conceived to sustain the evidenced symmetry from the electron paramagnetic resonance experiment results for the charge state q=± of mono-vacancy. The main contribution of the model is to describe the instability of the vacancy un-distorted T_d symmetry to Jahn-Teller symmetry breaking induced by lowering of energy of partially occupied degenerate defect states. According to Watkins' in +2 charge state, vacancy structure sustain the T_d symmetry locally around the vacant site with s-like (a+b+c+d) defect state labelled as a1 in completely filled and the p-like t_2 degenerate all empty. The energy of defect state lowers on occupation of an electron in p-like b_2 defect state MO of the form a+b-c-d in q=+1 charge state which lead to pairing between the atoms with the same phase on MO i.e. atom A-B and C-D make pair. This brought out a tetragonal distortion lowering the symmetry to D_{2d} leading inward relaxation. The six inter-atomic distances transforms as $d_{13} = d_{24} < d_{12} = d_{23} = d_{14} = d_{34}$. The tetragonal distortion mode is not unique with three equivalent distortion mode possible with three possible combination of pairing among atoms.

Further addition of one electron leading to neutral state push one electron in to the state a+b-c-d and thus sustaining and stabilizing more the overall D_{2d} symmetry of the vacancy structure with stronger inward relaxation. This addition of electron to a singly occupied state is against the scheme of Hund's rule which advocate parallel spin coupling due to electron-electron coulomb repulsion. However in the case of Si vacancy the Jahn-Teller energies resulting from the degeneracy uplifting of defect states overcome

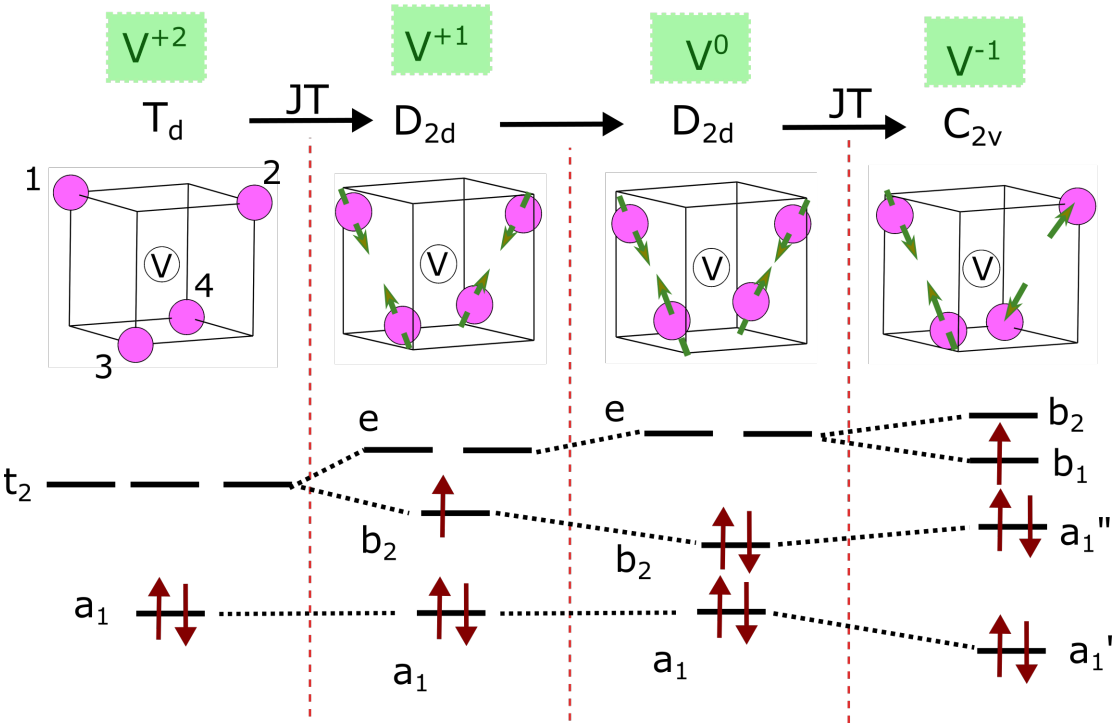

Figure 3.5: Jahn-Teller instability induced by the partial filling of tripet t_2 states for different charge state of the Silicon vacancy. The local structure of vacancy is shown with four neighboring atoms and their respective distortions (green arrows). T_d symmetry is stable in charge state +2 with empty t_2 (p-like) states. Symmetry reduces to D_{2d} and C_{2v} with filling of electrons (brown arrows) in the t_2 states which split in to components due to Jahn-Teller effect.

the coulomb repulsion energies. This is known as Anderson's effective-negative-U system where the energy lowering due to local distortion is higher than the compensating e-e repulsion. In this case second electron will rapidly follow the first electron on addition. Further addition of an electron to q=-1 charge state breaks the overall symmetry of defect states of defect molecule model due to additional dihedral distortion lowering the symmetry to C_{2v}. In turn the MOs in C_{2v} symmetry with complete degeneracy breaking take up the form b+c; a+d; a-d; and c-d labelled as a_1, a_1', b_1, and b_1' (in group theory scheme) in that energy order suggesting an outward relaxation of atom A and D away due to occupation in anti-bonding type orbital a-d. Consequently six interatomic distance in this case are given as $d_{24} = d_{JT1} < d_{13} = d_{JT2} < d_{12} = d_{23} = d_{14} = d_{34}$.

Watkins' Jahn Teller symmetry description of the vacancy defects based on the number of electrons present in LCAO formed under defect molecule approximation has been extensively used to interpret the symmetry lowering in point defects and the influence

of charge on electronic structure. We have consistently used the defect molecule model and the ideas of Watkins' model to relate the calculated symmetry of the point defects, considered in thesis, with the defect electronic states position in host band structure and the Kohn-Sham wavefunction character to interpret our results. These two models can be used effectively to model initial configurations to find the local ground state symmetry of the point defects and compare the symmetry of ground state with the reported EPR results in temrs of electronic structure of the defect.

CHAPTER 4

Se diffusion mechanism and passivation of critical defects in CdTe

4.1 Introduction

Cadmium telluride (CdTe) is a II-VI semiconductor that can be easily doped both p- and n-type and have a direct band gap energy of $\sim$ 1.5 eV[49,50]. CdTe has a wide range of applications and is one of the most important semiconductor materials used in photovoltaics, medical imaging, and high-energy astronomy[51–62]. In the thin film solar cells industry, CdTe based solar cells have been one of the front runners with successful commercialization and worldwide installed capacity of more than 15 giga watts[63]. CdTe band-gap value of $\sim$ 1.5 eV is optimal and close to the ideal band-gap value of 1.35 eV corresponding to maximum efficiency of $\sim$ 32 % according to the Shockley-Queisser limit[64,65] (Figure 4.1). The near-optimal band gap for visible absorption is responsible for the absorber layer thickness in CdTe solar cells going down to a level of $\sim$ 3 μ m in comparison to Si solar cells, which are typically of 50 times thicker in size[52]. Thin film CdTe absorber layer gives a manufacturing advantage over Si-based solar cells. In addition, it has a high optical absorption coefficient ($> 5\times10^5$ cm^{-1}) near the band edge, allowing it to absorb most of the sunlight in large visible spectral range[66–68]. These factors make CdTe a suitable material for use in thin-film solar cells as the absorber layer. Recent years have seen rapid improvement in the efficiency of

CdTe-based solar cells. In the last decade, the efficiency of CdTe solar cells has improved from 16.7 to 22.1 %[69]. This surge in efficiency has seen the manufacturing cost reduced to such levels that now the unsubsidized levelized cost of electricity from CdTe photovoltaics is cheaper than popular silicon photovoltaics and conventional fossil fuel resources[70].

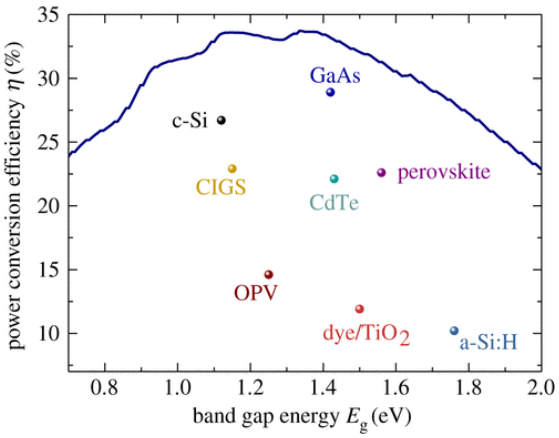

Figure 4.1: Plot of lab-grown solar cells record power conversion efficiency of high-performance semiconductor materials corresponding to their band-gap values, reproduced from the the attached reference[71]. The blue curve represents the theoretical Shockley-Queisser limit.

The basic structure of a solar cell is made of a p-n junction such that an in-built electric field separates electrons and holes generated by photons from light illumination. The solar cell efficiency, defined as the power ratio between electric output and photo-generated energy input, depends on three factors: open circuit voltage (V_{0c}), short circuit current density (J_{sc}), and filling factor (FF)[72]. Microscopically, V_{oc}, J_{sc}, and FF are related to carrier density and carrier lifetime. The V_{oc} is directly related to the band-gap and the carrier concentration, these two factors decide the Fermi energy splitting between n-type and p-type layers[73,74]. The J_{sc} depends on the carrier density and their lifetime[75]. The carrier concentration and lifetime rely on the defect properties and their control[76]. The point intrinsic defects or impurities with shallow character contribute to n-type and p-type doping. Whereas, the defects with deep character form non-radiative recombination centers can capture both electrons and holes with the help of phonons based on Shockley-Read-Hall (SRH) recombination process[17,18,77]. The carrier lifetimes are therefore limited by the defect-mediated recombination.

The most recent improvement in CdTe-based solar cell efficiency from 19.5 to 22.1 % has been achieved by the addition of Selenium (Se) to the front of the CdTe

absorber layer[5]. This increase in efficiency from the previous record performing $CdCl_2$ treated CdTe solar cell is explained based on lower material band-gap value ~1.4 eV (closer to the optimum band-gap value of ~1.35 eV), increased absorption of long-wavelength of the spectrum, device short-circuit current density (J_{sc}) and a slight improvement in open-circuit voltage (V_{0c})[5,78–80]. For record performing cell, open circuit voltage V_{0c} is ~887 mV and is severely limited by defects, compared to the theoretical Shockley–Queisser (SQ) limit of 1157 mV[81,82]. This large gap between the achieved value of V_{0c} and the theoretical limit is largely attributed to the low carrier lifetimes in CdTe.

Munshi *et. al.* suggested that Se alloying results in a bandgap grading from 1.50 to 1.40 eV leading to an increase in the wavelengths adsorption range[83]. Recent *ab initio* studies based on Density Functional Theory (DFT) support this reduction in band-gap in the case of $CdSe_xTe_{1-x}$ (CdSeTe) alloy formation, that is caused by bowing of the band-edges[84,85]. In agreement with experimental values, these studies suggest a minimum value of band-gap at ~1.40 eV for a value of x~0.35. However, this band gap reduction does not capture on its own the reported efficiency improvement as it cannot account for an efficiency increase of more than 2.5 %. This puzzle was recently solved by Fiducia *et. al.* through means of cathodoluminescence (CL) experiments coupled with Secondary Ion Mass Spectrometry (SIMS) measurements that revealed long-range diffusion of Se into the CdTe absorber[86]. They showed segregated diffusion of Se in to inter-diffused CdTe region, and fast diffusion of Se in the CdTe region along grain boundaries based on photons count mapped with their energy in CL experiments and SIMS analysis (Figure 4.2). At low concentrations of Se, a radiative transition level, in addition to the bowing of the band-gap was also noted down, corresponding to a defect transition level at an energy value of ~1.36 eV. Through the photon counts recorded at different distances from the top of the absorber layer, they also showed a clear increase in the local luminescence directly related to the Se content (Figure 4.2 (d)). Based on this dependence, they suggested that Se leads to the passivation of critical deep defects in CdTe and higher luminescence efficiency.

Recent DFT study by Watts *et. al.* on $CdSe_xTe_{1-x}$ alloy confirmed that transition level at an energy value of ~1.36 eV does not correspond to $CdSe_xTe_{1-x}$ bulk at any concentration. They suggested that it could be due to the possibility of interaction of Se with the intrinsic defect, such as Cd vacancies (V_{Cd}) and Te antisites (Te_{Cd}) leading to the defect complex formation which is responsible for 1.36 eV emission[85]. This suggestion was based on the knowledge that most of the CdTe crystals are grown by conventional Bridgman and high-pressure Bridgman techniques, resulting in a Te-rich material with a high concentration of V_{Cd} and Te_{Cd}, which both act as non-radiative

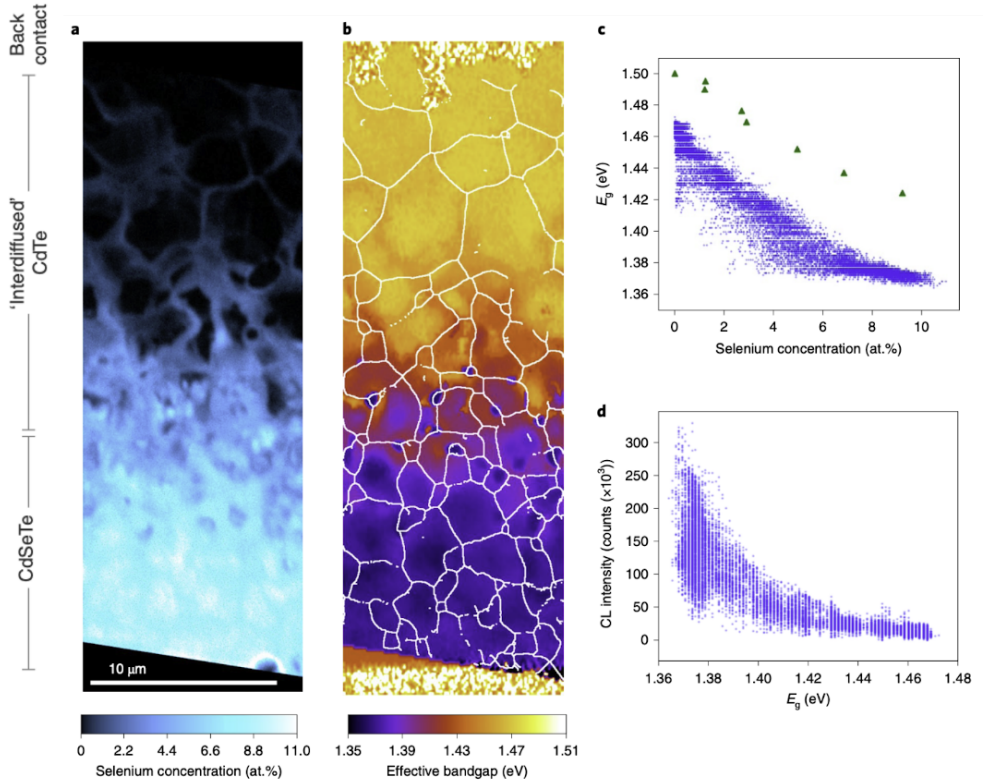

Figure 4.2: (a) Secondary Ion Mass Spectrometry (SIMS) map of Se concentration in solar cell device (CdSe layer present at the front of absorber). (b) map of the peak emission energy as observed in cathodoluminescence (CL), which corresponds to the effective bandgap of the material (on the same area as in (a)). (c) band-gap variation at each recorded point with Se concentration and (d) Photon counts in CL corresponding to band-gap value at the point of observation in the CL experiment. This Figure is taken from the experimental study by Fiducia *et. al.*[86]

recombination centers[87–89].

Li *et. al.* following the results from Fiducia *et. al.* addressed how the Se doping/alloying impacts the major critical defect present in CdTe, using transient photocapacitance (TPC) spectroscopy[90]. TPC spectroscopy is a powerful tool for identifying deep defects. In the TPC measurements, they identified a defect band centered at 1.07 eV above the valence band as the major critical defect transition level with an activation energy lower than 0.43 eV (Figure 4.3 (a)). Based on previous simulation results, they suggested that the defect level corresponds to Te_{Cd}. Temperature-dependent TPC

measurement results based on the CdTe devices with the presence of the CdSe layer were shown to have reduced defect signal in comparison to devices with no CdSe layer. They deduced that decreased defect signals were mainly due to the lower defect (critical defect) density in the CdSeTe alloy. They also pointed out that the carrier lifetime increased by more than six times in Se alloyed devices.

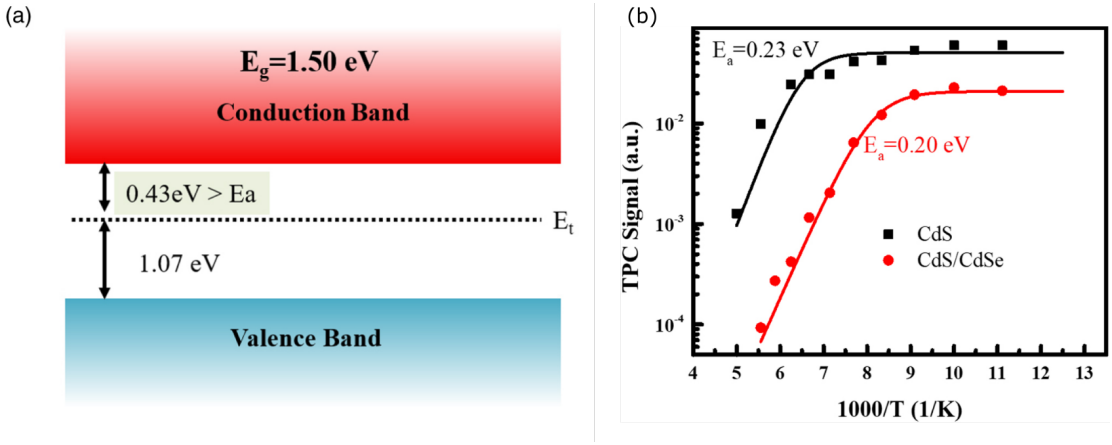

Figure 4.3: (a) Schematic diagram showing the transition level associated with the deep defect in CdTe (b) Temperature-dependent normalized transient photo-capacitance (TPC) signal corresponding to CdTe devices with CdSe (and without CdSe) layer shown with black (red) markers illuminated using 1.07 eV monochromatic light. The solid lines indicate the fitted curves using the thermal quenching mode. This Figure is taken from the experimental study by Li *et. al.*[90].

The experimental works by Fiducia *et. al.* and Li *et. al.* clearly established at the microscopic levels, two key reasons for efficiency improvement *i.e.* (i) band-gap grading and (ii) critical defects passivation in CdSeTe alloy[86,90]. We took motivation primarily from these two and a number of other experimental studies[80,83,91,92] conducted on Se alloyed CdTe solar cells to give atomistic level insight on the two factors behind efficiency improvement, by means of DFT calculations. Diffusion mechanism at the atomic level can give detailed information on the Se related diffusion defect and interaction with intrinsic defects in CdTe such as Te_{Cd}. The stability of the defects complexes, which can result from such interaction of Se with intrinsic defects V_{Cd} and Te_{Cd}, can then be calculated based on their formation energy.

In this chapter, using DFT based ground state calculations, we will explain the process of Se diffusion in CdTe bulk. We found low energy barriers for chalcogenide Se and Te diffusion in the CdTe lattice between neighboring stable sites. We, then, using our knowledge of chalcogenide diffusion, discuss the interaction of the diffusing

chalcogenide defect with Cd vacancy. We propose a possible passivation mechanism of Cd vacancy and Te antisite critical defects on interaction with Se diffused into CdTe bulk.

4.2 Methodology

All the calculations are performed in the framework of DFT using BigDFT code[93]. CdTe zinc blend structure belonging to $F\bar{4}3m$ space group is used. Valence electrons of Cd (12 e^-, including semi-cores), Te (6 e^-), and Se (6 e^-) were described on a wavelet basis set[94] and core electrons were frozen in the approximation of pseudo-potentials using Hartwigsen-Goedecker-Hutter formalism[36]. Local Density Approximation (LDA) functional[95] is used to approximate the exchange-correlation energy. The calculated value of the CdTe lattice constant for these pseudo-potentials is 6.42 Å, which is close to the experimental value of 6.48 Å[96]. The electronic structure calculations of the ground state of all the defects considered in this study are performed employing a $3 \times 3 \times 3$ supercell of 216 atoms. The ground state structure of all stable defect configurations were optimized using Fast Inertial Relaxation Engine (FIRE) algorithm[37]. The calculations were performed with only gamma-point. Formation energy ($\Delta^{EF}(q)$) of all considered point defects in charge state q is calculated using the following equation 4.1[40].

$$\Delta^{EF}(q) = E_T^{(defect,q)} - E_T^{perfect} \mp \sum_i (n_i \times \mu_i) \mp q\mu_e \tag{4.1}$$

Where $E_T^{(defect,q)}$, $E_T^{perfect}$, i, n, μ_i, and μ_e are total energy of the supercell with point defect, the total energy of the pristine supercell, index for atomic species present, change in the number of atoms of each atomic species in defective supercell respective to pristine supercell, the chemical potential of atomic species, and electron chemical potential (Fermi level) respectively. Arithmetic operator, $\mp$ in Equation 4.1 indicates additional or removal of atomic species in the defect, respectively. Barrier energies corresponding to diffusion steps were obtained with the Nudged Elastic Band (NEB) method[97?] in 64-atom super-cells while the saddle point configurations were later relaxed in 216-atom super-cells using Direct Inversion in the Iterative Subspace (DIIS) algorithm[46].

Kohn-Sham eigenvalue energies closely related (corresponding) to defect (induced) electronic states were corrected using potential alignment scheme. In this scheme the potential in the defect cell is aligned to that of bulk by a value δ_{VBM}. For δ_{VBM} we use the energy difference between the potential of the least perturbed point in the defect-

containing supercell and the same point in the defect-free supercell.

4.3 Intrinsic and doping Defects

In the case of typical Te-rich growth conditions, Cd-vacancy (V_{Cd}), Te-antisite (Te_{Cd}), and Te-interstitial (Te_i) are consistently proposed as the major defects previously both in experiments[90,98] and DFT calculations [72,99–101]. Te_{Cd} and V_{Cd} are predicted to have non-radiative recombination character responsible for carrier trap and reducing the photovoltaic efficiency of CdTe[72,89,100,102,103]. Te_i is predicted to be the primary mobile defect responsible for Te diffusion in CdTe[104–106]. We have studied the electronic structure of both critical defects V_{Cd}, and Te_{Cd} and mobile defect Te_i. For the case of Se present in CdTe, we studied the Se substitution defect at both Cd-site and Te-site. The lower energy configurations of Se_i were then identified to help explain the diffusion of Se in CdTe bulk.

4.3.1 Critical intrinsic defects

Cd-vacancy

For calculation of Cd-vacancy (V_{Cd}) electronic structure, a Cd atom is removed from a regular 216 atom supercell. Neutral charge state V_{Cd} structure can be modeled using the defect molecule model[48] proposed by Coulson and Kearsley based on the number of electrons present in dangling bonds of neighboring Te atoms[89,107,108]. Removal of a Cd atom from a regular Cd-site in the CdTe bulk results in four Te dangling bonds. The vacancy leaves behind 6 electrons in Te dangling bonds with T_d symmetry from the Zinc-blend structure. These 6 electrons are hosted in sp^3 like defect states with a bonding character. Defect electrons are filled in these states such that two electrons are placed in singlet a_1 (s-like), and four electrons are placed in three-fold degenerate triplet t_2 (p-like) states.

The V_{Cd} can adopt different local point group symmetry configurations in accordance with the defect molecule model and the previously reported results[89,108]. The vacancy local structure depends on the localization of electron density in dangling bonds, the position of the defect electronic states with respect to the band-edges, and Jahn-Teller distortion. Considering the possibility of Jahn-Teller distortion (keeping degenerate empty states in mind), we assumed several initial configurations for the neutral vacancy local electronic structure with point group symmetry lower than T_d, such as pD_{2d}, C_{2v}, and C_{3v}. The symmetry lowering is introduced by ad-hoc distortion along

the high symmetric axis of T_d symmetry. The local symmetry is interpreted in terms of the relative position of four Te-neighboring atoms of the defect site (Figure 4.4). The choice of initial configuration becomes very important in cases where the point defects adiabatic potential energy surface (APES) generally has several local minima. We calculated that the vacancy structure with local symmetry of T_d, C_{2v}, and pD_{2d} are stable. The T_d symmetry structure is calculated to be the global minima. The T_d symmetry structure is lower in energy than that of C_{2v} and pD_{2d} symmetry by 0.48 eV and 2.25 eV, respectively. We found out that the T_d symmetry is stabilized because of the presence of two-hole (polarons) localized on the vacancy defect site. This result of the localized polarons is consistent with the prediction made by Watkins in 1996 for neutral Cd-vacancy in CdTe based on electron paramagnetic resonance (EPR) results[109] and recent DFT result by Kavanagh *et. al.*[103]. In the ground state T_d symmetry configuration, the four Te neighboring atoms move inward by 0.34 Å (13.5%), sustaining the local symmetry (Figure 4.4). The inter-atomic distance between the four Te-atoms neighboring V_{Cd} reduces by 13.5% in respect of the CdTe pristine lattice.

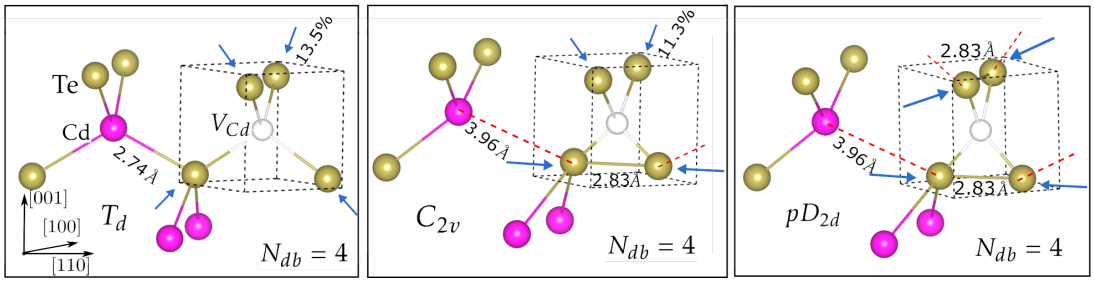

Figure 4.4: Cd-vacancy (V_{Cd}) geometry parameters of the ground state T_d symmetry and metastable C_{2v} and D_{2d} symmetry structure. V_{Cd}, Cd and Te atoms are shown with white, pink, and olive spheres, respectively. Blue arrows represent the displacement of defect site Te neighboring atoms. Dashed red lines shows broken Cd-Te bonds in C_{2v} (2) and D_{2d} (4) symmetry structure with respect to T_d symmetry

The C_{2v} symmetry is characterized by the formation of a Te-Te dimer along the $< 110 >$ axis, as shown in Figure 4.4. The two Te atoms bonded together displace inward along $< 110 >$ axis (family vectors) by 0.85 Å (61%). The bond length of the Te-Te dimer is 2.83 Å. In comparison, the Cd-Te bond length in pristine CdTe structure is 2.74 Å. The other two atoms are displaced inward by 0.28 Å along $< 111 >$ axis (family vectors) and remain three-fold coordinated. Interestingly, the Te atoms forming dimer are also three-fold coordinated as their inward displacement leads to the breaking of one of the three Cd-Te bonds. Similar to the C_{2v} symmetry case, the D_{2d} symmetry structure is characterized by two Te-Te bonds formation with all four atoms relaxing

inward along the < 110 > axis. The symmetric Te-Te bond distance for the two dimers is 2.83 Å. Also, all four Te atoms neighboring Cd-vacancy remains three-fold coordinated, each breaking one of the Cd-Te bonds.

V_{Cd} Electronic structure

The ground state T_d symmetry configuration is characterized by the singlet a_1 state lying deep in the valence band (Figure 4.5). The triplet t_2 state lies just above the valence band minima (VBM) with a very small splitting between the spin-up and spin-down states such that spin-up and spin-down states lie at 24 meVs and 58 meVs above VBM, respectively. The T_d symmetry structure with non spin-polarised calculation shows a metallic character such that the Fermi level lies below the occupied defect electronic levels by 10 meVs in the band gap. The calculated metallic character is consistent with the previously reported DFT results based on LDA calculations[89,108,110]. The spin-polarised solution is 18 meV more stable than the metallic solution. The triplet state in the spin-up channel is completely filled, whereas in the spin-down channel, there are two empty states representing localized holes. Therefore, the T_d symmetry ground state structure is represented by a net spin value of S=1. The ground state T_d symmetry structure with small spin-splitting is a semi-conducting solution. In T_d symmetry ground state structure with spin S=1, of the six localized electrons in the vacancy, two occupy electronic state deep in the valence band, and 4 populate quasi-degenerate (near-degenerate spin split states) 3 electronic states in band-gap, one doubly occupied state, and two singly occupied states. These singly occupied electronic state can accommodate two electrons, and thus Cd vacancy act as a double acceptor. The relative position of these electronic states to valence band maxima (VBM) suggests that it may act as a non-shallow electron and hole trap. In fact, previous studies with both LDA and HSE06 hybrid functional have also suggested double acceptor character[89,100,101,108]. A comprehensive mechanism explaining the non-radiative recombination activity of Cd-vacancy was recently proposed by Kavanagh *et. al*[103].

Lower symmetry structures are characterized by strong degeneracy breaking of sp^3 symmetry and triplet t_2 states. C_{2v} symmetry structure is characterized by an electronic structure with all electronic states present in the valence band completely filled and all states in the conduction band as empty (Figure 4.5). There are no localized defect states present in the band gap. This results from the splitting of triply-degenerate t_2 defect states and change in their character driven by Jahn-Teller distortion. Defect states in C_{2v} symmetry are spin-degenerate and do not show any splitting based on spin-channel. The sp^3 symmetry breaking changes the character of four defect states into a pair of two

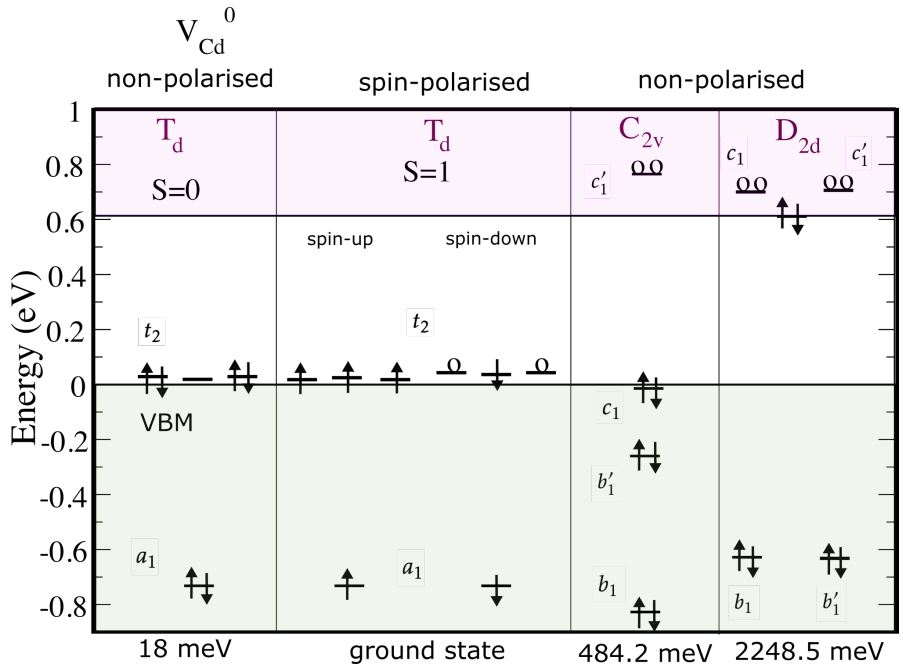

Figure 4.5: Defect states (and host band state) hosting V_{Cd} 6 electrons corresponding to T_d symmetry both spin-polarised and non-polarised solution with C_{2v} and D_{2d} symmetry non-spin polarised electronic structure. Electrons are shown with arrows and empty states are shown with hollow circles. The defect states close to the valence band are not scaled in energy for graphical reasons as they lie in less than 50 meV range to band-edge

bonding type states and two anti-bonding states. We have referred bonding type states as b_1 and b_1' and anti-bonding states as c_1 and c_1'. This splitting of vacancy defect states is similar to the Silicon vacancy electronic structure in -1 charge state, as proposed famously by Watkins[107]. The Symmetry lowering into C_{2v} results in the splitting of bonding-type defect states into two non-degenerate singlet states (b_1 and b_1') occupied by four electrons lying resonant in the valence band at 0.24 eV and 0.82 eV below VBM. The anti-bonding states are split into doubly occupied singlet c_1 and an empty singlet state c_1', lying in the band-gap and conduction band, at 0.052 eV below VBM and 0.18 eV above conduction band minima (CBM), respectively. On the other hand, pD_{2d} symmetry structure have completely filled degenerate bonding-states b_1 and b_1' lying at 0.43 eV below VBM. The two anti-bonding states are also degenerate and empty, positioned at 0.1 eV above CBM. Two of the six vacancy electrons hosted by the V_{Cd} defect center are occupied in a bulk-like state resonant in the CBM (and thus result in a metallic solution). Therefore pD_{2d} symmetry structure has a double donor

character. The calculated electronic character matches well with the previously reported by Orellana *et. al.* based on 216 atom supercell HSE06 functional calculations[21].

Consistent with the previously reported results based on LDA[89,108], we calculated a +2/0 ionization level of the Cd-vacancy defect lying at the edge of the valence band. However, this result does not agree even qualitatively with the previously reported values of 0.36 eV above VBM from the HSE06 hybrid functional[103], which also corresponds well to the single thermal ionization level observed at 0.3-0.4 eV above VBM in experiments[111,112]. One of the reasons for the difference in the ionization level values calculated from LDA by us and the reported hybrid functional results is the different ground state symmetry of Cd-vacancy as obtained using two functionals. The local structure with C_{2v} symmetry is reported as the ground state in HSE06 calculations with energy stabilization of 0.52 eV over T_d symmetry[103]. Although, in terms of topology, the results match quite well from our LDA and the reported HSE06 calculations[89,103,108]. One reason that could derive the energy difference between the Cd vacancy local structures (with different symmetry) from the two different functionals could be attributed to the strain field and bond-strength treatment in the two cases. We reckon that in the case of our LDA calculations, the energy lost because of the Cd-Te bond breaking as calculated in the case of pD_{2d} and C_{2v} symmetry structure must be significantly larger than the energy gained by Te-Te dimer formation. However, this energy order must be different in the case of HSE06 calculations.

To compare our LDA functional calculations results with that of hybrid functionals, we also calculated the ground state symmetry structure of Cd-vacancy using PBE0 hybrid functional. In this case, we also obtained C_{2v} symmetry structure to be 966 meV more stable than the T_d symmetry structure. Although, distortion around the vacancy site brought by the C_{2v} symmetry relaxed structure in a 216 atom supercell PBE0 functional calculation is not local in character. In contrast, we found out that the Jahn-Teller distortion corresponding to C_{2v} structure from LDA calculations in 216 atom supercell does not progress far away from the defect site and is local in character (Figure 4.6). In our understanding, the strain field resulting from the Jahn-Teller distortion is not accounted for properly in 216-atom supercell PBE0 hybrid functional calculations. Such an extended strain field in the supercell will result in large interaction between defect images under the periodic boundary treatment[113]. Therefore a larger supercell may be required to account for proper ground state electronic structure calculation using PBE0 hybrid functional.

The computational task (resource and time) for a larger supercell will increase and scale as N^3 (N is the number of atoms in the supercell, which will become $(4/3)^3$ fold in a larger supercell). Keeping in mind the computational cost of hybrid functional

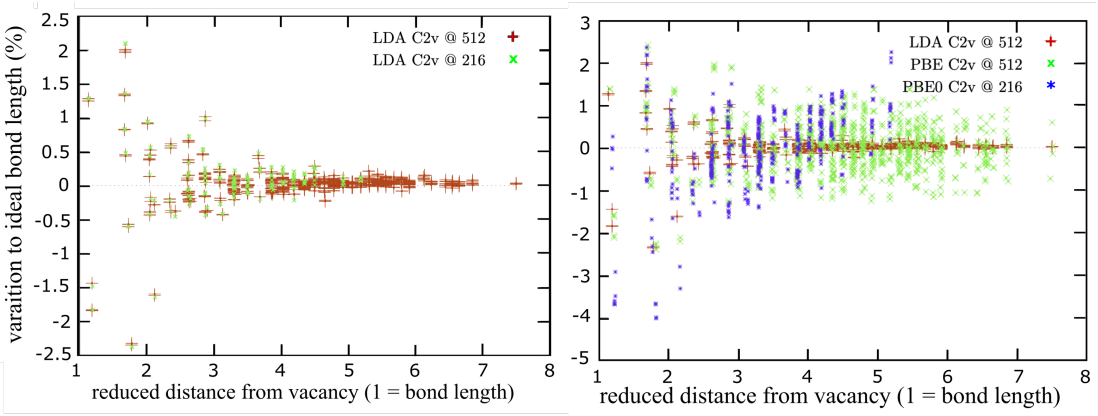

Figure 4.6: Extended strain field represented using Cd-Te bond-length for all atoms as a function of distance from vacancy corresponding to C_{2v} symmetry structure in 216 and 512 atom supercells with LDA, PBE, PBE0 exchange-correlation functionals.

calculations, we, therefore, have chosen to do our (qualitative) analysis of the Se role in defect passivation of CdTe performance limiting defects using LDA 216 atom supercell calculations. Moreover, for the Cd-vacancy case, T_d symmetry structure, as obtained using LDA calculations, has an active acceptor character, which is not true for C_{2v} symmetry structure. Also, the recombination activity of the vacancy defect is reported to be dependent on both C_{2v} and T_d symmetry structure by Kavanagh *et. al*[103].

Te-antisite

Te-antisite (Te_{Cd}) is modeled by replacing a regular Cd site atom, with a Te atom. This initial structure has a T_d symmetry, such that Te_{Cd} has 12 electrons localized on the defect center. Six electrons are contributed by four Te-neighbours and six by Te_{Cd} atom. Eight of these electrons are occupied in defect states resulting from the sp^3 type bonding interaction among the four neighboring Te-atoms. The other four electrons are occupied in a singlet a_{1c} (2) and triply degenerate t_{2c} (2) defect states. These states are anti-bonding in character. Unlike the case of Cd vacancy, the potential energy surface of the local structure of Te_{Cd} is rather simple. The ground state of Te_{Cd} is characterized by a stable C_{3v} local symmetry with energy stabilization of 0.92 eV over T_d symmetry structure. The local symmetry configuration of Te_{Cd} reported previously using LDA[114,115], hybrid functionals HSE[106] and HSE06[72,89,99] is consistently the same.

The symmetry lowering from T_d to C_{3v} is driven by Jahn-Teller distortion brought by relative displacement of the Te_{Cd} atom off the Cd-site into plane formed by the three (of four) Te-neighboring atoms (Figure 4.7). The displacement of Te_{Cd} atom is along

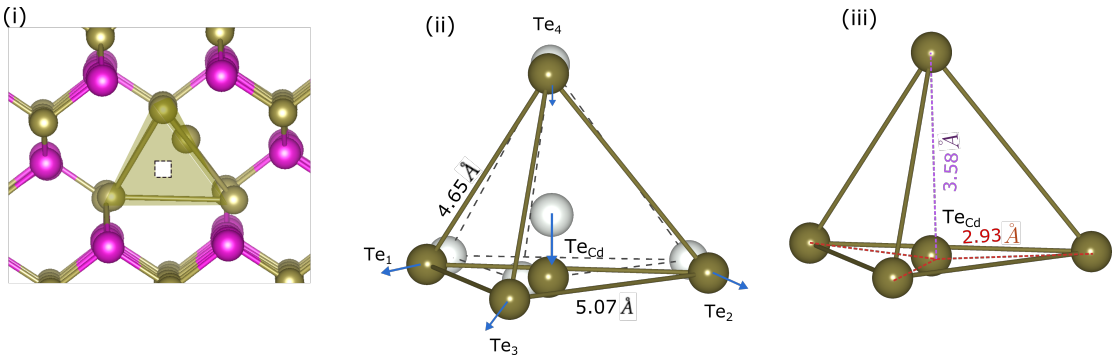

Figure 4.7: (i) Te-antisite Te_{Cd} C_{3v} symmetry structure presented in Te-tetrahedron (shown in translucent olive), small white box represent V_{Cd} site. (ii) Geometric position (and parameters) of Te_{Cd} defect shown with solid olive spheres with respect to the position of Te-atoms in T_d symmetry structure (shown as white spheres); blue arrows show the relative displacement in optimized geometry. (iii) Te_{Cd} atom distance from four neighboring Te-atoms.

the axis (< 111 > crystal symmetry axis) joining the fourth atom (marked as Te_4) and Te_{Cd} atom, which is perpendicular to the plane formed by the three neighbors (marked as Te_1, Te_2, and Te_3 in Figure 4.7). This movement places the Te_{Cd} atom at the center of the triangle (in the same plane) formed by three neighbors. As a result of Te_{Cd} atom displacement, the three neighboring atoms bonded to Te_{Cd} are further pushed outward by 0.31 Å. This increases their inter-atomic distance by 0.52 Å (11.2%). The distance between Te_{Cd} atom and the closest neighboring three atoms is 2.93 Å and that from the farthest Te-atom of the enclosing Te-tetrahedron is 3.58 Å (increased by 30.6% in comparison to pristine Cd-Te). In comparison, the Cd-Te pair distance in the pristine CdTe lattice is 2.74 Å.

Te_{Cd} electronic structure

In the ground state C_{3v} symmetry structure, all four defect electronic states of bonding character are present deep in the valence band. The C_{3v} symmetry breaking also leads to degeneracy uplifting of sp^3 bonding states into sp^2 and a s-type singlet[116]. The reason behind this degeneracy uplifting is the three-fold coordination of Te_{Cd} atom (Figure 4.7). Although, it is anti-bonding type defect states, which are of primary interest as they are responsible for the Jahn-Teller distortion and active electronic structure of Te_{Cd}. The singlet defect state corresponding to sp^2 coordination b_{1c} lie 0.44 eV below VBM (Figure 4.8 (i)) and the singlet defect state b_{2c} involving (anti-bonding) Te_4

atom is placed at 0.19 eV above VBM. The doubly degenerate e_c empty defect states are positioned at 0.73 eV above CBM.

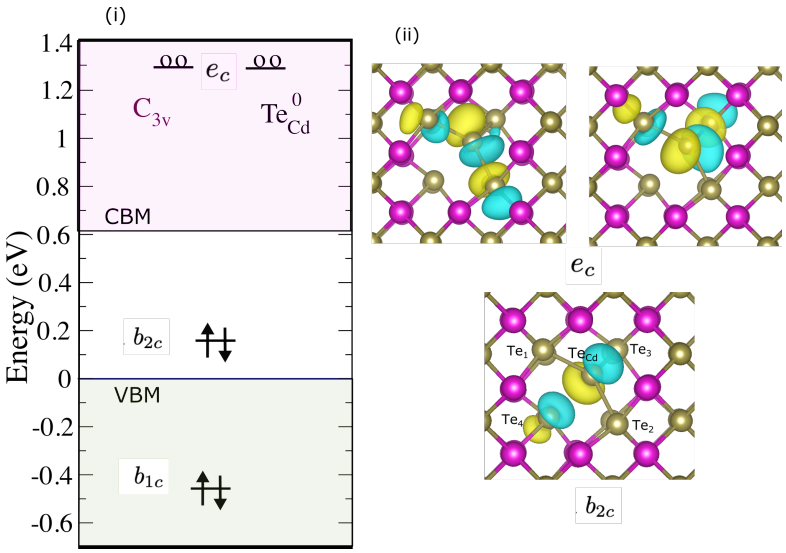

Figure 4.8: (i) Position of anti-bonding defect states of Te_{Cd} in C_{3v} symmetry shown in respect of host band-edges. (ii) Kohn-Sham wavefunction plots of defect states lying in band-gap and above conduction band with an electron density value of 0.005 e/Å^3.

The wavefunction plot corresponding to the b_{2c} defect state suggests that it is responsible for the anti-bonding interaction between the Te_{Cd} atom and the farthest Te atom on Te-tetrahedron around antisite (Figure 4.8 (ii)). This anti-bonding interaction explains the displacement of Te_{Cd} atom (away), increasing the distance between the atoms (Te_{Cd} and Te_4) on which b_{2c} defect state is localized (Figure 4.7). The degenerate e_c defect states are characterized by the anti-bonding interaction of Te_{Cd} atom and three nearest Te-neighbors (Figure 4.8 (ii)). The position of localized b_{2c} anti-bonding defect state in previous LDA and HSE06 combined study by Lindström *et. al.* was reported as 0.16 eV above VBM for LDA and 0.23 eV above VBM for hybrid functional (HSE06) calculations[89].

The doubly occupied anti-bonding defect state (b_{2c}) present in the band-gap represents that Te_{Cd} can capture two holes, meaning it can easily give away two electrons. As this defect state lies deep in the band gap, it may act as a deep donor. The ionization level corresponding to the conversion of Te_{Cd}^{0} neutral charge state to +2 charge state Te_{Cd}^{2+} (characterized by T_d symmetry) is calculated as to lie 0.21 eV above VBM. This reflects a deep double donor character of neutral Te_{Cd} defect. This value is close to the previously reported values (~ 0.32 eV) based on LDA calculations[89,114,117]. In the DFT

results reported using HSE06 hybrid functional, the ionization level was calculated to lie 0.55 eV above VBM[72,89]. Whereas the ionization level value reported by Flores *et. al.* with the use of the beyond-DFT GW method is 0.99 eV above VBM[99]. The value reported by Flores *et. al.* from DFT-GW calculations matches with the ionization level of ~ 1.1 eV above VBM as observed in photothermal deflection spectroscopy (PTDS)[118] and Time-Resolved Photoluminescence (TRPL) experiments[90]. In experiments, this level was assigned to Te-antisite as it reflects from the chemical analysis done in Te-rich grown CdTe[119]. Te-antisite with deep double donor character is consistently reported as the main non-radiative recombination center previously in both experiments[120] and DFT calculations[89,99].

4.3.2 Te-interstitial

We have studied primarily only the neutral charge state of the Te-interstitial (Te_i). Since we tend to discuss the Te_i defect to define Te-diffusion in CdTe and Te_i in neutral charge state is proposed to have the lowest diffusion energy barrier in various previous studies[104–106]. In the zinc-blende structure, several interstitial sites are possible. We considered a number of high symmetry interstitial sites in lattice, namely the two tetrahedral symmetry site configurations with the nearest neighbor four i)regular Cd ($Te_i^{Tet_{Cd}}$) and ii)Te site atoms ($Te_i^{Tet_{Te}}$), hexagonal site configuration (Te_i^{hex}), split interstitial at Cd and Te sites.

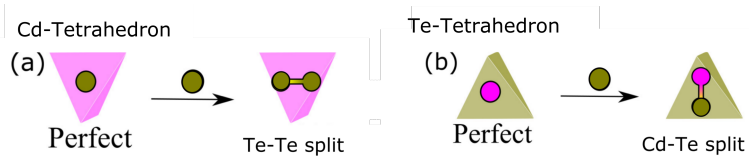

Figure 4.9: Schematic representation of split interstitial at Te-site (Cd-tetrahedron) and Cd-site (Te-tetrahedron)

The split interstitial configuration is characterized by an interstitial atom displacing a regular lattice site atom such that they form a bond ($(Te_i - Te)_{Te}$ and $(Te_i - Cd)_{Cd}$) being placed on either side of the regular site (Figure 4.9). We calculated that the split interstitial configuration of Te-Te aligned along $< 110 >$ directions ($(Te_i - Te)_{Te}^{[110]}$) has the lowest formation energy among the high symmetry interstitial configurations. A similar observation about the stability of the split configuration of Te self-interstitial was made by Du *et. al.*[114]. The Te-Te split interstitial along the $< 001 >$ directions ($(Te_i - Te)_{Te}^{[001]}$) is higher in energy by 0.33 eV. The Cd-Te split interstitial ($(Te_i -$

$Cd)_{Cd}^{[001]}$) has slightly higher formation energy (0.14 eV) in configuration aligned along $< 001 >$ directions and has a saddle point character on the PES of the Te_i defect. The pure interstitial Te_i coordinated to Cd-atoms (Te_i^{TetCd}) is higher in energy than the $(Te_i - Te)_{Te}^{[110]}$ configuration by 1.92 eV and Te_i tetrahedrally coordinated to Te-atoms (Te_i^{TetTe}) is not stable.

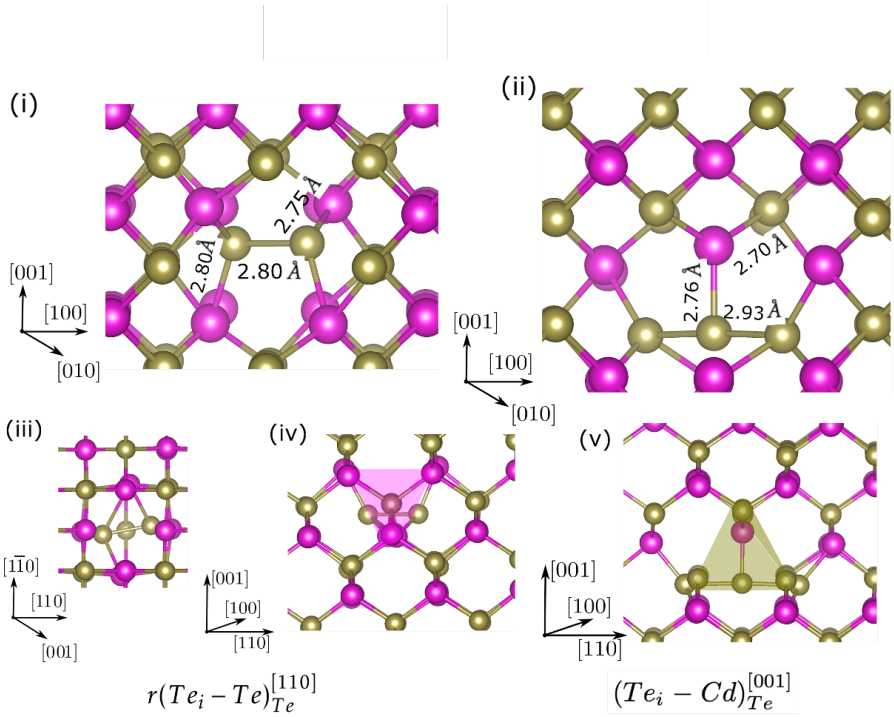

Figure 4.10: (i) bond distances of lowest energy Te-Te split interstitial configuration rotated by 10.7 degrees from [110] axis. (ii) bond-distance of Cd-Te split interstitial perfectly aligned along [001] axis. (iii) pictorial view showing rotation of Te-Te split configuration from [110] axis. (iv) and (v) models showing Te-Te split and Cd-Te split configurations in Cd-tetrahedron and Te-tetrahedron, respectively. For each panel axis-diagram represents the corresponding axis orientation

A configuration (Figure 4.10 (i)) with 28 meV further lower energy than the high symmetry ($(Te_i - Te)_{Te}^{[110]}$) split interstitial configuration is also calculated. This configuration is slightly displaced from the high symmetry configuration of $(Te_i - Te)_{Te}^{[110]}$ (having C_{2v} symmetry) with a rotation of 10.7 degrees reducing symmetry to C_2 (Figure 4.10 (iii)). We have referred to this lower symmetry configuration as $r(Te_i - Te)_{Te}^{[110]}$. The Cd-Te bond-length values representing this lowest energy configuration are shown in Figure 4.10 (i). The bond-length values are close to symmetric and Cd-Te bond length value of 2.74 Å in pristine CdTe lattice. This configuration is also displaced in

[001] direction by 0.58 Å in comparison to the Te-site position in the pristine lattice. In contrast, $(Te_i - Cd)^{[001]}_{Cd}$ split configuration is perfectly aligned and does not show any further lowering in energy through C_{2v} (symmetry) breaking. The Cd-Te bond lengths corresponding to split interstitial are shown in (ii) panel of Figure 4.10.

For the calculation of the diffusion path of Te_i, we have considered high symmetry $(Te_i - Te)^{[110]}_{Te}$ interstitial as the initial configuration, since the energy difference is very small from $r(Te_i - Te)^{[110]}_{Te}$ and obvious high symmetry reason.

4.3.3 Se doping defects in CdTe

Se substitution at Te-site (Se_{Te})

Se is iso-valent to the Te-atom and replaces the Te-atom on its regular site and brings about a symmetric very small 0.14 Å local inward distortion in the lattice. The T_d symmetry is maintained (Figure 4.11). Due to its isovalent nature and larger electronegativity in comparison to the Te-atom, Se does not introduce any defect state in the band gap. A moderately localized state corresponding to Se_{Te} defect resonant in the conduction band is calculated. The defect state is situated at 1.08 eV above CBM.

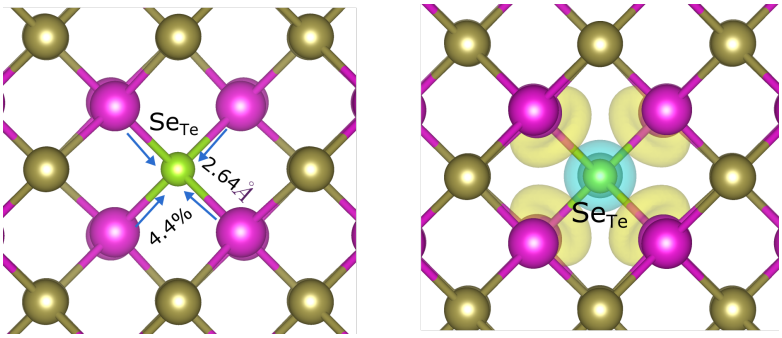

Figure 4.11: (i) Ground state configuration of Se_{Cd} showing symmetric inward relaxation and Se-Cd bond length. (ii) Localised defect state wavefunction of Se_{Te} defect state wavefunction located in conduction band with an electron density value of 0.0018 e/Å^3.

Se substitution at Cd-site Se_{Cd}

Se_{Cd} has a similar electronic structure to Te-antisite (Te_{Cd}), with Se atom shifting off from the substitutional site, and is 1.49 eV less stable than the Se_{Te} defect in Te-rich limit. This defect results from the interaction of Se-interstitial interaction with Cd-vacancy, and therefore the electronic structure is discussed in the later section 4.5, where

defect complexes resulting from the diffusing Se interstitial interaction with Cd vacancy are discussed.

Se-interstitial

For the Se interstitial defect atom, the different high symmetric position shows a similar adiabatic potential energy surface as in the case of the Te-interstitial defect. The split interstitial defect at Te-site, such that Se_i displaces the regular Te-site atom forming an asymmetrical dumbbell $(Se_i - Te)_{Te}$, is most stable. In its ground state, the dumbbell is aligned along the $< 110 >$ direction (off-rotated), as shown in Figure 4.12. The Se interstitial split configuration at Cd-site ($(Se_i - Cd)^{[001]}_{Cd}$) aligned along $< 001 >$ direction is slightly higher in energy by 0.18 eV. In comparison, other interstitial defects are much higher in energy, like the hexagonally (Se_i^{hex}) coordinated interstitial (1.27eV) and the one with tetrahedrally coordinated with Cd atoms ($Se_i^{Tet_{Cd}}$) (1.62 eV).

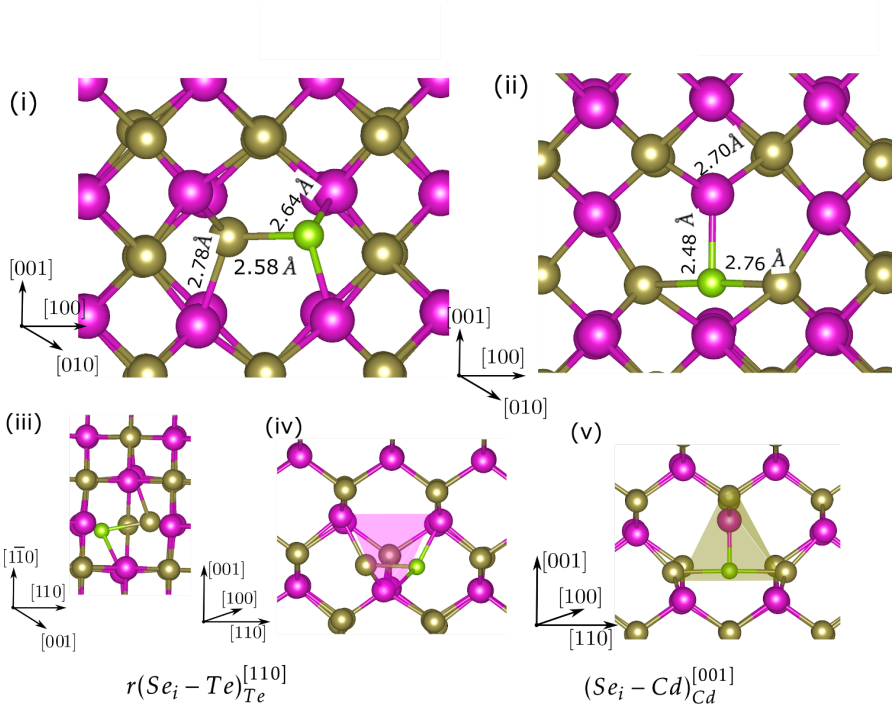

Figure 4.12: (i) and (ii) Important bond-length parameters corresponding to $(Se_i - Te)^{[110]}_{Te}$ (off rotated) and $((Se_i - Cd)^{[100]}_{Cd})$ split interstitial respectively. (iii) graphical view representing rotation of $(Se_i - Te)^{[110]}_{Te}$ by 12.2 degrees. (iv) and (v) respective view of Se-Te and Se-Cd split interstitial in Cd-tetrahedron and Te-tetrahedron.

Similar to the case of Te_i, the lowest energy configuration, $r(Se_i - Te)^{[110]}_{Te}$ (Figure

4.12 (i)) is the one displaced off from the high symmetry structure of $(Se_i - Te)^{[110]}_{Te}$ configuration. This configuration has lower energy of 47 meV and is rotated by 12.2 degrees (Figure 4.12 (iii)) in respect of $(Se_i - Te)^{[110]}_{Te}$ configuration. $Se_i - Te$ forms a strong and shorter (2.58 Å) bond in comparison to the anion Te-Te bond (2.80 Å in Te-Te split). Also, Se-Te bond lengths are shorter than Cd-Te bond lengths by ~ 0.14 Å (Figure 4.12 (i)). Se forms shorter bonds due to large electronegativity and small atomic radii. The split interstitial is displaced along the [001] axis by 0.48 Å in comparison to the Te atom position in the pristine lattice. Although the Se-Te bond length in the case of $(Se_i - Cd)^{[001]}_{Cd}$ split interstitial are larger than Cd-Te bond lengths (Figure 4.12 (ii)) derived by asymmetric displacement of Se (~ 2.20 Å) to Cd atom (~ 0.65 Å) from regular Cd-site position in pristine lattice.

Following the small energy difference between $r(Se_i - Te)^{[110]}_{Te}$ and $(Se_i - Te)^{[110]}_{Te}$ configurations we will use high symmetry $(Se_i - Te)^{[110]}_{Te}$ as initial configuration as Se_i diffusing defect.

4.4 Diffusion process of Te-self diffusion and Se impurity diffusion in CdTe

Understanding of diffusion path of Se interstitial (Se_i) and the associated energy barrier of diffusion is very important to decipher the deep segregation of Se into CdTe grain and as well the impact of Se presence at the atomic level in electronic terms. We first studied the self-diffusion of Te_i and then used the developed understanding to propose a new diffusion mechanism (for zinc-blende lattice) to define the Se_i diffusion in CdTe bulk. The diffusion paths of both chalcogenide atoms are proposed using calculations based on nudged elastic band (NEB) method[97]. The method helps in finding the saddle point configuration along the diffusion path for the migration of a defect from one site in the lattice to an adjacent site. The barrier to migration from one site to another is defined as ΔE_m, which is the energy difference between saddle point configuration and defect ground state. The corresponding diffusion rate is proportional to $exp(-\Delta E_m/K_B T)$. According to Lordi *et. al.*, in the case of CdTe at room temperature, point defects with a barrier value of ~ 0.25 eV are highly mobile, with a barrier value of ~ 0.5 eV are moderately mobile. The defects with a migration barrier value of ~ 1.0 eV need a high temperature of 1000 °C to be moderately mobile[106].

4.4.1 Te-interstitial diffusion

The most straightforward diffusion mode in a number of zinc-blende lattice materials is interstitial diffusion along [110] channel and related symmetry equivalent directions[104]. For the Te_i defects, split interstitial $(Te_i - Te)^{[110]}_{Te}$ has the lowest formation energy. Therefore, it is very much plausible that the Te-Te split configuration must be the defect configuration that drives the diffusion of Te in the CdTe grain. The Te-interstitial configuration of $(Te_i - Cd)^{[001]}_{Cd}$ with second lowest energy and saddle point character (that relaxes to $(Te_i - Te)^{[110]}_{Te}$ on optimization) could then be assumed as an intermediate state present along the path facilitating Te diffusion. We performed NEB calculations in a 64-atom supercell considering the $(Te_i - Te)^{[110]}_{Te}$ and $(Te_i - Te)^{[\bar{1}\bar{1}0]}_{Te}$ split interstitials as the initial and final configuration of the NEB diffusion step/path (Figure 4.13). The two configurations essentially have the same formation energy as they are identified as being aligned along the symmetric 110-axis of different orientations. The $(Te_i - Cd)^{[001]}_{Cd}$ split interstitial is identified as the saddle point corresponding to this diffusion step.

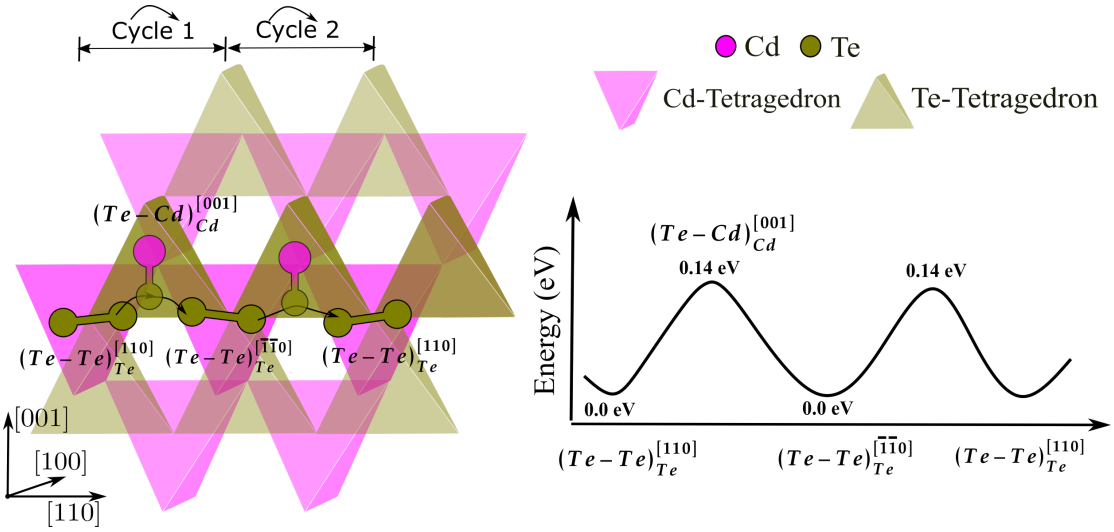

Figure 4.13: On left Pictorial representation of $(Te_i - Te)^{[110]}_{Te}$ split interstitial translation movement from the end of a Te-tetrahedron to another with consecutive linear diffusion step. Arrows represent each step in the diffusion process. (Right) Energy graph corresponding to linear diffusion process showing the energy of saddle point configuration (on top of maxima point) with respect to the energy of minima.

This diffusion step can repeat and lead to the formation of the final configuration $(Te_i - Te)^{[110]}_{Te}$ split, the same as the initial configuration of the diffusion path at the end of the second cycle. Therefore this diffusion path can explain a long-range diffusion of Te-interstitial. We refer to this diffusion mode as linear, since diffusing Te_i keeps

its track along the same 110-axis family. To calculate the corresponding barrier for the diffusion from the initial $(Te_i - Te)^{[110]}_{Te}$ to final $(Te_i - Te)^{[\bar{1}\bar{1}0]}_{Te}$ configuration, the energy maxima high symmetry Cd-Te split interstitial configuration is optimized in a larger 216 atom supercell. The height of the migration barrier is calculated as 0.14 eV.

Previously Roehl *et. al.* reported a very high value of 1.2 eV for the Te-interstitial diffusion barrier using LDA functional with diffusion path involving high symmetry Te_i tetrahedral site [104]. More recently, Ma *et. al.* [105] and Yang *et. al.* [121] reported value of $\sim$ 0.09 eV using PBE and HSE06 functionals, respectively for the Te split-interstitial diffusion. Our results correspond well with the diffusion mode suggested in these two studies. We also calculated the diffusion barrier, considering the Te_i^{Tet} and Te_i^{Hex} as diffusing defects. However, the corresponding barriers for Te_i are $\geq$1 eV, and therefore, such diffusion processes are considered unfavorable. We identified another $(Te_i - Te)^{[110]}_{Te}$ interstitial diffusion mechanism, which involves an additional rotation step that allows the diffusing Te-interstitial to access the direction other than the [110]-axis, belonging to the [011] and [101] families of vectors. This diffusion path has a slightly higher barrier than the linear diffusion process and is discussed alongside the diffusion process of Se-interstitial defect later in 4.4.2

4.4.2 Se-interstitial diffusion

We used the study of Te_i diffusion as a basis initial guess to propose the interstitial diffusion path for Se_i. The $(Se_i - Te)^{[110]}_{Te}$ split configuration has the lowest formation energy among the various Se-interstitial configurations. Therefore, it is practical to assume it as the initial configuration for the diffusion process in CdTe bulk. Accordingly, we first considered the linear diffusion process for Se_i as a possible mechanism in a similar manner as defined for the Te-Te split interstitial diffusion step. We identified the energy barrier corresponding to the NEB path with initial $(Te - Se_i)^{[110]}_{Te}$ to final $(Tei - Se_i)^{[\bar{1}\bar{1}0]}_{Te}$ as 0.21 eV (Figure 4.14). The split interstitial $(Se_i - Cd)^{[001]}_{Cd}$ configuration corresponds to the saddle point on the diffusion step. Although, in this case, the initial and final configurations of the split interstitial are different, as the dumbbell is formed by different group VI atoms pair. The initial configuration is identified as the Se-Te split configuration directed along the [110] direction, whereas in the final configuration, Se and Te are swapped in reference to their respective positions in the initial configuration.

As a result, when this chalcogenide atom diffusion step repeats itself, it leads to the formation of the $(Te_i - Te)^{[110]}_{Te}$ split interstitial as the final configuration and a Se_{Te} antisite at the end of the second cycle of the diffusion process. Here we call the

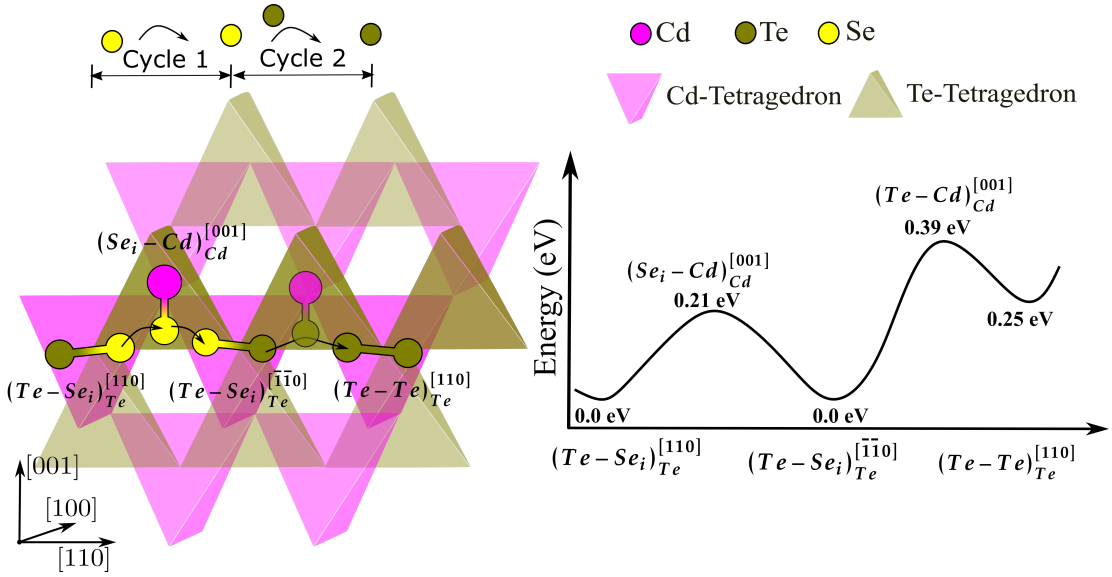

Figure 4.14: On left, two consecutive linear diffusion steps starting with the initial configuration of $(Te - Se_i)^{[110]}_{Te}$ are shown. Se is left trapped at the end of the first step (Cycle 1). (Right) Energy profile of diffusion path showing the energy of saddle point configuration (on top of maxima point) and of local minima (written below the curve).

movement of chalcogenide atom as split interstitial $((Se/Te)_i - Te)^{[110]}_{Te}$ from one end of the Te-tetrahedron to the other as one cycle. Therefore at the end of the second cycle, Se is left behind at Se_{Te} substitutional site. Consequently, this linear diffusion process of $((Se/Te)_i - Te)^{[110]}_{Te}$ split interstitial leaves Se trapped and cannot account for the long-range diffusion of Se in CdTe grain.

To define the Se interstitial long-range diffusion, next, we take motivation from the previously reported case of Cl dopant split interstitial. In this case, a 90-degree rotation step in Cd-tetrahedron along with a kick-out mechanism was proposed by Yang *et. al.*[121] to explain the diffusion path for positively charged $Cl^+ - Te$ split interstitial. A low diffusion barrier of 0.6 eV corresponding to this path was reported using HSE06 functional DFT calculations.

Rotation step of split interstitial at Cd-tetrahedron

We, therefore, then considered a diffusion process with a rotation of Se-Te interstitial in conjunction with the linear diffusion step as the second possible diffusion path. We defined the rotation of chalcogenide Se-Te split interstitial in Cd-tetrahedron as the second step following the first step of linear diffusion of $(Te - Se_i)^{[110]}_{Te}$ to the $(Te -$

$Se_i)_{Te}^{[\bar{1}\bar{1}0]}$ configuration (Figure 4.14 and Figure 4.15). This possible diffusion path is then defined as a combination of the linear part having a diffusion barrier of 0.21 eV and the $(Te{-}Se_i)_{Te}^{[\bar{1}\bar{1}0]}$ rotation step. For the rotation step (Figure 4.15) with $(Te{-}Se_i)_{Te}^{[\bar{1}\bar{1}0]}$ as initial configuration and 90-degree rotated $(Te-Se_i)_{Te}^{[\bar{1}10]}$ as the final configuration, a high energy barrier of 0.95 eV is calculated.

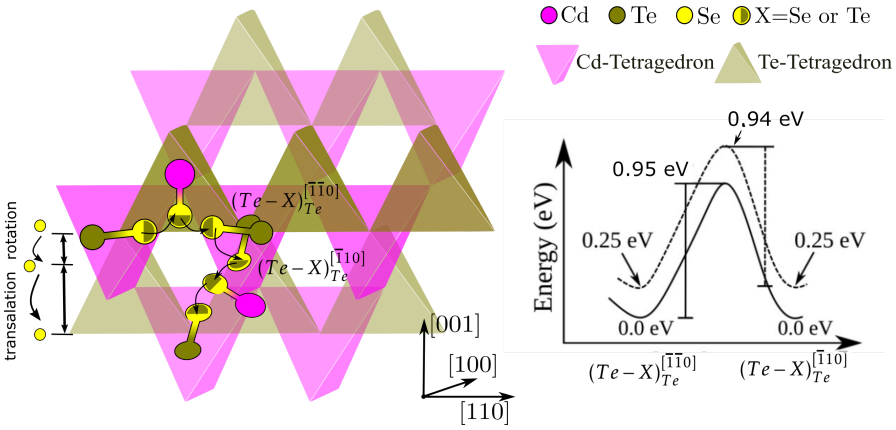

Figure 4.15: Representation of diffusion path involving a 90-degree rotation step of Se-Te split ($(Te-Se_i)_{Te}^{[\bar{1}\bar{1}0]}$) followed by translation diffusion step. The rotation of the split interstitial is followed by another translation step. Arrow represents the consecutive movement of Se in the lattice. On the right, the energy profile corresponding to 90-degree rotation is shown for Se (solid line) and Te (dashed line). The energy barrier height is shown as vertical lines between the minima and saddle point configuration.

This rotation of the Se-Te split interstitial in Cd-tetrahedron thus allows the Se atom to be mobile by means of repeated linear and rotation consecutive steps. Although the total barrier for the diffusion process is 0.95 eV. This barrier height for the diffusion process is very high and thus does not successfully describe the fast and long-range diffusion of Se as observed in experiments[86,122]. The corresponding barrier calculated for the diffusion of self Te-Te split interstitial involving linear diffusion step and rotation step in Cd-tetrahedron is 0.94 eV.

Rotation step of split interstitial at Te-tetrahedron

However, there is a possibility of diffusion of Se by means of rotation movement involving the other Se_i split interstitial defect configuration with formation energy slightly larger than $(Se_i - Te)_{Te}$ interstitial. $(Se_i - Cd)_{Cd}^{[001]}$ split interstitial has a slightly higher energy than $(Te - Se_i)_{Te}^{[110]}$ interstitial configuration for Se dopant in CdTe. This Se_i configuration is also identified as the saddle point along the linear diffusion step of

$(Te - Se_i)^{[110]}_{Te}$ split interstitial (see Figure 4.14). To explain long-range diffusion, we have thus considered the intermediate NEB step of $(Se_i - Cd)^{[001]}_{Cd}$ interstitial 90-degree rotation in Te-tetrahedron (Figure 4.16 (a)). Here, $(Se_i - Cd)^{[001]}_{Cd}$ and $(Se_i - Cd)^{[\bar{1}00]}_{Cd}$ are considered as the initial and final configuration for the NEB step. We identified $(Se_i - Te)^{[010]}_{Te}$ in Cd-tetrahedron (Figure 4.16 (b)) as the maxima (saddle point) along this path with an energy barrier value of 0.19 eV. This value corresponds to the relative energy of saddle point configuration $(Se_i - Te)^{[010]}_{Te}$ with respect to $(Cd - Se_i)^{[001]}_{Cd}$ interstitial in a 216 atom supercell.

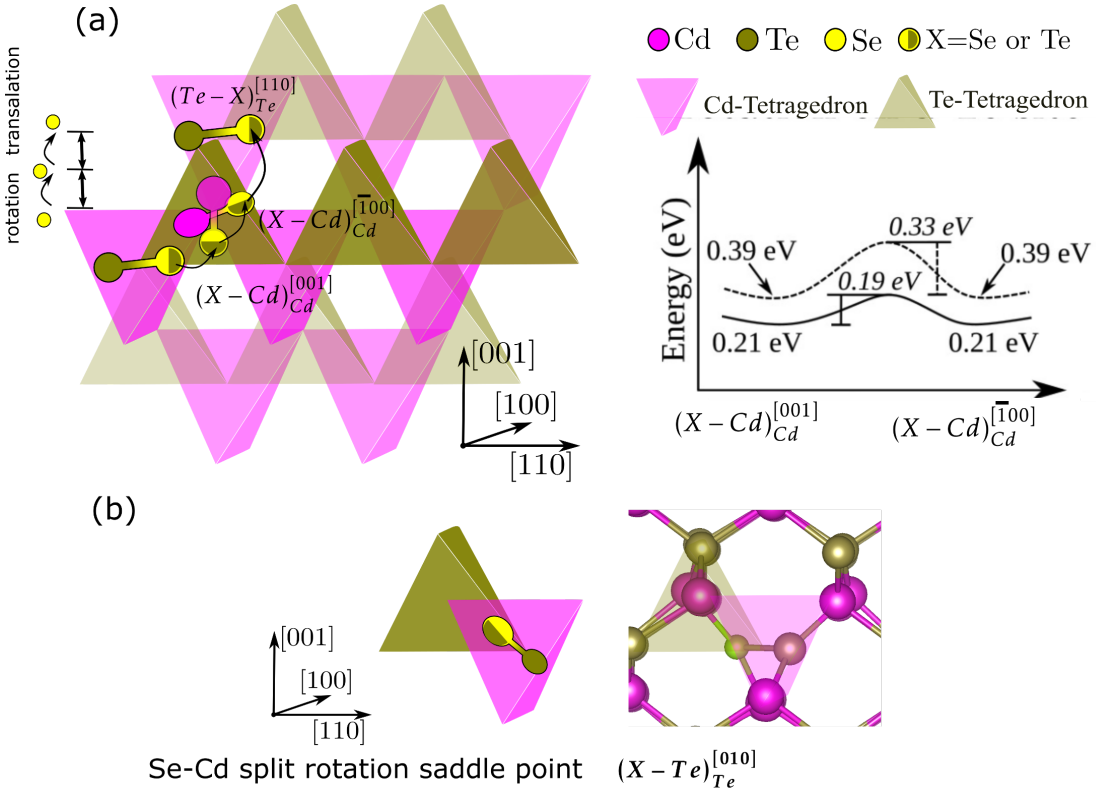

Figure 4.16: (a) Diffusion path of Se presenting low diffusion barrier involving 90-degree rotation of Se-Cd split interstitial, followed and preceded by translation step of split interstitial. (Right) Energy graph representation of chalcogenide Se (solid line) and Te (dashed line) rotation step in Cd-tetrahedron. Barrier heights are shown with vertical lines, and corresponding values are written in italics. (b) Saddle point configuration $(Se_i - Te)^{[010]}_{Te}$ (in Cd-tetrahedron) corresponding to Se-Cd split rotation.

Therefore a diffusion path can be defined such that at the end of the $(Cd - Se_i)_{Cd}$ rotation step, $(Se_i - Cd)^{[\bar{1}00]}_{Cd}$ dissociates and forms $(Te - Se_i)^{[110]}_{Te}$ at another edge of the Te-tetrahedron (Figure 4.16 (i)). Thus at the end of this devised new diffusion

path, initial and final configurations are the same as $(Te - Se_i)^{[110]}_{Te}$. The complete barrier for the diffusion process starting from $(Te - Se_i)^{[110]}_{Te}$ configuration, dissociation step leading to formation of intermediate $(Cd - Se_i)^{[001]}_{Cd}$ configuration and rotation step ($(Cd - Se_i)^{[\bar{1}00]}_{Cd}$) is 0.40 eV (0.21 + 0.19). This diffusion process can repeat itself with a low effective energy barrier and establish a long-range diffusion of Se_i in CdTe grain. In comparison, this diffusion path for Te-self interstitial involving rotation of $(Cd-Te_i)^{[001]}_{Cd}$ split, is less likely with a barrier of 0.33 eV, making the full diffusion process of Te interstitials in volume through linear and re-orientation mechanism around 0.47 eV.

To summarize, a mix of translation and rotation diffusion movements defines the migration path for both the chalcogenides with a low energy barrier in CdTe bulk. The diffusion rate is different for the Te-self interstitial and Se interstitial as defined by the calculated energy barriers. The lowest energy barrier of 0.14 eV, for the case of Te-self interstitial, corresponds to the linear diffusion path involving simple translation movement of $(Te - Te)^{[110]}_{Te}$ split. Whereas the Se_i long-range diffusion is represented by a combination of rotation and translation steps with a collective barrier of 0.40 eV. For the $(Te - Te)_{Te}$ self-interstitial diffusion mechanism involving both translation and reorientation steps, the barrier is relatively higher than both pure translation linear diffusion path of Te-Te split (by 0.33 eV) and $(Se_i - Te)_{Te}$ interstitial diffusion (by 0.07 eV) with the same trajectory. Therefore, Te-self interstitial diffusion through translation motion will be predominant over the reorientation possibility, leading to the fast disappearance of Te interstitial atoms on interfaces or grain boundaries. This interpretation is consistent with the Te-rich clustering region proposed to be present at grain boundaries and interfaces in experiments performed on Te-rich grown samples[123]. However, the Se substitutional atom (CdSeTe alloy) at Te-site can actually moderate this diffusion rate of the Te-interstitial by facilitating the formation of a Te-Se split through a push mechanism. This situation then allows the Te-interstitial atoms to explore a wide volume of CdTe grains with both chalcogenide atoms diffusing as pairs. It has been reported by Kuciauskas *et. al.* by means of combined ab-initio calculations and experimental result analysis that Te_i in CdTe actually can form several defect complexes with Cd-vacancy and Te-antisite defects[120]. Therefore, Se also allows and enhances the Te atoms diffusion as interstitials to the critical isolated Cd-vacancy and Te-antisite defects and the formation of defect complexes.

Next, to understand how Se impacts the electronic structure of critical defects and their recombination activity we then considered the interaction of Te self-interstitial and Se-interstitial with critical Cd-vacancy defects. Depending on the topology of the approaching diffusing defect, several defect complexes with different configurations can form on the chemical reaction of the chalcogenide interstitial with the Cd vacancy.

To compare the energetics of the defect complexes with that of the interacting defect species, we have used standard formation energy formulation[40]. To calculate the formation energy, the total energy of a supercell with a defect is reduced (increased) based on the number of added (removed) atoms to (from) the supercell, times their respective chemical potentials (section 4.2). For this purpose, we defined the chemical potentials of Cd, Te, and Se species based on the CdTe bulk and intrinsic defects. According to the convention, we defined the chemical potential of the Cd-Te pair using the CdTe bulk. Next, we defined the chemical potential for Cd and Te atoms using the Cd-vacancy defective supercell total energy. This choice is based on the fact that we want to describe crystals grown in Te-rich conditions where Cd-vacancies are constitutional defects. This way, Cd-vacancy defective supercell complemented with Cd-Te pair chemical potential set up chemical potential values for the two species. We, therefore, used CdTe bulk and Cd-vacancy as a reference and equated their total energy as zero defining in this manner the chemical potential of Te and Cd atoms. For the chemical potential of Se, since Se diffuses as an interstitial, we defined the diffusing $(Se_i - Te)^{[110]}_{Te}$ interstitial with the lowest formation energy as the reference for Se chemical potential. Therefore Se-Te split interstitial total energy is set to zero, and the formation energy of all defect complexes involving the Se atom is calculated based on that.

4.5 Se interaction with critical V_{Cd} and Te_{Cd} defects and passivation

The diffusion mechanism of both chalcogenide Se and Te atoms is discussed in the previous section 4.4. Both the chalcogenide can diffuse with significant ease in CdTe bulk. Split $(Se_i - Te)^{[110]}_{Te}$ is the main diffusing defect that assists the chalcogenide diffusion. In other words, this defect is very diffusive with a low diffusion barrier (0.40 eV) such that it can diffuse to reach isotropically deep in the CdTe grain. These diffusing chalcogenide defects can then interact with the intrinsic defects such as V_{Cd} and Te_{Cd} and make defect complexes. These defect complexes can alter the carrier recombination activity (electronic defect states) of critical intrinsic V_{Cd} and Te_{Cd} defects and, as a result, may lead to the passivation of these defects. Defect complex formation affects the defect-related levels and thus changes their position with respect to band-edges. This change in the position of defect electronic levels (closer or into band-edges) of active defects could change the carrier capture rates and thus may reduce the non-recombination activity of critical defects[124].

Interaction of diffusing defect $(Se_i - Te)^{[110]}_{Te}$ with the V_{Cd} shows that it is the Te atom

among the two chalcogenide atoms which preferably diffuses into the corresponding chalcogenide tetrahedron to occupy the vacancy site (Figure 4.17). The interaction of $(Se_i - Te)_{Te}$ split diffusing defect with V_{Cd} results in three unique configurations depending on the approach trajectory of Se/Te chalcogenide split close to V_{Cd} site (small pink tetrahedron on the left panels in Figure 4.17). In the case where Se gets trapped (section 4.4.2) at the Te substitution site in close vicinity and diffusing $(Te_i - Te)_{Te}$ approaches to the V_{Cd}, the resultant defect complex is a Te-antisite (Te_{Cd}), as shown in Figure 4.17 (b) (with Te-atom displaced off from the vacancy site). This scenario is based on the assumption that the major part of the diffusion of Te_i atom close to V_{Cd} site is facilitated by the Se atom. On the other hand, when $(Se_i - Te)_{Te}$ approaches the V_{Cd}, it leads to the formation of two stable defect complex configurations that can be referred to as Se_{Cd} and $Te_{Cd} - Se_{Te}$ (Figure 4.17 (a) and (c)). (Antisite defects Te_{Cd} and Se_{Cd} here are referred to as defect complexes as they result from the reaction of diffusing chalcogenide interstitial with V_{Cd}. Although, they can form as isolated point defects in Se alloyed CdTe bulk.)

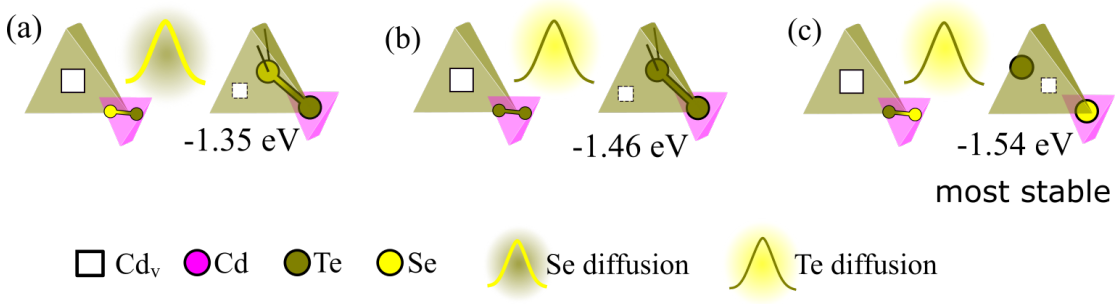

Figure 4.17: Three unique configurations resulting from the interaction of Se_i approaching the V_{Cd} defect and their respective formation energies (in eVs). The type of chalcogenide atom involved in the last diffusion step is coded by a golden or yellow barrier symbol, while its exact topology is described inside the small pink tetrahedron.

The resulting configurations are equivalent to an anti-site where the chalcogenide atom is displaced within a Te tetrahedron face adopting a C_{3v} symmetry as for the Te_{Cd}. In all final configurations, the chalcogenide atom is displaced along a $< 111 >$ direction inside the vacancy. All three defect complexes have negative formation energy less than -1.3 eV with respect to the choice of our chemical potentials. The formation energy values suggest that these defect complexes are very stable in comparison to the Cd-vacancy constitutional defects. Comparing the energetics, Se_{Cd} (-1.35) is less stable than Te_{Cd} (-1.46) because of two reasons i) first, Se is more electronegative, which leads to strong coulomb repulsion (yet Se form strong Se-Te bonds) among the Se_{Cd}

atom and Te atoms sitting on edges of Te-tetrahedron and (ii) second, smaller atomic radii size of Se atom with respect to Te atom. The high stability of $Te_{Cd} - Se_{Te}$ (-1.54) can be explained on the basis of the high stability of Se_{Te} and Te_{Cd} defect. The energy required to form strong anion-anion bonds in the case of Se_{Cd} (2.74 Å) destabilizes it in comparison to Te_{Cd} (2.93 Å). Whereas strong cation-anion bonding provides more stability in the case of $Te_{Cd} - Se_{Te}$ (2.56 Å) over Te_{Cd} (2.74 Å).

Stable defect complexes resulting from this interaction of split $(Se_i - Te)_{Te}$ interstitial defect with V_{Cd} have a similar electronic structure to Te_{Cd} with a characteristic anti-bonding electronic state that drives C_{3v} local symmetry. This defect state results from antisite atom interaction with one of the four chalcogenide atoms sitting at Te-tetrahedron (Figure 4.19 and Figure 4.18). These interactions lead to the passivation of three dangling bonds present in the V_{Cd}. One dangling bond still remains, driven by anti-bonding interaction. In the case of the antisite defect complexes (Figure 4.18), there are no longer any singly unoccupied electronic levels present in the band gap. This results from the occupation of singly-unoccupied states of V_{Cd} by the electrons of the chalcogenide antisite atom. For the Te_{Cd} defect, the corresponding anti-bonding defect state is present at 195 meV above VBM. This defect state is responsible for the non-radiative recombination carrier trap activity of the Te_{Cd}. The defect is a deep double donor due to the presence of two electrons occupying the anti-bonding defect state. In the other two cases of chalcogenide antisite configurations, where the Se atom is involved in the anti-bonding interaction, the corresponding defect electronic state is shifted lower in energy and close to VBM.

Quantitatively, the anti-bonding defect state moves to a value of 48 meV above VBM in the case of $Se_{Te} - Te_{Cd}$, whereas it moves 36 meV below VBM for Se_{Cd}. This change in the anti-bonding state position with respect to the VBM is driven by the reduction in anti-bonding interaction and electronic repulsion between chalcogenide Se and Te atom involved in anti-bonding. These two factors can be qualitatively represented by the wavefunction isosurfaces corresponding to the anti-bonding interaction and the local distortion induced by the defect complex. The Kohn-Sham wavefunction plots for the anti-bonding defect states are shown in Figure 4.19. A significant reduction in anti-bonding interaction is clearly seen in the case of $Se_{Te} - Te_{Cd}$. A downshift of 147 meV in the energy of the anti-bonding electronic state present in band-gap (in reference to Te_{Cd} defect state) for the case of $Se_{Te} - Te_{Cd}$, matches quite well with the previously reported value of 130 meV from more precise GW calculations[99]. The two latter configurations with one Se atom display weak anti-bonding interaction and defect states lying close to VBM, significantly reducing hole-trapping probability. Both are thus expected to be tolerant for solar applications and enhance radiative recombination.

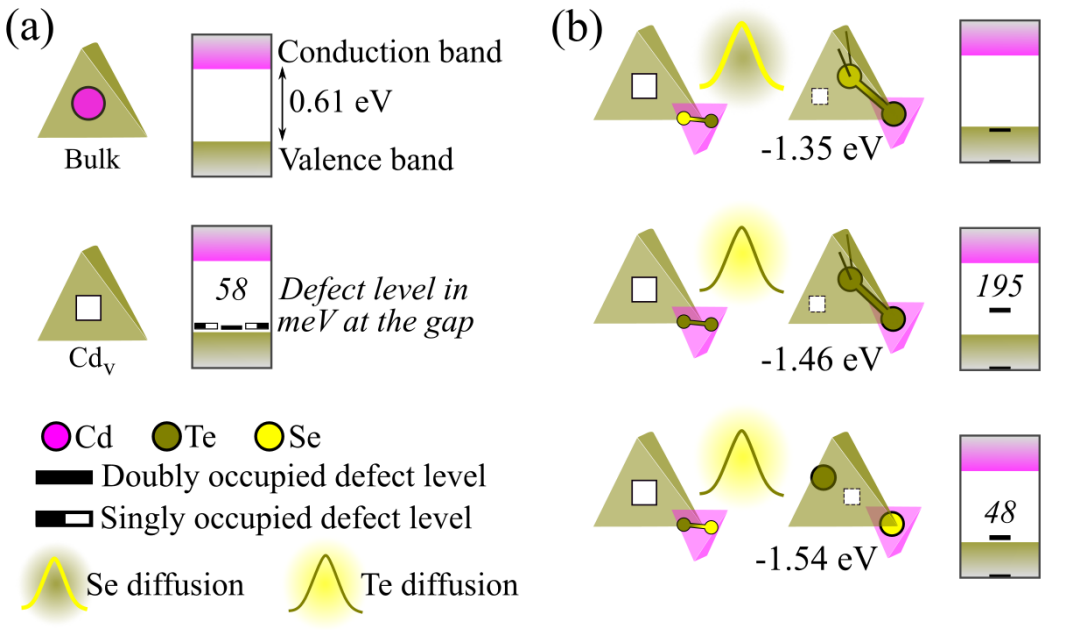

Figure 4.18: Simplified electronic structure of (a) CdTe bulk, V_{Cd} and (b) defect states of three antisite configurations resulting from the chalcogenide diffusing interstitial with V_{Cd}. The respective energy difference (in meVs) of defect states with respect to the valence band edge is written in the band-gap region.

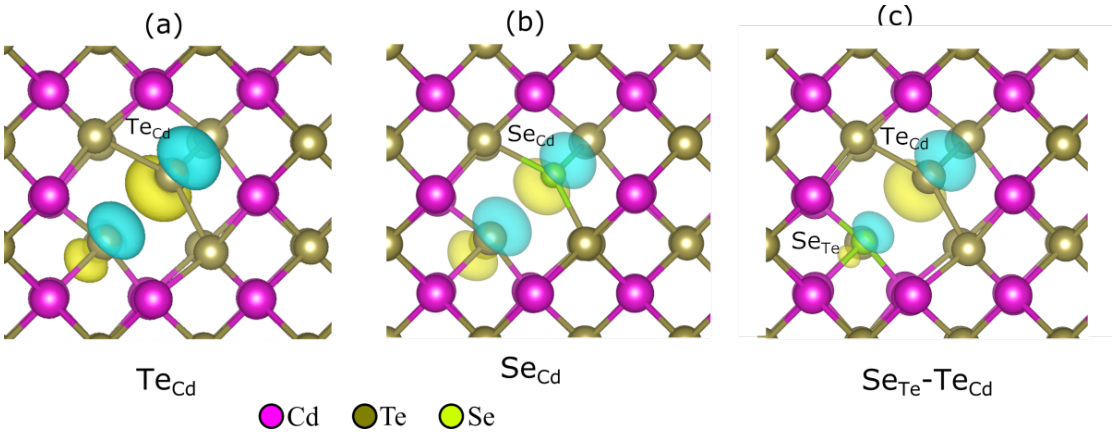

Figure 4.19: Kohn-Sham isosurfaces corresponding to (a) Te_{Cd}, (b) Se_{Cd}, and (c) Se_{Te}–Te_{Cd} antisite defects with electron density value of 0.005 e/Å^3.

It should be noted here that all three defects can be present in substantial concentration based on growth temperature keeping in mind their relatively close formation energy. With respect to the choice of our chemical potentials, the formation energies

of these anti-sites are negative, so that all of them are thermodynamically stable defect complexes over the Cd-vacancy constitutional defect. Although the formation energy is negative for the three antisite defect complexes, they are still characterized by one dangling bond and an anti-bonding defect state. It is, therefore, possible that these defect complexes can interact chemically with another diffusing chalcogenide defect to form more stable defect complexes. Indeed, the displacement of the chalcogenide anti-site atom along the $< 111 >$ direction inside the vacancy leaves a dangling bond that could be passivated by a second chalcogenide approaching the vacancy site.

Therefore we considered further the interaction of these three chalcogenide antisite defect configurations with another diffusing chalcogenide interstitial. These interactions result in to several configurations depending on the exact nature of the diffusing chalcogenide involved in the two consecutive passivation steps. We identified six of these interactions as distinct and characterized by a unique chemical environment on Cd-site and the neighboring chalcogenide tetrahedron (Figure 4.20). The six unique configurations are identified as each leading to the passivation of the one remaining dangling bond and represented by a chalcogenide dimer formation at the Cd-site. As all these configurations have two chalcogenides passivating the dangling bonds at the Cd-vacancy site. Therefore, we have referred to them as bi-passivated configurations.

The chalcogenide dimer present at the Cd-site in a split interstitial manner is aligned along the $< 001 >$ direction in bi-passivated configurations. These bi-passivated configurations have further lower formation energy in the magnitude of more than 1 eV in comparison to three antisite defect complexes, resulting from stable coordination. The most stable of the six configurations is the one where a $< 001 >$ Te dimer occupies a Cd site with two selenium atoms present in the first neighbors' shell (bottom right configuration Figure 4.20). This configuration is reminiscent of the proposed defect complex formed by Te interstitial and Te-antisite interaction (top left Figure 4.20) by Lordi *et. al.* [106]. The coordination of a Se atom with each Te atom of the split interstitial at the Cd-site results in further lowering of the energy by 0.35 eV. This factor is reflected in $Se_{Cd} - Te_{Cd}$ antisite defect complex and in several bi-passivated configurations, where Se_{Te} reduces the formation energy when introduced at Te-site (Figure 4.17 and Figure 4.20).

The bi-passivated configurations with a chalcogenide dimer present at Cd-site involve strong bonding interaction between the two chalcogenide atoms inside the vacancy and the absence of any dangling bond for the six configurations. The defect states for all the cases are majorly present in the valence band, and a few defect states are present within an energy gap of 40 meV above the valence band. (In total, bi-passivated configurations have nine doubly occupied defect states and one empty defect

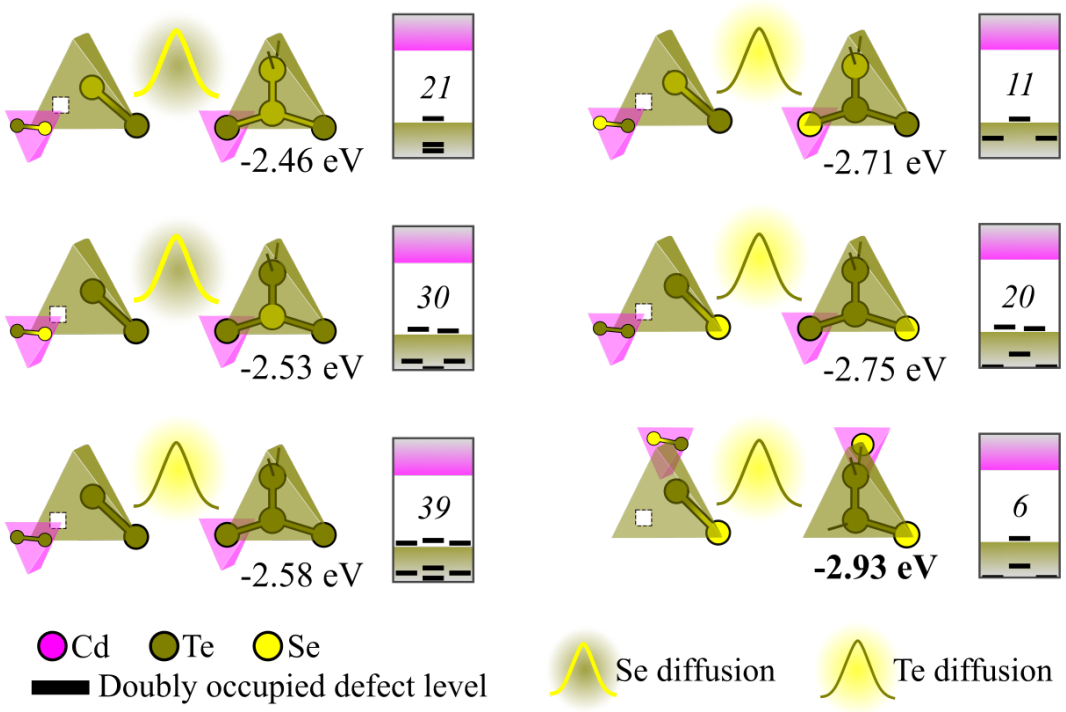

Figure 4.20: Six bi-passivated configurations resulting from the interaction of antisite defects with a diffusing chalcogenide interstitial defect. The split interstitial configuration involved in the reaction is shown in small pink tetrahedrons. Relative energy (in eVs) of these bi-passivated configurations in comparison to constitutional V_{Cd} defect are written at the bottom of each configuration. The position of defect states corresponding to each configuration present close to the valence band-edge is shown on its right with the energy (in meVs) of the top-most filled state with respect to the valence band edge written in the band gap.

state.) Although the energy of Kohn-Sham defect states calculated based on LDA functional is not very precise, they can be used for qualitative analysis[125]. For the defects considered in this study, the position of defect states with respect to band edges for the respective ground state structure has been predicted quite well as in comparison to the reported cases of V_{Cd}, Te_{Cd}, $Se_{Te} - Te_{Cd}$ defect complex, with more accurate hybrid functional and GW calculations[89,99,103,106]. Therefore, we can say with sufficient confidence that the defect states corresponding to all bi-passivated defect configurations provide shallow defect states which lie within the few tens of meVs (40 meVs in our case) close to the valence band edge. The bi-passivated configurations are characterized by an empty anti-bonding state corresponding to the chalcogenide dimer being present

in the conduction band. The chalcogenide dimer anti-bonding defect state for all six configurations lies deep in the conduction band (therefore not shown in Figure 4.20). Therefore, all the bi-passivated configurations can act as both electron donors and acceptors. Although, the position of the defect states (empty states lying too far from the valence band and filled state too far from the conduction band) suggest that both electron and hole capture rates leading to non-radiative recombination are not possible. In other words, all these bi-passivated configurations rectify the defect states of both Cd vacancy and Te antisite defects that otherwise are detrimental to solar applications.

4.6 Conclusion

In this chapter, we have extensively defined at the atomistic level how Se plays a hybrid role in the efficiency improvement of Se alloyed CdTe. We have first studied the electronic structure of critical intrinsic defects Cd-vacancy and Te-antisite, which act as non-radiative recombination centers and limit the efficiency of CdTe-based photovoltaics. We explained how the strain field generated by local re-configuration of the lattice around the defect site can be strongly dependent on the choice of DFT exchange-correlation functional, and a careful analysis of strain field dependence on the supercell size should be made.

To understand the long-range diffusion of Te self-interstitial and Se-interstitial in the CdTe grain, we then identified their diffusion pathways. A combination of translation and rotation of split-interstitial defects was defined to explain the diffusion of both the chalcogenides. We finally demonstrated that the Cd-vacancy and Te-antisite intrinsic defects can be passivated by diffusing Se in the CdTe grain. The interaction of diffusing Se interstitial with the two critical defects in CdTe obliterates their dangling bonds. We identified the low formation energies defect complexes resulting from such interaction of two (one) Se interstitial defects with Cd-vacancy (Te-antisite) defects. The activation energy corresponding to the formation of these defect complexes is lower than -1.2 eV. The lowest formation energy defect calculated by us in the Te-rich conditions with the presence of selenium impurities consists of a $< 001 >$ Te-dimer on a Cd site with two Se atoms in the first neighbor shell. The five other combinations with similar topology also present the same kind of passivating effect in terms of defect electronic levels position with respect to band-edges. Qualitatively speaking, we predict that all these configurations to have low electron and hole capture rates. Due to the diffusion-driven passivation mechanism, we expect that all six configurations with chalcogenide dimer at Cd-site can co-exist.

4.6 Conclusion

In summary, the role of Se in the context of defect passivation of critical defects in the CdTe grain is a hybrid one. Firstly, Se moderates the fast and linear diffusion of Te, thus enabling both chalcogenide atoms to diffuse isotropically inside the volume of CdTe grain and reach Cd-vacancies and Te anti-sites. Secondly, the peculiar diffusion mechanism promotes a Se alloying at the Te-substitution site in the first shell of the Cd-site related defects (Cd-vacancy, Te-antisite, chalcogenide dimer). This lead to a systematic reduction in the carrier capture rates as the defect states are pushed close to band edges or into semiconductor electronic bands. We think that this comprehensive insight on the role of Se in the passivation mechanism of CdTe absorbers should allow further improvements in understanding of defects physics of CdTe-based photovoltaics alongside with other doping strategies[126,127] to push efficiencies in the range of 25 % in the coming years[128].

CHAPTER 5

Transition metal single dopant defect in CdTe for solotronics application

5.1 Introduction

Transition metals (TM) with $3d$-valence electrons are commonly found impurities in semiconductors[129–135]. The growth of new materials where TM doping alters the physical properties of the material, such as its electric[136,137], optical[138–141], and magnetic properties[142–144], is gaining attention. Precise control over these impurities provides a platform for defect engineering of optoelectronic behavior of materials and various other applications based on spin associated with the physics of $3d$-electrons.

TM doping of semiconductor in both bulk and nanostructures forms have found application in different fields ranging from photovoltaics to nuclear radiation sensors[145–149]. In the context of this thesis, Copper (Cu) doping of p-type Cadmium telluride (CdTe) layer for improving the hole concentration of the CdTe absorber is an example of TM doping of semiconductors for photovoltaics application[150–153]. Manganese(Mn) doped CdTe is a promising material emerging as a successor of $Cd_xZn_{1-x}Te$ (widely used commercially) for room temperature gamma-ray detection[149,154–156]. Mn-doped CdTe shows improved homogeneity and the ability to produce large monocrystal detectors over $Cd_xZn_{1-x}Te$[157–159]. Among the other applications based on optoelectronic control, II-VI crystals doped with TM, such as Mn and Chromium (Cr), have been gaining attention for potential application in infrared solid-state lasers[160–165].

For the application based on the spin of 3d-electrons, spin associated with TM ion can be detected and manipulated by opto-electronic means[166–169], providing the platform for various spin-based future solid state device technologies[170–175]. Among such possibilities, diluted magnetic semiconductors(DMSs) have been extensively explored over the last two decades for spintronic and spin-photonic applications[144,176–178]. The spin of unpaired electrons localized on the TM ion impurity interact with the delocalized spin of band carriers (free and photo-generated) with coupling strength related to the spatial overlap of spin wavefunction leading to $s, p-d$ exchange interaction. Such exchange interaction is responsible for the emergence of magneto-optical properties in TM-doped semiconductors with effects such as carrier-mediated ferromagnetism[179–181], giant band-edge Zeeman splitting and Faraday rotation[182,183] in DMSs.

With the progress in doping strategies reaching ultra-high precision levels, the avenue to control the various opto-electronic and magneto-optical properties at a single impurity level is plausible. A lateral accuracy of 35 nm for adjacent intentional single impurities has been observed by Pacheco *et. al.* in Silicon-based devices[184].

Typically at very low concentrations where impurity TM atoms do not interact with one another, they are similar to trapped or embedded atoms. The trapped TM dopants originate individual electronic states well separated from the host band states with an orbital and spin degree of freedom, that can be controlled by means of electromagnetic fields. One of the ways to achieve isolated impurity is to trap one single atom in the semiconductor nanostructures, such as a quantum dot (QD) or quantum wells, through control of growth kinetics. Over the past decade, several advancements have been made in the fabrication process of the epitaxially grown and colloidal doped QDs[9,185,186]. The sensitivity of the trapped impurity localized spin (isolated with the background) to the local fields such as electronic, magnetic, thermal, and strain provide several functionalities[187–191]. Access to the d-orbital manifolds provides an additional degree of freedom for coherent spin manipulation. One opportunity is to coherently control the spin embedded in semiconductor nanostructures, relying on electromagnetic fields to drive transition between spin multiplet states[192,193]. Such impurities hosted in semiconductor nanostructures present long coherence times even at room temperature in some cases[194,195].

The main application of the single dopant impurity atoms in semiconductor nanostructures with opto-electronic control is in the emergent field of Solotronics (a term coined for electronics based on the spin of solitary dopant) with the potential to be used for quantum information processing[7,9,196]. Such intentional doping into a semiconductor nanostructure or binary semiconductor QDs could provide tunable materials with emergent electronic, optical, and magnetic properties due to the formation of (isolated)

sub band-gap states in electronic band-structure. Among the non-magnetic dopants, an impurity nitrogen atom placed adjacent to a vacancy in diamond (popularly referred to as N-V center), and phosphorus doped in Silicon, with localized spin, are the most widely studied defect systems for potential Solotronic application[195,197–200]. For the purpose of Solotronics, magnetic dopants embedded in semiconductor QDs show many promising features such as reproducible quantum signature properties, stability, and scalability for potential application in quantum information processing[196]. TM impurities Manganese (Mn) and Chromium(Cr) embedded in CdTe bulk and QDs as isolated dopants are the subject of discussion for this chapter.

The $3d$-TM magnetic atoms in the semiconductor host provide a large set of options for orbital momentum with electronic and nuclear spin. Electron spin probe and control have already been shown for Mn in II-VI & III-V, Co in II-VI, and Fe in II-VI semiconductors[9,10,12,166,201]. Among the variety of $3d$-TMs, the $4s^0 3d^5$ Mn^{2+} a pure spin system with zero orbital momentum is most widely studied, which have the electronic d-levels lying either in or very close to the valence band in energy. In the case of Mn^{2+} ion in II-VI semiconductors, exchange interaction with the free holes is dominated by $p-d$ hybridization, the so-called kinetic exchange with the anti-ferromagnetic sign[202]. Magnetic dopants with non-zero orbital momentum and zero nuclear spin, are expected to have longer spin relaxation time and large spin-mechanical coupling in comparison to Mn^{2+} (L = 0, S=5/2) solitary dopant and light atom dopants defect such as N-V center[12]. Large coupling between spin and lattice vibrations provides a possibility of coherent mechanical control of spin associated with such an impurity defect. Chromium (Cr) doped in II-VI semiconductor QDs is of particular interest, due to its net S=2 spin, zero nuclear spin (for most of the isotopes), and non-zero orbital momentum L=2. The latter point opens the way for coherent mechanical control of the Cr spin through surface acoustic waves, for example[203]. The zero nuclear spin leads to a simplified spin-level structure.

The solitary dopant properties are strongly influenced by the local environment factors such as strain, electric, magnetic, optical fields, and dopant position within the device[196]. Coherent control of spin embedded in semiconductor nanostructures typically rely on electromagnetic fields to derive transition between spin states. Another possibility based on mechanical control driven by the interaction of spin with lattice vibration is gaining attention[12,204–207]. This provides a platform also for mediating the interaction between the solid-state spin qubits achieved by the strong coupling of the spin to the resonance mode of a mechanical resonator. In such a spin-mechanical resonator, the vibration mode of an oscillator will be coherently coupled to the spin state of a single atom, driving switching between the spin multiplet states[208].

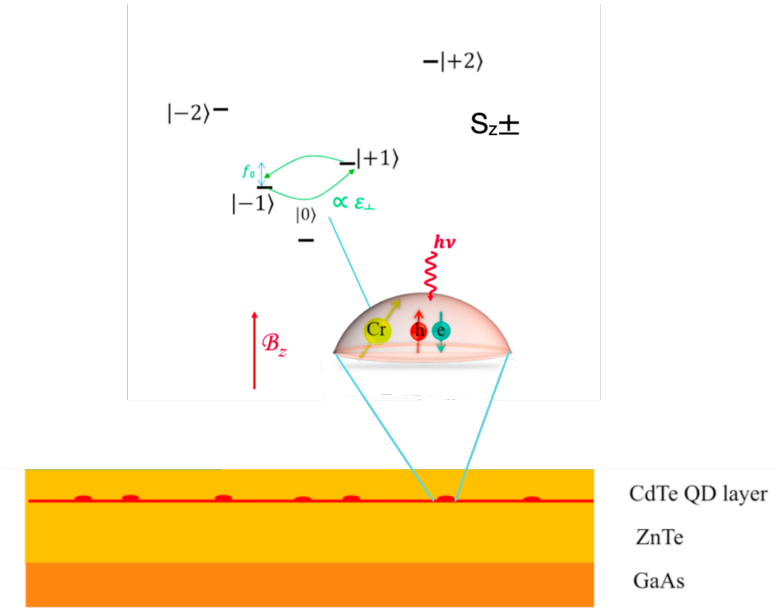

Figure 5.1: Schematic view of the spin multiple structure of a single Cr^{2+} atom doped in CdTe/ZnTe QDs excited with an optical pumping photon[203]

Besombes *et. al.* have shown the probe and optical control of both Mn^{2+} and Cr^{2+} doped in CdTe grown over ZnTe surface by means of optical pumping excitation and photoluminescence readout[201,209,210]. The magneto-optical spectroscopy of Cr doped CdTe/ZnTe QDs shows a large magnetic anisotropy of Cr spin, induced by bi-axial strain in the plane of dots resulting due to lattice constant mismatch of CdTe and ZnTe. This anisotropy leads to zero magnetic field splitting of the 0,±1,±2 spin quantum states (order of meV), and to the difference in their occupancy at low temperatures (5K)[12,210]. The spin transition between these spin quantum states can be derived by optical means.

As part of this thesis, under the ANR Mechaspin project (ANR-17-CE24-0024), we worked in collaboration with Besombes *et. al.* to provide atomistic-level insight into these Soltronics systems to address growth-related challenges and understand the experimentally observed electronic state of Cr single dopants in CdTe QDs. In this chapter, we have discussed our DFT analysis of the systems and addressed two questions that came to light during the experiments performed by our collaborators. The first is that they found out that the number of QDs presenting the correct single dopant configuration for the Cr atom turned out to be much lower in comparison to Mn-doped CdTe/ZnTe QDs grown by the same approach. Two, they reported, for the first time, stabilization of Cr^{+} oxidation state in CdTe/ZnTe QDs, such that Cr captures an electron from background doping.

In this chapter, we first studied, using the Density Functional Theory (DFT), the electronic structure of Cr^{2+} and Mn^{2+} solitary dopant defects in CdTe. We identified the effect of host interaction in terms of Jahn-Teller coupling and local symmetry of the dopant in the lattice. Then in the second part, we did a detailed analysis of the TM dopants interaction with native impurities in CdTe to answer the two questions, one of the concentration of the single Cr doped CdTe/ZnTe QDs and the second of the Cr^{+} oxidation state. We provide plausible explanations for the two phenomena as observed in the experiments.

5.2 Cr and Mn dopant electronic configuration in CdTe: Experimental background

Cr and Mn free ions have electronic configuration of $[Ar]\,3d^5 4s^1$ and $[Ar]\,3d^5 4s^2$ respectively. For Cr ion half-filled d-states are more stable than $[Ar]\,3d^4 4s^2$ configuration. When TM, Cr, and Mn are doped into the CdTe matrix, taking a substitutional position at the Cd site, $4s$ electrons are exhausted in bonding interaction with the neighboring Te atoms. Mn and Cr thus take up an oxidation state of II in terms of coordination, same as that of Cadmium (Cd), and thus introduces no net charge. The electronic configuration for Cr and Mn, therefore, changes to $[Ar]\,3d^4 4s^0$ and $[Ar]\,3d^5 4s^0$ respectively. In the defect notation, Mn and Cr dopant are represented as Cr^0_{Cd} and Mn^0_{Cd}, whereas in TM dopant representation, they are referred with the oxidation state as Cr^{2+} and Mn^{2+} respectively. EPR experiments establish that Cr and Mn impurities inserted in CdTe follow Hund's rule, and the ground state has an electronic spin of S =2 and S= 5/2, respectively[211–214]. According to spectroscopic notation $^{(2S+1)}L$, the ground state of Cr and Mn in CdTe is noted as $^5D(L = 2, S = 2)$ and $^6S\,(L = 0, S = 5/2)$. Mn substitution impurity is characterized by zero orbital angular momentum and no spin-orbit coupling. Cr^{2+} and Mn^{2+} configurations in CdTe DMSs and quantum dots (QDs) have been extensively reported in the experiments with electron paramagnetic resonance (EPR)[212,215–217], infrared absorption[11,218,219], magnetization measurements[201,220,221], and Raman EPR spectroscopy[222].

In the CdTe Zinc-blende structure with T_d symmetry, Cr and Mn dopants experience crystal field splitting. The crystal field affects only the orbital part of the wavefunction and lifts the degeneracy of energy levels of the system. Since the ^6S state of Mn^{2+} ion is symmetrical and non-degenerate, except for spin, the crystal field does not affect the electronic energy level of Mn^{2+} ion, as shown in Figure 5.2. For Cr^{2+} ion, the ground state is orbital degenerate. Thus, the crystal field splits ^5D state into an energy state

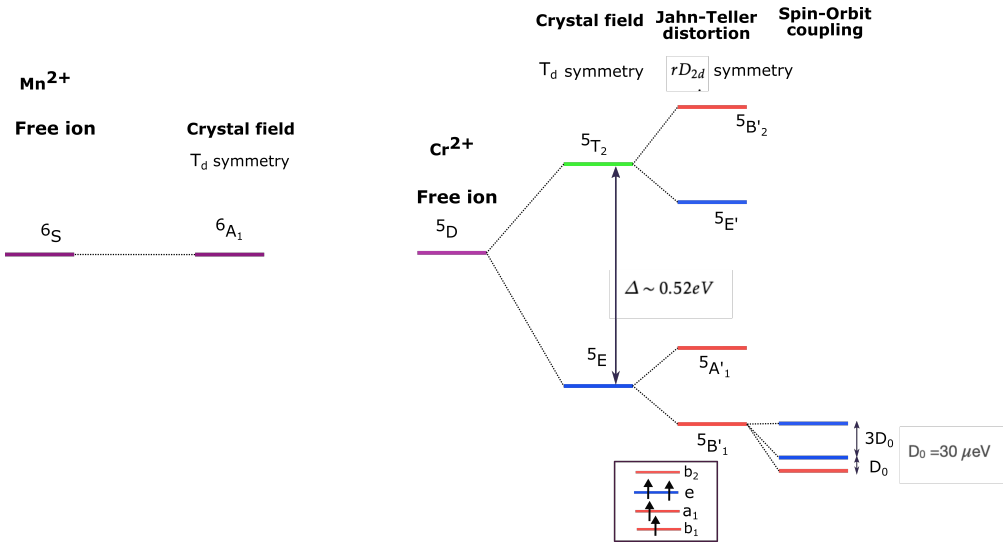

Figure 5.2: Schematics diagram of energy levels of Mn^{2+} and Cr^{2+} single dopants in CdTe bulk. The ground-state $^5B_1'$ is defined by the electronic orbital splitting as shown in inset

triplet $^5T_2$ and doublet ^5E. EPR results from Vallin *et. al.* suggest that the $^5T_2$ is susceptible to Jahn-Teller instability, which further splits into orbital doublet $^5E'$ and singlet $^5B_2'$[212]. Consequently, it was proposed that tetragonal distortion also split term symbol orbital doublet ^5E into $^5B_1'$ and $^5A_1'$. They, by means of applied uni-axial strain along three perpendicular axis of the Cr-doped CdTe crystal, reported that the Jahn-Teller distortion mode is identified as compression along one axis of the tetrahedron formed by four neighboring Te atoms. Therefore the distortion mode was proposed to have 3-fold degeneracy.

Spin orbit coupling further splits the spin levels $^5E'$, $^5B_2'$, $^5B_1'$ and $^5A_1'$ in to spin sub-levels $m_s = \pm 2, \pm 1, 0$. This spin-orbit interaction results in magnetic anisotropy ($D_0 S_z^2$), with zero field splitting(D_0) $\sim$ 30 μ eV. In the case of the Cr doped CdTe/ZnTe QDs, the zero field splitting grows large to a value of $D_0 \simeq 1 \pm 0.6meV$[12]. In the presence of electromagnetic fields, these spin levels could be used to create a two-level system, as in for Cr^{2+} impurity embedded in CdTe/ZnTe for optical excitation b/w +1 and -1 m_s S_z sub-levels with zero-field splitting and readout with the photoluminescence[12,210].

A Mn^{2+} ion in CdTe matrix with L=0 symmetric wavefunction has zero spin-orbit coupling. But in CdTe QDs grown on ZnTe surface with lattice mismatch results in a non-negligible magnetic anisotropy of $\sim$ 40 μ eV. This system was reported to have a spin memory with a magnetic relaxation lifetime of $\sim$ 100 ns[201].

Another configuration of Cr impurity in CdTe with Cr^+ oxidation state was also

reported in several instances with photo illumination of CdTe bulk specimens containing Cr^{2+}, such that Cr^{+} was photo-generated[213,223–225]. Recently, Vivek *et. al.* reported the Cr^{+} stable configuration in a Cr-doped CdTe QDs grown over the ZnTe layer. They argued that a small fraction of single doped Cr^{2+} in CdTe QDs transformed into Cr^{+} acceptors by capturing an additional electron from a 'background' doping source. The ground state of Cr^{+} is ${}^{6}S(L = 0, S = 5/2)$ with six-fold degeneracy having electronic configuration similar to Mn^{2+}. As in the case of Mn^{2+}, a magnetic anisotropy and spin memory lifetime of 20 μs was reported for Cr^{+} [226].

As DFT is an electronic levels-based (ground-state) theory. In subsequent sections, we will discuss only the ground state and the electronic orbitals (as shown in the inset of Figure 5.2) of the impurity Cr and Mn dopants.

5.3 Single transition metal impurity in Zinc-blende structure

5.3.1 Ludwig and Woodbury model

The electronic structure of transition metal (TM) single impurity in zinc-blende semiconductors can be understood in terms of the phenomenological model proposed by Ludwig and Woodbury (LW)[227–229]. They based their model on electronic paramagnetic resonance (EPR) spectrum results and postulated that the TM in the Silicon lattice prefers to take up either a substitutional position or a tetra-coordinated interstitial position. TM impurity, when introduced into the semiconductor matrix, perturbs the local lattice electronic potential. The energy of electronic levels hosting TM impurity *d*-electrons is different than bulk band-states and results in several electronic levels lying deep in the semiconductor band-gap. The model is based on simple symmetry consideration of impurity defect states and the local structure sustained from EPR results. The model can be translated to the case of TM dopants in the II-VI semiconductor matrix[134,228]. We will use here the basic assumption of the LW model, where local symmetry around the defect can be understood in terms of localized *d*-like impurity states and the interaction of electrons hosted in these states.

The 3*d*-TM isolated atoms have valence electronic configuration of the form $4s^m 3d^n$, where m=2 except in the case of Cr and Cu, where it is m=1. When embedded in the Zinc-blende lattice, TM, in the case of the substitutional position, involves in bonding interaction with the neighboring anion (group VI) atoms. The dangling bonds associated with neighboring anion atoms interact with 4*s* shell electrons of TM, such that 2

4s electrons are exhausted in the TM-anion bond resulting in sp^3 type bonding. The empty 4s electronic states are pushed deep into the conduction band. Thus the TM electronic configuration changes to $4s^0 3d^n$, referred to as oxidation. The 3d-electrons of TM impurity are tightly bound to the atomic nucleus, and this is the reason why the 4s electrons are first to be lost upon oxidation.

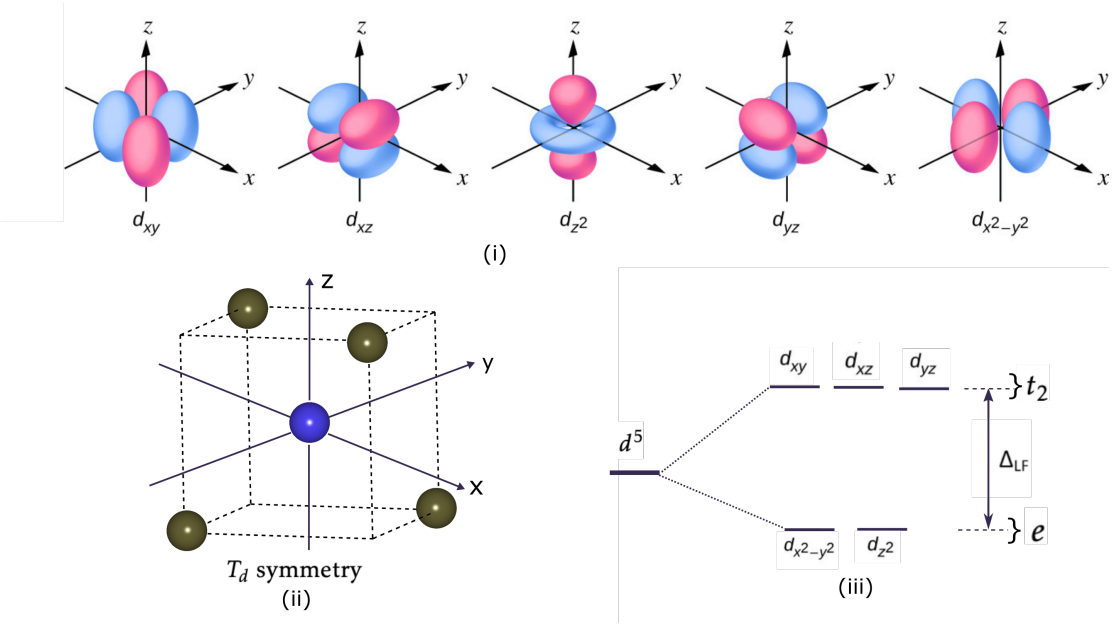

Figure 5.3: (i) d-orbitals of an isolated TM atom. (ii) Schematic view of TM impurity replacing a Cd atom site in CdTe. (iii) d-orbital splitting due to crystal field experienced by TM impurity in zinc-blende lattice

The 3d electrons of the dopant atom are subjected to an electrostatic potential that has a T_d point group symmetry and strength dependent on the electronegativity of the anion atoms. Neglecting the interaction among the 3d electrons of isolated TM impurity atom, under single-particle approximation[230], the 3d orbitals are degenerate in the case of spherical symmetry as shown in the Figure 5.3. Within a simple electrostatic repulsion treatment, TM at the substitutional site is surrounded by four negative ions. Considering the electron density on the neighboring anion atoms is pointed towards the TM along the bond. The electronic repulsion from neighboring anion atoms results in an interaction similar to crystal field splitting, as seen in TM complexes in a T_d symmetry environment. As a result of crystal field splitting, the 3d-orbital states split into two groups; two of the orbitals have electronic lobes directed along the Cartesian axis (denoted as the e orbitals as shown in Figure 5.3), while the other three are between the axes (denoted as the t_2 orbitals). Under T_d symmetry crystal-field the d electronic

orbitals transforming as xy, xz, yz are identified as triply-degenerate t_2 states, whereas orbitals transforming as $x^2 - y^2$ and z^2 are identified as doubly-degenerate e states. The three orbital xz, xz, and yz lie along the TM-anion bond and interact strongly with the p-electrons of the neighboring anion atoms. The nature of the interaction is anti-bonding thus, these states are raised in energy relative to the doublet.

The partial occupation of these d-electronic orbitals brings about the so-called Jahn-Teller distortion in the case of TM complexes as well as in the isolated TM impurity in the semiconductor host[47,231,232]. The d-electrons localized on TM impurity ions in II-VI semiconductors prefers to be unpaired and the impurity has a high spin value[130]. This arises as a result of the repulsive coulomb electron-electron interaction between $3d$-electrons being dominant over the crystal field splitting. The absolute magnitude of crystal field splitting is assumed to be small so that the electrostatic Coulomb repulsion is larger than the d-splitting energy so that electrons remain unpaired. Following the same, a one-to-one correspondence between the phenomenological model presented here and results from *ab-initio* calculations can be made by comparing the Kohn-Sham eigen states symmetry, defect electronic structure, and local symmetry around the TM impurity in semiconductors[233].

5.3.2 TM $3d$-orbital overlapping with neighboring anion p-states

We discuss in this section, the electronic structure of embedded $3d$-TM in the context of II-VI semiconductor, explained in terms of defect-induced states as in Picoli *et. al*[234]. TM in semiconductor lattice can be assumed to take up a cation vacancy site and form a bond with anion neighbors. The electronic structure of point defect or impurity in T_d coordinated systems can be understood in terms of sp^3 orbitals and the corresponding single-particle energy levels. An unrelaxed cation vacancy, in T_d symmetry environment with sp^3 character dangling bonds, results in to s-like singlet a_1 and p-like triply degenerate t_2 localized states[48,107,108] as shown in the right end side of Figure 5.4.

TM atomic-like d-states overlaps and interact with vacancy defect states localized on to the neighboring anion atoms leading to the formation of bonding and anti-bonding states[234,235]. As shown in Figure 5.4, TM impurity triplet d-like t_2 state interacts with p-like t_2 state of cation vacancy, which transforms with the same symmetry adapted representation, and results in to bonding $t_2^{b\pm}$ and anti-bonding $t_2^{anti\pm}$ states (where plus and minus indicate the spin orientation). Vacancy a_1 like state interacts with the $4s$ state of TM and forms a bonding state deep in the valence band and an anti-bonding state resonant in the conduction band (not shown in the diagram). The doubly degenerate e (d)-states of TM have no vacancy state to interact with and are essentially non-bonding

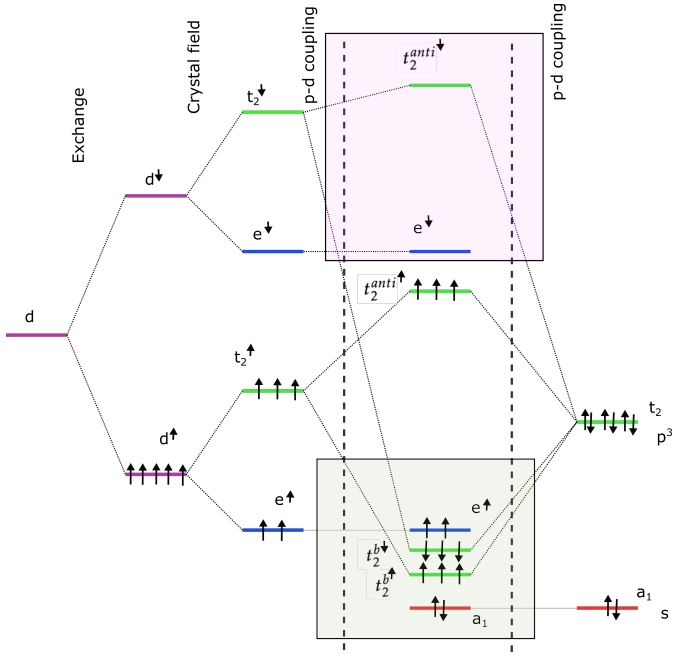

Figure 5.4: Schematics diagram of TM impurity defect states resulting from the interaction of atomic like d-states of impurity and the sp^3 like state of neighboring anions.

in character.

TM electrons in the d states, experience large exchange interaction among themselves, and therefore spin-up and spin-down electronic states are split into energy by order of a few electron volts. As a result e state as well as t_2^b and t_2^{anti} states split in to $e^{\pm}$, $t_2^{b\pm}$ and $t_2^{anti\pm}$ states. These electronic levels are gradually occupied with the TM impurity valence electrons and six electrons shared by the neighboring Te atoms. The $t_2^{b\pm}$ and e^{+} levels are fully occupied and lie in the valence band. These are followed by spin-up t_2^{anti+} and spin-down e^{-} and t_2^{-} levels lying at higher energy values in that order. With all the spin-down t_2^{anti-} and e^{-} state being empty for Cr and Mn impurity embedded in II-VI semiconductors.

5.3.3 Jahn-Teller distortion

Jahn-Teller effect[47,232], which brings out symmetry breaking of orbitally degenerate states in non-linear systems, is commonly seen in molecules and in point defects/impurities in the semiconductor lattice. The basic principle statement is that any non-linear atomic arrangement in a molecule (point defect) is unstable up on the degeneracy of molecular orbitals (defect molecule orbitals) at static equilibrium[47]. As a result, deep localized

defect states induced by TM impurity in the band gap might trigger local reconfiguration in the lattice around the defect/impurity site. For the partially occupied states such as triply degenerate $t_2^{anti\pm}$ states of d orbital character, the total energy is lowered by some local atomic distortion along with symmetry breaking of degenerate states. The distortion modes usually occur along a high-symmetry axis of the local atomic configuration defined by nearest neighbors (characterized by localized deep defect state(s) electronic wavefunction). The magnitude of distortion varies linearly as the splitting of degenerate states, and the energy lowering contribution of distortion is quadratic[236]. It is worth mentioning that distortion is derived only in the case of deep localized impurity states and not for the impurity states resonant with the host electronic bands. In the Zinc-blende structure, TMs (Cr and Mn) are present in the T_d symmetry of neighboring anion atoms. The symmetry adapted distortion as discussed by Saboya *et. al* derived by degeneracy breaking of T_d symmetry adapted orbitals can be defined primarily as tetragonal (D_{2d} and C_{2v} symmetry group) and trigonal (C_{3v}, which can further reduce to lower symmetry such as C_s in some cases) Jahn-Teller distortion[237]. Only tetragonal distortion modes for isolated dopants are discussed here as they are the only ones relevant in this case. We have not discussed here trigonal Jahn-Teller distortion mode.

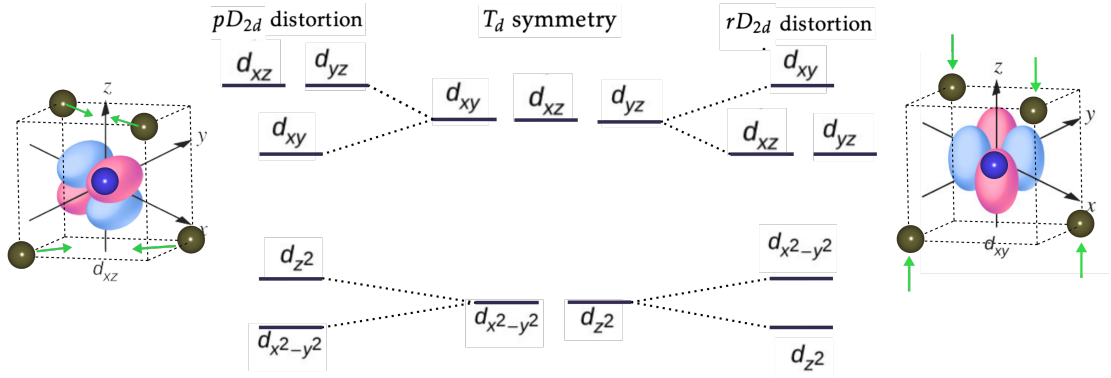

Figure 5.5: Schematics diagram of tetragonal distortion D_{2d} from T_d symmetry in zinc-blende lattice. The *resonant* rD_{2d} distortion mode is driven by energy up-lifting of $t_2^{anti\uparrow}$ states of d_{xz} and d_{yz} orbitals character and the *paired* pD_{2d} mode is driven by energy up-lifting of state driven by d_{xy} orbital. The energy uplifting in both modes results from increased coulomb repulsion in the electron-density distribution corresponding to the orbital.

We have defined distortion modes considering the point defect model[48,230], which assumes that the local lattice rearrangement around the defect can be modeled in terms of the relative position of the four nearest neighboring atoms of impurity in a diamond-like lattice. We define the position of the nearest neighbor as r_i^0, where i indices repre-

sent atoms as 1, 2, 3, and 4 in an ideal lattice. The rearrangement of atoms, r_i in terms of displacement δ can be defined as

$$\delta(r_i) = (\delta x_i, \delta y_i, \delta z_i)$$

The displacement can be broken down into two components; the first one is the symmetric breathing mode of neighboring atoms that can be defined as $\delta(r_i^B) = \delta x_i = \delta y_i = \delta z_i)$ for all i. The second component is defined as symmetry adapted Jahn-Teller distortion/displacement of neighboring atoms as $\delta(r_i^{JT}) = \delta(r_i) - \delta(r_i^B)$.

Here tetragonal symmetry distortion can be derived by two displacement modes brought by symmetry breaking of degenerate d-orbital derived $t_2^{anti\pm}$ states: *(i)* $|\delta x_i| = |\delta y_i| < |\delta z_i|$ referred as *resonant* rD_{2d}, *(ii)* $|\delta x_i| = |\delta y_i| > |\delta z_i|$ the *paired* pD_{2d} symmetry modes. The rD_{2d} distortion mode is driven by the compression of the anion tetrahedron along one of three cartesian axes, as shown in Figure 5.5. In this Figure 5.5, compression mode is shown along the $z-$ axis. This is brought by energy lowering of $d-$ orbitals having components along the z-axis, *i.e.*, d_z^2, d_{xz}, and d_{yz}. Whereas, pD_{2d} distortion is driven by compression along a plane of the (110) family. In the Figure 5.5, pD_{2d} compression mode is shown in the $x - y$ plane. This results from the lowering of energy of d_{xy} and $d_{x^2-y^2}$ orbitals. The distance between nearest neighbor r_{ij} as defined in case of *paired* pD_{2d}, out of 6, two are paired and shorter than the other 4, whereas in case of *resonant* rD_{2d} 4 resonant r_{ij} are shorter than other 2. Consequently, tetragonal distortion modes are 3-fold degenerate for 3 cartesian axes.

5.4 DFT results of the ground state of Cr and Mn single dopant in CdTe bulk

Physical parameters, *i.e.* the lattice constant (a_0) = 6.42 Å and bulk modulus (B_p) = 45.03 GPa, as obtained by us in DFT calculations for pristine CdTe Zinc-blende structure in equilibrium condition agrees closely with (a deviation of 1 % and 1.2 %) the experimentally reported values of a_0 = 6.48 Å and B_p = 44.50, respectively[96]. The CdTe band-gap in our LDA calculations is underestimated as 0.61 eV instead of the experimental reported band-gap value of 1.48 eV[96]. The band-gap underestimation is a well-documented fundamental issue associated with the use of local and semi-local exchange-correlation functionals in DFT[31]. Despite the quantitative error in band-gap, DFT calculations with spin-resolved local density approximation (LSDA) functional can provide a good qualitative description of the defect states appearing due to the TM impurity in the semiconductor matrix that agrees and can be understood in conjunction

with the experimental results[238]. The correct charge and oxidation state of TM ion and the character of TM interaction with the other defects can be accounted for qualitatively.

The defect-induced states by localized *d*-orbitals of TM ion are supposed to be further split by the spin-orbit coupling interactions. The spin-orbit interaction is not taken into account here in the calculations and discussion as compared to the magnitude of crystal field splitting of 0.52 eV (from the experiment)[212], spin-orbit coupling induced zero-field splitting is +30 μeV[12] and thus relatively very small.

5.4.1 Oxidation and spin state of Cr and Mn in CdTe

We studied the TM substitution doping configuration with Cr and Mn replacing the cation Cd(II) site in a $2 \times 2 \times 2$ zinc-blende supercell of CdTe with 64 atomic sites. We did these initial calculations in a 64-atom supercell, as in case of CdTe, Cd *d*-electrons have to be treated as valence electrons, this significantly increases the computation cost in comparison to calculations of other zinc-blende structure semiconductors, such as Si and GaAs. Firstly, in the neutral supercell, we identified an oxidation state +2 for Cr and Mn, the same as that of the cation (Cd) oxidation state. The $4s$ atomic states of Cr and Mn impurity are involved in bonding interaction with Te-dangling bonds resulting from the Cd vacancy, which is filled by the TM substitution atom. The corresponding bonding states move deep in the host band occupied states (valence band). This is reflected in the *d*-orbital occupation of both TM dopants, where the *d*-electrons are localized on the TM center and show the signature of non-zero net electronic spin.

The Cr^{2+} and Mn^{2+} TM dopants in the neutral charge (q=0) state, assumes the electronic configuration $3d^4 4s^0$ and $3d^5 4s^0$ characterised by the 4 and 5 electrons occupied in the *d*-levels respectively. In the next step, for the case of the Cr impurity atom, we calculated the occupation manner of the TM *d*-orbitals driven states (with orbital overlapping from neighboring Te atoms), that split as a result of the CdTe crystal field. We considered two possibilities for the electron population in the d-orbitals: first, the one where Hund's rule is followed, that support unpaired electrons, and the other with spin-paring.

We calculated the stability of different net spin values of S = 2, 1, and 0 corresponding to $d^{4\uparrow}d^{0\downarrow}$, $d^{3\uparrow}d^{1\downarrow}$, $d^{2\uparrow}d^{2\downarrow}$ respectively. The $d^{4\uparrow}d^{0\downarrow}$ configuration, with net spin S=2 was stabilized over S=1, S=0 by energy of 0.85 and 5.32 eV respectively. These value point to a strong tendency of *d* electrons in this system to remain unpaired. Initial structure with unperturbed T_d symmetry was considered for these calculations, as the substitutional site presents T_d symmetry in the zinc-blende structure. To calculate the total energy of the meta-stable spin states with the different spin configurations (other

than ground state S=2), we made constrained DFT calculations with magnetic moment fixed to a specific value of interest. All three spin configurations were subjected to geometry relaxation.

Consistent with experimental reported EPR results[212] and phenomenological model as discussed in sub-section 5.3.1, electrons prefer to be unpaired and follow Hund's rule. In the subsequent discussion, we thus have considered the unpaired electron configuration with the net electronic spin S=5/2 as the ground spin state for Mn_{Cd} impurity as well. For all the calculated results in the following discussion self-consistent algorithm for geometry optimization based on Pulay's discrete inversion in the iterative subspace (DIIS) technique[46] is used. In these calculations, the net spin value has been kept unconstrained.

5.4.2 Atomic and electronic structure of Cr and Mn single dopants in CdTe

The calculated atomic structure of the two dopants agrees with the point defect model[48,230], which suggests that the lattice perturbations for a dopant are local in character and can be understood in terms of rearrangement of the four nearest atoms forming a tetrahedron. For the optimized geometry corresponding to spin (ground) state S=2 and S=5/2 in T_d symmetry for Cr_{Cd} and Mn_{Cd} respectively, we find the distance of dopant Cr_{Cd} and Mn_{Cd} TM ions with neighboring Te atoms (sitting at the edge of the tetrahedron) (Figure 5.6) to be 2.74 Å and 2.66 Å respectively. In comparison, the Cd-Te bond length in pristine CdTe is 2.78 Å. On geometry optimization, the T_d symmetry is maintained. The displacement coordinates of the four nearest neighbour of Mn_{Cd} is symmetrically inward and are given as $|\delta_x| = |\delta_y| = |\delta_z| = 0.1$ Å . In comparison, the nearest neighbors of Cr_{Cd} dopant do not move significantly.

Compared to the ideal tetrahedral position of the four nearest neighbors in unrelaxed structure (as in pristine CdTe), the four nearest neighbors of Cr and Mn impurity on geometry optimization move closer to TM ion by the amount of $\delta R_i^B = 0.1$ Å and 0.02 Å respectively, as symmetric breathing mode (introduced in sub-section 5.3.3). To understand the effect of supercell size on the ground state configuration, for the case of Mn impurity with T_d symmetry, geometry optimization was performed in 216 atom supercell. The optimized geometry and electronic structure results for the 216 atom supercell calculations were the same as that of 64 atoms supercell. The values reported here are from $3 \times 3 \times 3$ (216 atoms) supercell calculations.

As explained in the sub-section 5.3.2, the *d*-orbitals of the TM undergo three types of interactions *(i)* crystal field splitting resulting in triplet t_2 and doublet e states, *(ii)*

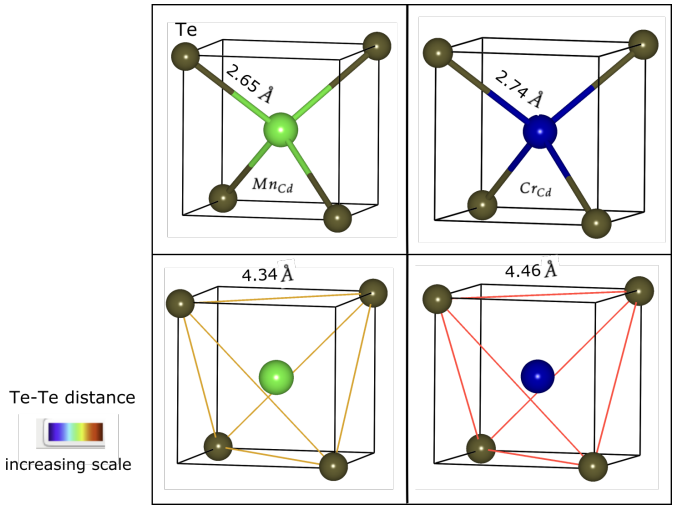

Figure 5.6: Optimized geometry parameters of Mn (green) and Cr (blue) impurity in the immediate local environment formed by four Te neighboring atoms enclosed in the tetrahedron, from 216 atom supercell calculations.

exchange splitting interaction which leads to spin-up and spin-down states *(iii)* orbital overlapping with the neighboring Te-states which splits t_2 states into anti-bonding ($t_2^{anti\pm}$) and bonding ($t_2^{b\pm}$) components. Thus the defect states in the following sections are discussed in these terms.

Both the dopants lead to the appearance of localized defect states of d-orbital character (hybridized with neighboring Te atoms p-orbitals) in the conduction and valence band. As a result of large exchange interaction, spin-up, and spin-down electronic levels split by more than 1.5 eV for both Cr and Mn dopants. With d^4 and d^5 configuration equivalent to $d^{4\uparrow}d^{0\downarrow}$ and $d^{5\uparrow}d^{0\downarrow}$ respectively for Cr and Mn only spin-up states are filled. All the non-bonding and anti-bonding spin-down defect states are located in the conduction band for both the dopant cases.

We obtained TM ion d-states in both spin-up and spin-down channels split into triply degenerate t_2 (t_2^{anti}) and e_2 states corresponding to T_d symmetry. The position for these TM ion localized states is significantly different for both the dopants, pointing to their different electronic activity. The $t_2^{b\pm}$ defect states for both the dopants lie deep in the valence band. The filled (spin-up channel) $e_2^{\uparrow}$ state for both the dopants lies resonant in the valence band. The (spin-up channel) $t_2^{anti\uparrow}$ state for the case of Cr in T_d symmetry lies in the band-gap positioned 0.42 eV above VBM. In the case of Mn impurity, the top of the valence band is formed by the $t_2^{anti\uparrow}$ state with moderate localization (dispersion), shifted from the pristine CdTe valence band lying above at 0.006 eV. The $t_2^{anti\uparrow}$ states position for both the dopants are shown in Figure 5.7. The Kohn-Sham wavefunction

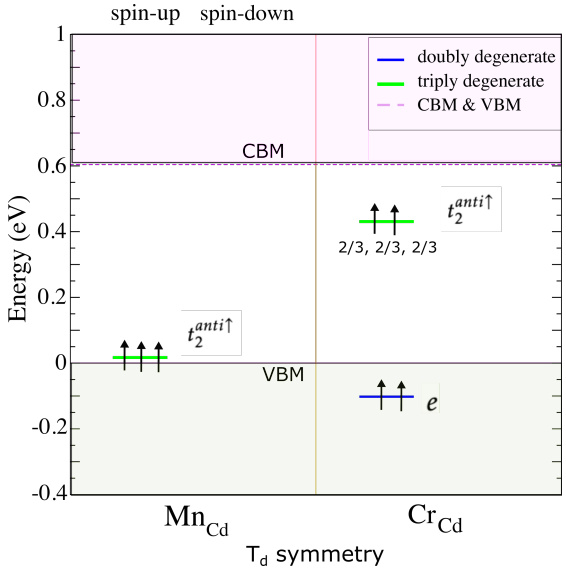

Figure 5.7: Cr and Mn defect states diagram in constrained T_d symmetry configuration; showing states present in band-gap and close to band-edges, valence band minima (VBM), and conduction band minima (VBM).

plots corresponding to Mn dopant $t_2^{anti\uparrow}$ defect states are shown in Figure 5.8.

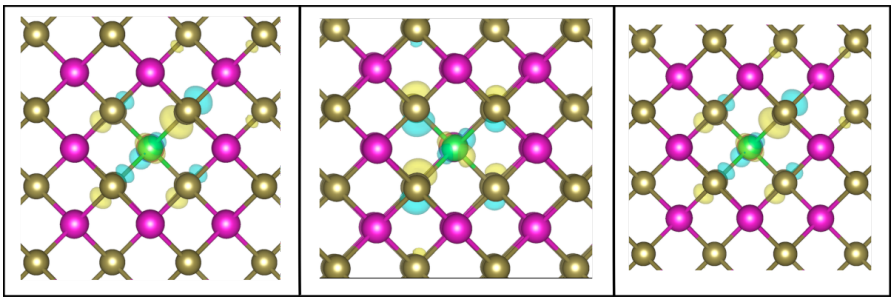

Figure 5.8: Kohn-Sham wavefunction iso-surfaces corresponding to triply degenerate $t_2^{anti\uparrow}$ defect states of Mn impurity with electron-density of 0.002 e/Å^3

The crystal field splitting for the case of Cr impurity that can be calculated from the splitting energy difference between TM impurity triply degenerate $t_2^{anti\uparrow}$ and $e_2^{\uparrow}$ states is 0.54 eV. This value closely matches with the experimentally reported value of 0.52 eV[218]. For the case of Cr impurity with T_d symmetry configuration, triply degenerate $t_2^{anti\uparrow}$ states are present in mid-gap and are partially filled with occupancy of 2/3 electrons for each state (Figure 5.7). The Fermi level is located in the gap for the spin-down channel and cut Cr impurity $t_2^{anti\uparrow}$ defect states in the spin-up channel. The spin-up

defect $t_2^{anti\uparrow}$ states forms dispersion-less highly localized band-pinned at Fermi level. Therefore, the Cr case without symmetry breaking is half-metallic. One thus expects a strong local Jahn-Teller(J-T) instability towards the splitting of the degeneracy in 2(occupied)+1(empty) electronic levels.

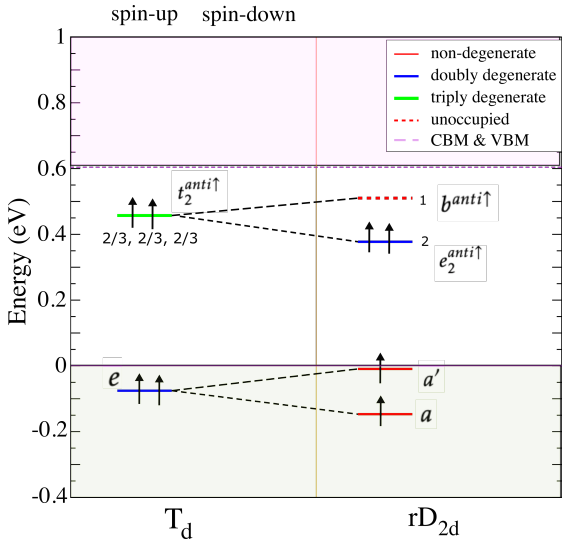

Figure 5.9: Splitting of the Cr impurity $t_2^{anti\uparrow}$ defect states on Jahn-Teller distortion from T_d to rD_{2d} symmetry

Considering the spatial symmetry breaking, J-T distortion is perceived only when ad-hoc symmetry breaking is added to the initial structure. To find the ground state local configuration for Cr doped CdTe consistent with the J-T adapted symmetric distortions, the four nearest neighboring Te atoms were allowed to distort in such a sense considering tetragonal (rD_{2d}, C_{2v}) and trigonal (C_{3v}) symmetry lowering possibilities. In agreement with the EPR[212] and X-ray magnetic circular dichroism (XMCD)[239–241] results for Cr^{2+} in CdTe, we found out that rD_{2d} tetragonal distortion mode is most stable. J-T effect brings about an energy stabilization of 22 meV over the T_d symmetry structure. For the comparison purpose, we considered the symmetry lowering distortion configurations with tetragonal and trigonal distortion in the case of Mn single dopant as well. Tetragonal and trigonal lower symmetry configurations were found to be not stable (or metastable) against T_d symmetry.

The lowest energy rD_{2d} symmetry configuration of Cr_{Cd} dopant was then relaxed in the 216 atom supercell. The local geometry structure for the impurity was found to be the same as that of the 64-atom supercell. Similar observation was made for the Mn_{Cd} impurity ground state structure in 64 and 216-atom supercell calculations. However, in contrast to the Mn_{Cd} case, the electronic structure of Cr_{Cd} was calculated to be different.

In the case of 64 atom supercell, the Cr impurity empty d-oribtal derived defect state ($b^{anti\uparrow}$) in the spin-up channel was calculated to lie above CBM at 0.02 eV, whereas this electronic level lies below CBM at 0.09 eV in the case of 216 atom supercell (Figure 5.9). Therefore, we concluded that 64-atom supercell calculations do not provide an accurate description of localized TM-induced defect states. Thus all the ground state calculations for defects in this chapter are performed in 216 atom supercell.

In the ground state rD_{2d} configuration, four nearest Te atom neighbors of the Cr dopant move in such a sense, that symmetry is lowered from T_d to rD_{2d}, with displacements $|\delta x_i| = |\delta y_i| \neq |\delta z_i|$. Two neighboring atoms (1 and 2) of Te tetrahedron (formed by Cr impurity neighboring atoms) displace inwards along the [001] direction towards the other two Te atoms (3 and 4) of the tetrahedron, which displace inwards along [00$\bar{1}$] direction as shown in the Figure 5.10. The displacements for the four neighboring atoms are $|\delta x_i| = |\delta y_i| = 0.02$ Å and $|\Delta z_i| = 0.18$ Å. In terms of symmetry-adapted coordinates, the magnitude of the breathing displacement is $\delta R_i^B = 0.02$ Å and that of J-T displacement is $\Delta R_i^{JT} = 0.16$ Å. This shows that the distortions are brought only by the J-T effect, and the symmetric breathing effect is negligible. We also realized that the calculated displacements of the second nearest neighbors of impurity atoms for both the dopants are very small (smaller than numerical accuracy values) in comparison to the nearest neighbors, indicating the Jahn-Teller and breathing distortions are local in character in the context of our problem.

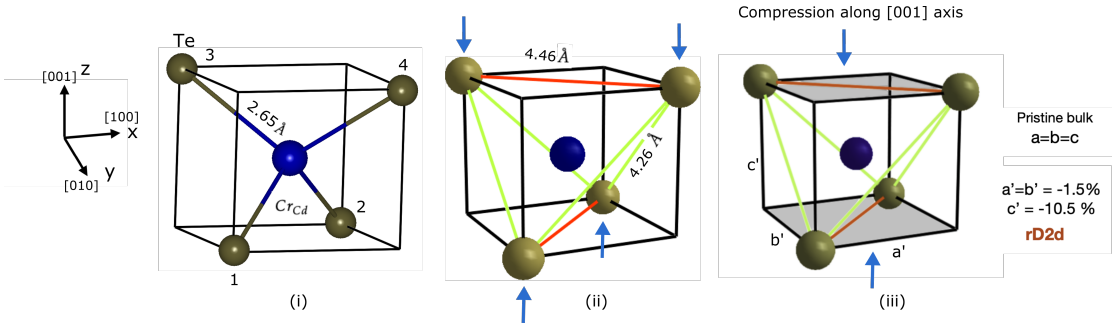

Figure 5.10: (i) Cr-Te bond distance for ground state rD_{2d} symmetry configuration, (ii) neighboring Te-Te atom distances, showing the prominent displacement mode of atoms driving symmetry distortion (iii) the shaded planes along which rD_{2d} compression mode is applicable.

Jahn-Teller distortion is interpreted in terms of splitting of partially occupied $t_2^{anti\uparrow}$ defect states, which split into completely filled doublet $e_2^{anti\uparrow}$ and empty singlet $b^{anti\uparrow}$ state at gamma point as shown in Figure 5.9, positioned at 0.382 eV and 0.521 eV above VBM respectively. As a result of Jahn-Teller distortion, the non-bonding type

doubly-degenerate splits into two singlet states, a and a' lying at 0.006 eV and 0.158 eV below VBM, respectively.

The doublet $e_2^{anti\uparrow}$ and singlet $b^{anti\uparrow}$ defect states results from the pure TM ion d-type d_{xy}, d_{yz}, d_{xz} states hybridised with Te-p states. The non-bonding states a and a' are essentially driven by Cr d_z^2 and $d_{x^2-y^2}$ states. The Kohn-Sham wavefunction plots of the defect states for the Cr dopant are shown in Figure 5.11. From the wavefunction plots of Kohn-Sham eigenstates, we see that d_z^2 and $d_{x^2-y^2}$ states are fully occupied and are located well below the Fermi level while spin-up d_{xy}, d_{yz}, d_{xz} states hybridized with Te-p states of neighboring atoms and are occupied with 2 electrons in the two low lying states and an empty state located around the Fermi level. The hybridization is more pronounced in the case of $e_2^{anti\uparrow}$ and $b^{anti\uparrow}$ defect states in comparison to a and a' electronic states. The top of the valence band is composed of p(Te), and d(Cr) hybridized states. The conduction band-edge is formed by the s(Cd) states and is not perturbed by Cr d-states.

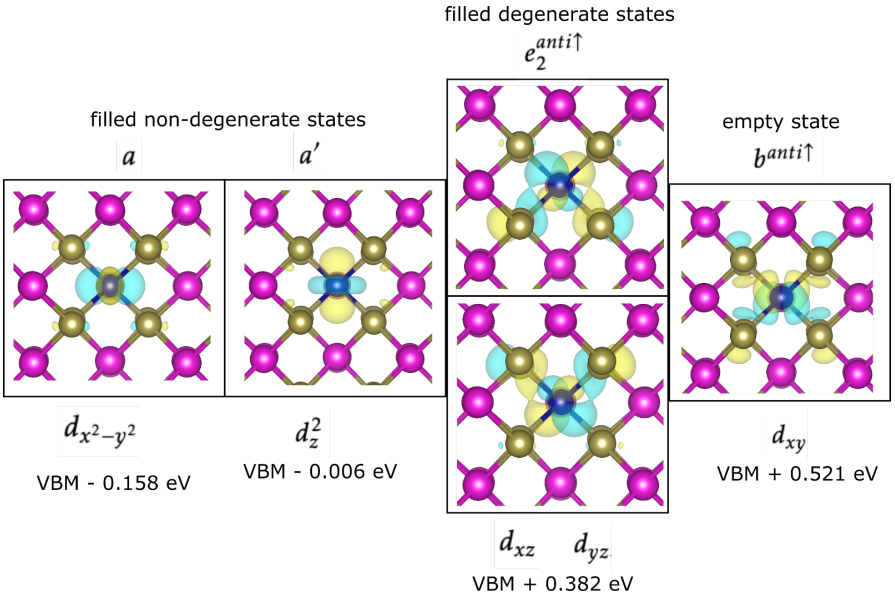

Figure 5.11: Kohn-Sham wavefunction isosurfaces corresponding to Cr impurity defect states driven by d-atomic orbitals with an electron density of 0.0035 e/Å^3 and their respective position in reference to VBM

For the case of Cr impurity, due to the Fermi level lying close to the defect electronic levels, the adding and removing of electrons will happen on the defect. It is worth considering the realistic case of charge compensation, where the hole occupying the defect level in the d^4 configuration can be compensated by an electron added from

the background leading to conversion of d^4 to d^5. Since a d^5 state is a spatial singlet and thus Jahn-Teller distortion will be suppressed. In this case of negatively charged Cr_{Cd} impurity, the addition of one extra electron fills up the Cr 3d shell and induces an outward relaxation restoring tetrahedral coordination. As a result, Cr impurity defect states are lifted in the energy up into the band-gap split by crystal field in e and t_2 components. A detailed comparison of the defect electronic states of Cr neutral and -1 charge state, with the defect complex of Cr and Cd_{Te} native defect, is presented, later in section 5.7.4 and Figure 5.29 and Figure 5.30.

5.5 Dopants, defects interaction and charge state of TM dopant

Semiconductors are affected by native defects and unintentional dopants. Native defects and the growth conditions result in to p-type and n-type material affecting the magnetic properties of the TM doped semiconductors in terms of the charge and spin state of the impurity. The Fermi level of the host semiconductor is affected by the character, concentration of intrinsic defects, and growth criteria. The concentration and TM impurity magnetic state are directly decided by the Fermi level of the host. Especially the magnetic ground state can be manipulated where the Fermi level falls within the impurity levels in the band gap. Consequently, the charge state of a single dopant defect depends on the host semiconductor.

Experimentally in the case of TM-doped zinc-based II-VI diluted magnetic semiconductors, the exchange interaction between the TM ions is reported to be changing from ferromagnetic to anti-ferromagnetic, affected by the local p-type and n-type doping from the intrinsic defects in several cases over the past two decades[242–247]. *Ab-initio* calculations performed along with the experiments explained this change to be brought by the interaction of TM dopant ions with the intrinsic defects (especially with vacancy defects) by means of transfer of electron(s) or hole(s) from the native defects electronic levels to the TM impurity d-type electronic levels[248–251].

In the case of Mn-doped CdTe with typical concentrations of $10^{18} - 10^{20}$ at/cm^3, Solodin *et. al.* proposed that a high concentration of Cd vacancies results from the signature of Mn donor states. They explained the formation of Mn donor states based on charge self-compensation and defect complex formation. By means of high-temperature electrical measurement and quasi-chemical reaction analysis, it was established that Mn interacts with Cd vacancy and forms complexes $(Mn^+_{Cd} - V^-_{Cd})^-$[252].

The dopants can interact with the intrinsic defects and can form bound complexes.

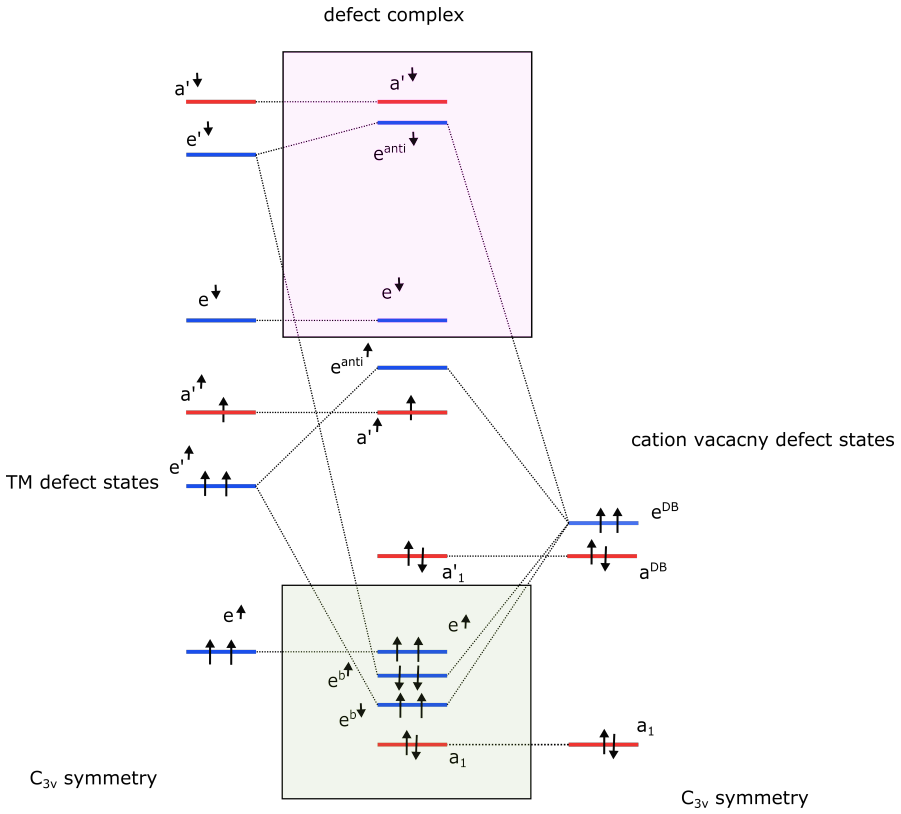

Figure 5.12: Schematic diagram of defect states for TM impurity interaction with cation vacancy in II-VI semiconductors. On the left and right isolated TM impurity defect states and vacancy dangling bond states with C_{3v} symmetry are shown respectively. The middle panel shows the states corresponding to $TM_{Cd} - V_{Cd}$ defect complex (adapted from Rabiger *et. al*[248]).

The electronic defect levels of such defect-bound complexes and clusters are different from the isolated defects. The interaction could lead to alteration in the energies of defect levels and/or the introduction of new defect levels. Such interaction can have an impact on the solubility of dopants, passivation of electrically active defects, change in magnetic interaction among magnetic impurities in dilute magnetic semiconductors, and change in the magnetic state of a single (TM) dopant. As an example, a schematic diagram for the TM interaction with Cd vacancy defect interaction is shown in Figure 5.12 (adapted from Rabiger *et. al*[248]).

Therefore, we studied the interaction of Cr and Mn dopants with the major intrinsic defects in CdTe extensively. We identified that the two issues related to Cr doped CdTe QDs, i.e., the low concentration of single Cr doped QDs and the appearance of negatively charged single Cr in CdTe, can be related to the interaction of Cr impurity with

the intrinsic defects. In the next section, we discuss the electronic structure of the native defects in CdTe and then the interaction of Cr and Mn dopants with native defects in the subsequent sections.

5.6 Native defects in CdTe

Several defects or defect complexes can form during the growth of CdTe. Depending on growth conditions, various native defects could be present, providing different types of doping conditions. Native defects in CdTe have been extensively studied in the past, both experimentally and theoretically identifying the major native point defects in CdTe[72,90,99–101]. First principle calculations in agreement with experimental data can be summarized as follows. The cadmium vacancy (V_{Cd}) is a non-shallow double acceptor. The cadmium antisite (Cd_{Te}), Te-vacancy(V_{Te}) and Cd-interstitial (Cd_i) are shallow double donors. The Te-interstitial (Te_i) and Te-antisite (Te_{Cd}) are deep double donors [72]. CdTe is commonly grown under Te-rich conditions, and Cd vacancy is the dominant intrinsic defect under such growth conditions[89]. Te-antisite and Te-interstitial have relatively low formation energies under Te-rich conditions, consistent with experimental observations.

Defect complex formation of TM impurities with the native defects can be understood in terms of single particle electronic levels (under the assumption of the point defect model). The charge transfer and self-compensation interactions, along with orbital overlap (hybridization) with the native defect electronic levels, drive a thermodynamic association of point defects. We keep our focus mainly on the defect complexes resulting from the interaction of the neutral charge state of TM dopants and intrinsic defects. Therefore single particle electron levels corresponding to only the neutral charge state of intrinsic defects are discussed in this section.

The character of the native defects calculated by us is consistent with experimental results and previous theoretical calculations. There are some divergences from the results of the ground state geometry and the electronic structure of Cd-vacancy reported based on more accurate hybrid HSE06 functional calculations[72,89,103]. The HSE06 calculations for the isolated defects and defect complexes considered here are computationally very expensive and thus were not feasible with HSE06 functional. The description from the LDA calculations provides a good platform for qualitative analysis of the dopants and intrinsic defects character in terms of single particle electronic levels corresponding to defect electrons with plausible physical understanding.

We base our discussion on single particle electronic levels for intrinsic defects in

CdTe based on the suggestion by Su Hai Wei *et. al.*[101]. They suggest that in the case where a high valence atom is replaced by a low valence atom (Cd-antisite Cd_{Te}) and of vacancy defects (V_{Cd} and V_{Te}), due to local electrostatic potential, the defect states result from the host valence band of the sp_3 character and split in to singlet a_{1v} and triplet t_{2v}. These defect states are essentially bonding in character, and their energy with respect to band edges depends on the magnitude of electrostatic potential. These states are occupied by the defect site electrons (0 in case of a vacancy) and the valence electrons of the four neighboring atoms.

Whereas in the case when a low valence atom is replaced by a high valence atom (Te-antisite (Te_{Cd})) or in case of self-interstitials (Cd_i, Te_i), the defect states a_{1v} and t_{2v} lie resonant in the valence band. With them other defect states, singlet a_{1c} and t_{2c} are created from the conduction band. Similarly, the defect states in this case as well are filled by the defect (atom) electrons and the valence electrons of the four neighboring atoms.

We will use this single-particle electron description of the intrinsic defects to explain the electronic structure and ground state symmetry based on the Jahn-Teller distortion and other electronic factors. In cases where native defect electrons partially occupy the triply-degenerated t_2 states, the system may undergo some distortion that splits the degenerated levels. In this case, the system gains electronic energy from the level splitting but pays strain energy. We have presented detailed discussion of electronic structure of CdTe native defects corresponding Te-rich conditions (i.e. V_{Cd}, Te_{Cd}, Te_i). Here a part of those results is discussed again with additions relevant of the discussion for single-particle electron description of the intrinsic defects.

Cd vacancy

Cd vacancy leads to the creation of localized a_{1v} and t_{2v} defect states originating from the valence band. According to the point defect model[101] (3.2.7), neutral charge state Cd-vacancy (V^0_{Cd}) has 6 electrons present in the four Te-dangling bonds equivalent to Te valence (6). These 6 electrons are filled in $a_{1v}(2)$ and $t_{2v}(4)$ defect states, resulting in partial filled triply degenerate t_{2v} states (with 2 holes). Thus, according to the Jahn-Teller theorem, the vacancy local environment can go through distortion to a group symmetry lower than T_d, leading to symmetry breaking locally on the vacancy site.

Although, in our LSDA calculations, we realized that the T_d symmetry is stabilized over Jahn-Teller tetragonal distortion mode D_{2d} and C_{2v} by 2.24 eV and 0.48 eV due to the presence of two localized hole polarons on V_{Cd} site. Therefore the V^0_{Cd} has spin S=1 corresponding to two unpaired localized electrons and is acceptor by character due to two localized hole polarons. The energy eigenvalues of Kohn-Sham states

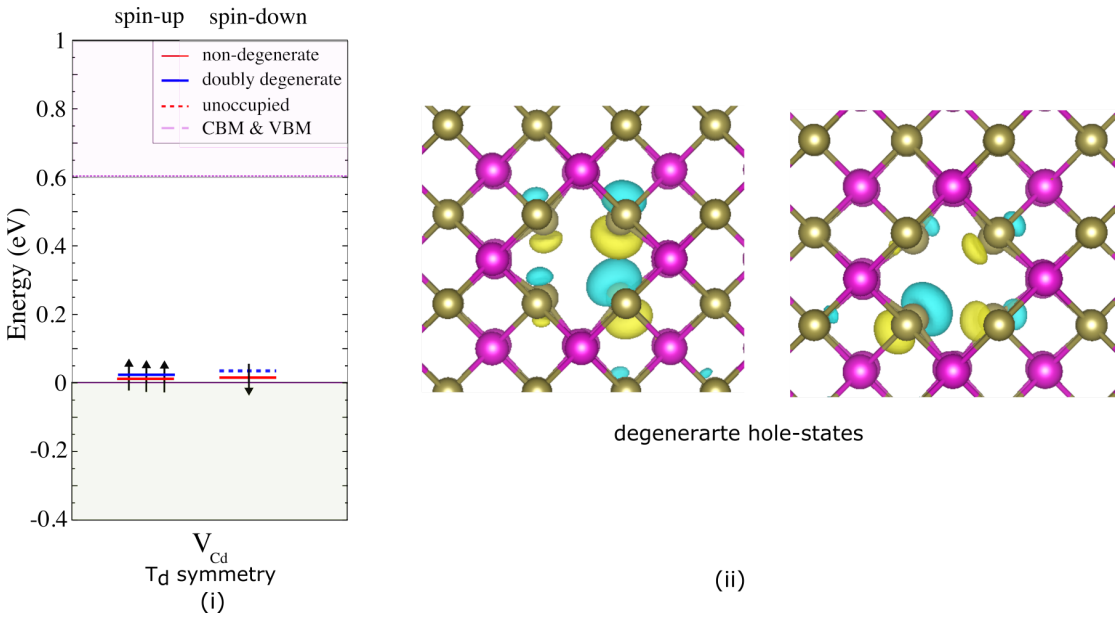

Figure 5.13: (i) Defect state diagram of Cd vacancy, (ii) Kohn-Sham wavefunction isosurfaces corresponding to two localized hole-polarons degenerate states present in the spin-down channel with hole density 0.0025 e/Å^3

corresponding to t_{2v} localized states are shown in Figure 5.13 (i). The corresponding wavefunction for 2-hole polaron is shown in Figure 5.13 (ii). The T_d symmetry configuration is characterized by an inward relaxation of Te neighboring atoms of 0.33 Å towards the vacancy site.

Te vacancy

Removing one Te atom from its lattice site leads to the formation of four Cd dangling bonds, each of which hosts a charge equivalent to half an electron. Te vacancy (V_{Te}) induces a_{1v} and t_{2v} defect states, hosting 2 electrons from neighboring Cd atoms dangling bonds corresponding to the Cd oxidation state (2). Two electrons occupy the localized a_{1v} defect state located at 0.32 eV below the VBM.

The ground state configuration presents a C_{3v} symmetry. This symmetry lowering from T_d to C_{3v} is not driven by Jahn-Teller distortion, as there are no partially filled degenerate states present in the T_d configuration. This distortion is driven by the fact that V^0_{Te} does not follow the Watkins' vacancy symmetry model proposed for vacancy defects in Silicon (sub-section 3.2.7), where electron density in dangling bonds is symmetrically distributed on neighboring atoms. In this case of V^0_{Te}, due to the high electronegativity difference between Cd and Te atoms, the defect electron density takes a

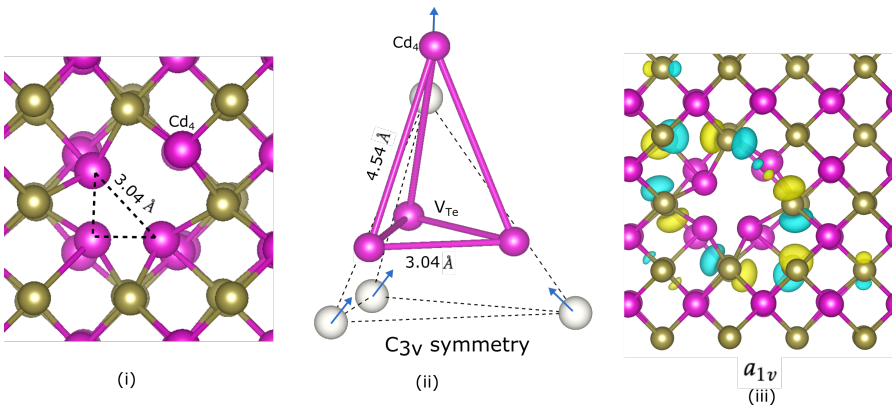

Figure 5.14: (i) Optimized geometry of neutral Te-vacancy showing the distance between three inward relaxed atoms; Cd_4 is the outward relaxed atom, (ii) change from T_d (un-relaxed) initial Cd-atom (white) tetrahedron neighboring Te vacancy to symmetry reduced C_{3v} Cd-tetrahedron (pink), (iii) a_{1v} defect state of Te-vacancy with electron-density 0.0025 e/Å^3.

trigonal distribution.

This trigonal symmetry of electron density is evident from the wavefunction plot corresponding to a_{1v} defect state as shown in Figure 5.14 (iii). V^0_{Te} with doubly occupied a_{1v} state have double donor character. The triply-degenerate t_{2v} defect states are empty, and due to C_{3v} symmetry split in two doubly-degenerate e_{2v} and singlet a_{2v} states present well above the conduction band at energy 0.76 eV +CBM and 1.10 eV +CBM respectively. Three of the four Cd neighboring atoms at the vacancy site move inward by 0.72 Å and are placed at a distance of 3.04 Å from each other. The fourth Cd atom relaxes outward and moves away from the vacancy site by 0.54 Å along the 111 axis.

Cd-antisite

In the case of Cd-antisite (Cd_{Te}), the defect has 2 electrons corresponding to Cd atoms tetrahedrally coordinated to Cd_{Te} atom and 2 electrons corresponding to the Cd_{Te} atom. In our calculation, we found out that the doubly occupied a_{1v} state lies well deep in the valence band, and the triply degenerate t_{2v} states are empty, lying well above the CBM by 0.41 eV.

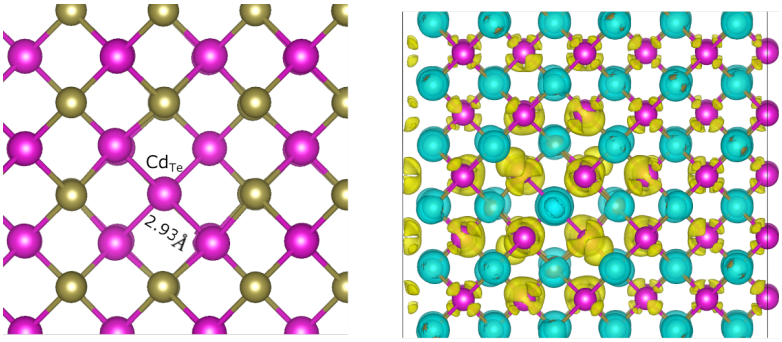

Figure 5.15: (i) Ground state structure of Cd-antisite (zoomed on defect site) with T_d symmetry; showing Cd-Cd distance, (ii) Kohn-Sham isosurface of PHS resonant with CBM with electron-density 0.0008 e/Å^3

This is driven by the fact that the two defect electrons reside in the conduction band minima (CBM) in a perturbed host state (PHS) manner weakly bound to the impurity in an effective mass donor state. These 2 electrons are de-localized over the whole super-cell of 216 atoms. The corresponding wavefunction of CBM is shown in Figure 5.15 (ii), hosting 2 electrons. This occupation of 2 electrons in CBM is consistent with the fact that Cd_{Te} has a local T_d symmetry around the defect site and shallow double donor character.

Te-antisite (Te_{Cd}), Cd-interstitial (Cd_i), Te-interstitial (Te_i) defects have a character where the a_{1v} and t_{2v} are completely filled as there are no unsaturated dangling bonds present. They result in the creation of a_{1c} and t_{2c} states from the conduction band as the number of electrons on the defect site is higher than the number of electrons in the corresponding pristine (defect-free) CdTe T_d site.

Te-antisite

In the case of neutral Te-antisite (Te^0_{Cd}), the defect center have 6+6 = 12 localized electrons: six electrons contributed by the Te atoms present on tetrahedron around Te_{Cd} site and six electrons from Te_{Cd} atom. These electrons fill $a_{1v}(2)$, $t_{2v}(6)$, $a_{1c}(2)$ and $t_{2c}(2)$ states. The states a_{1c} and t_{2c} are anti-bonding in character. The partially filled triply degenerate $t_{2c}(2)$ lead to symmetry breaking of t_{2c} states in to doubly occupied singlet $a_{2c}(2)$ and empty doubly-degenerate $e_c(0)$ states resulting in Jahn-Teller distortion reducing local symmetry from T_d to C_{3v}. This C_{3v} symmetry is consistent with previously reported calculations[72,116]. The defect state a_{1c}, as a consequence of symmetry breaking and large local lattice distortion, is localized onto the three Te atoms coordinated with

the Te-antisite atom hosting a lone pair and lies well below VBM. The a_{2c} and e_c defect states lie in the band gap at 0.16 eV above VBM and in the conduction band at 0.73 eV above CBM respectively.

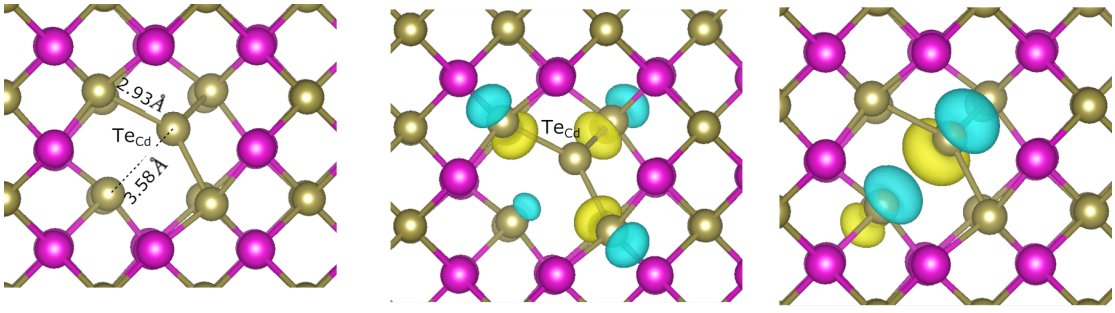

(i) (ii) (iii)

Figure 5.16: (i) Te-antisite atom distance with four neighboring Te-atoms in C_{3v} symmetry, (ii) and (iii) Kohn-Sham wavefunction isosurfaces of a_{1c} and a_{2c} defect states with electron-density of 0.0035 e/Å^3 and 0.0050 e/Å^3 respectively.

Doubly occupied a_{2c} state is anti-bonding in character localized on Te_{Cd} antisite atom and one of the 4 Te-neighboring atoms as shown in Figure 5.16 (iii). This anti-bonding interaction brings about the Te_{Cd} atom displacement along the vector joining the two atoms in [111] direction increasing the distance between them. The Te-antisite and Te atom involved in anti-bonding are placed at a distance of 3.58 Å. This changes the Te_{Cd} bond length with the other three neighboring atoms to 2.93 Å only slightly longer in comparison to the Cd-Te bond in pristine CdTe (2.78 Å). Te-antisite has a deep double donor character resulting from the two electrons residing in the anti-bonding state deep in the band gap.

Unlike Te_{Cd} defect, interstitial defects do not represent the condition where dangling bonds need to be passivated by the electrons from the substitutional defect atom. In this case, interstitial atom defect electrons fill a_{1c} and t_{2c} states.

Cd-interstitial

For the case of interstitial defects in a zinc-blende lattice, two high symmetry T_d sites are possible, one where the interstitial atom is tetrahedrally coordinated with cation(Cd) and the other with anion (Te) atoms. In neutral charge state Cd_i^0, the configuration with tetrahedrally coordinated Cd atom is more stable. The defect is characterized by two interstitial atom electrons residing in a_{1c} defect state lying at 0.42 eV above

VBM and empty t_{2c} states lying above CBM.

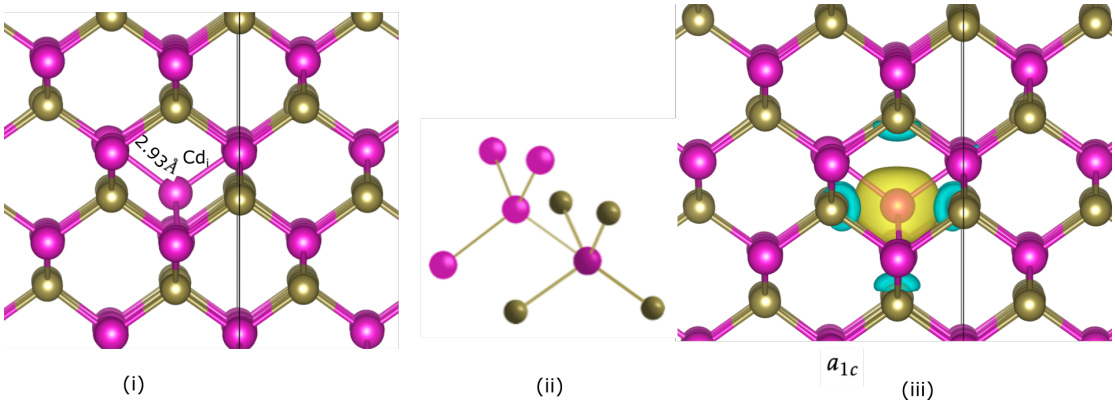

Figure 5.17: Cd-interstitial with T_d symmetry bonded with four Cd-atoms, (ii) Cd-interstitial local environment, (iii) wavefunction iso-surface of Cd-interstitial a_{1c} defect state with electron-density 0.0045 e/Å^3.

The Cd_i have a double donor character resulting from localized electrons with the singlet energy level present in the band-gap. The barrier of diffusion for Cd_i in previous calculations is reported to be 0.36 eV, which is very low. Consequently, the concentration of Cd_i defects in CdTe is expected to be significantly small[253].

Te-interstitial

Te_i has 6 electrons occupying the $a_{1c}(2)$ and $t_{2c}(4)$ defect states. In our calculations, we observe that neutral Te_i is unstable against the structural relaxation that displaces the Te_i atom towards a regular Te lattice site such that it shares the regular Te site and forms a split interstitial $(Te - Te)_{spl}$ (Figure 5.18).

The Te_i and the Te-regular site atom forms a bond such that the Te-Te dimer is aligned along the 110 direction. The distortion is driven by partially filled triply degenerate $t_{2c}(4)$ states. The symmetry breaking split the t_{2c} state into three non-degenerate states. As the split interstitial configuration does not have any symmetry axis higher than C_2 rotation symmetry. One of these states is doubly occupied and lies deep in the band-gap positioned at 0.3 eV above VBM and is responsible for the double-donor character of the Te_i. The other two empty singlet states resulting from degeneracy breaking of t_{2c} states lie in the conduction band. The doubly occupied state present in the band-gap is responsible for the double donor character of Te_i.

In the next section, we will discuss the interaction of Cr and Mn dopants with native defects. We try to understand the dopant-defect interactions based on the single-particle states that are active and lie in the band-gap and the hybridization overlapping of the

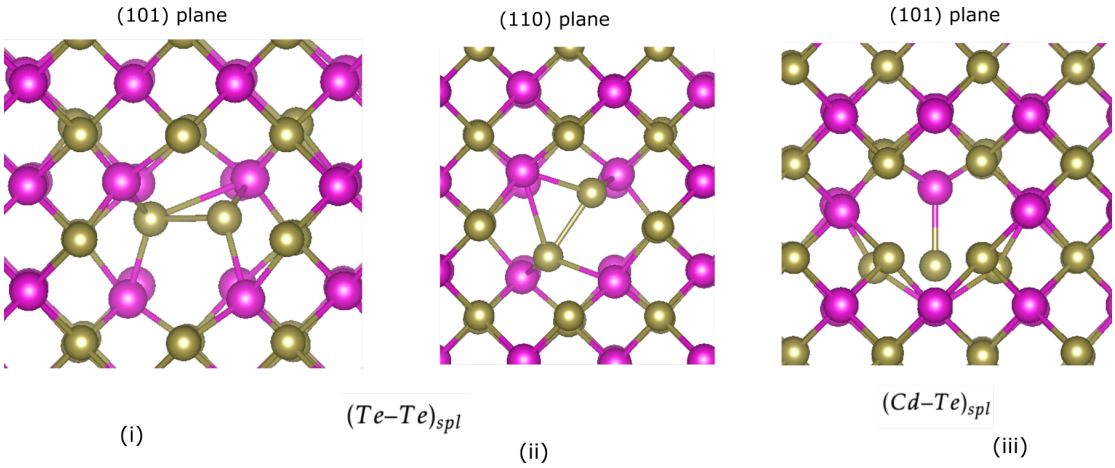

Figure 5.18: (i)-(ii) 101 and 110 planar views of ground state interstitial configuration of Te_i aligned along 110 axis respectively, (iii) 101 planar view meta-stable configuration with Cd-Te split interstitial at Cd-site.

orbitals that can result.

5.7 Cr and Mn dopants interaction with native defects in neutral charge state

Magnetic properties in the case of TM-doped semiconductors are typically dependent on the growth conditions and co-doping. We have attributed here that one factor leading to a low concentration of Cr-doped QDs is driven by the fact that the TM impurities can interact with intrinsic defects present in CdTe. The formation of such defect complexes can effectively change the character of TM ions in terms of magnetic and charge state. The relative position and symmetry of in gap electronic levels induced by intrinsic point defects can thus drive about a change in the TM impurity defect states. This thus implies that the characteristic signature spectra of defect complex(es) in magneto-optical experiments could be significantly different than the isolated dopants.

To evaluate the tendency towards defect complex formation, we calculated the binding energies associated with the defect configurations where the TM ion is placed at the closest distance from intrinsic defects (with each intrinsic defect in a separate simulation context). The interactions where the TM ion is present in the closest vicinity to one of the intrinsic defects in a supercell are considered as defect-bound complex configurations. A detailed description of binding energy formulation is given in the sub-section 3.2.6 of Chapter 3. The binding energy (E_b), in this particular context for TM and intrinsic defects interaction, is defined as $E_b = E_f[TM] + E_f[I.D.] - E_f[TM - I.D.]$.

The $E_f[TM - I.D.]$ is formation energy when the two defects are present in the simulation box at the closest distance. The $E_f[TM]$ and $E_f[I.D.]$ are the formation energy of isolated TM impurity in CdTe and isolated intrinsic defect, respectively. The acronym I.D. is used here in this particular instance for intrinsic defects. The closest distance for TM ion and an intrinsic defect at the Te site (i.e. V_{Te} and Cd_{Te}) is 2.78 Å and that of Cd-site (i.e. V_{Cd} and Te_{Cd}) is 4.54 Å in an unperturbed lattice.

Defects interaction are described as favorable and unfavorable based on the sign(±) of the dopant-defect binding energy. A positive E_b value indicates that there is a thermodynamic driving force for defect complex formation, whereas a negative E_b suggests otherwise. The E_b (positive) values are larger when the association of defect is driven by charge-compensation and charge transfer. Small values of E_b suggest that the defect complex is susceptible to dissociation. Here we have defined $E_b > 0.1$ eV to be sufficiently large to avoid dissociation. The binding energies $E_b < 0.05$ eV are considered as very small, and such interactions are considered feeble associations. This threshold value is taken by keeping in mind the thermal energy associated with the degree of freedom at room temperature.

The calculated E_b values can be understood in the context of the growth process

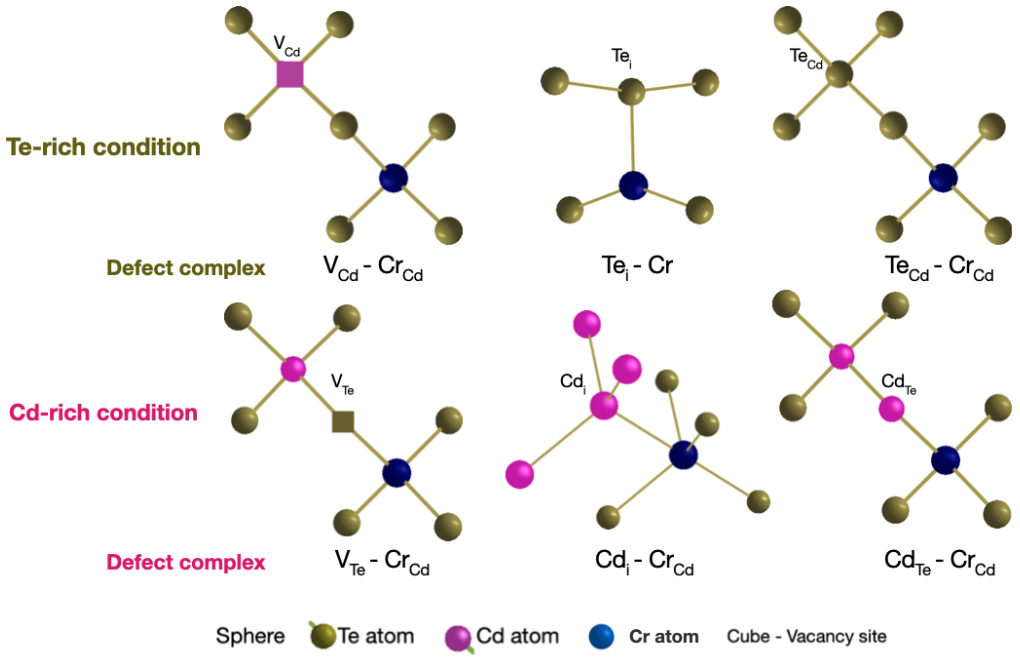

Figure 5.19: Local initial structure of the defect-complexes considered for Cr (and Mn) impurity interaction with native defects of CdTe.

that typically can either be Te-rich or Cd-rich. In the case of the Cd-rich limit as per the elemental pressure, during the growth, the major intrinsic defects present are likely to be Cd_i, Cd_{Te}, and V_{Te} roughly speaking in order of increasing concentration. Similarly, in the case of Te-rich limit Te_i, Te_{Cd}, and V_{Cd} are the major intrinsic defects present.

The E_b values calculated for all the defect complexes are given in the Table 5.1

5.7.1 Te-rich limit

There is a complete contrast in the interaction character of Cr and Mn dopants with the intrinsic defects present in CdTe. In the case of the Te-rich limit, positive E_b values are calculated for each dopant and native defect interaction. These interactions are regularly referred to as dopant-defect interactions in the following text. The E_b values suggest that Cr_{Cd} dopant interacts with Te-rich condition major intrinsic defects and forms tight bound complexes. In contrast, for Mn_{Cd} dopant calculated E_b values are small interactions, and dopant-defect interactions are weak. This large difference is attributed to two important factors *(i)* lattice distortion induced by impurity and *(ii)* the impurity-associated defect states. Mn_{Cd} substitutional impurity has high stability as it

Table 5.1: Binding energy (E_b) values calculated with ground state configurations of the dopant-defect complexes and isolated defects for Cr and Mn impurity in both Te-rich and Cd-rich conditions

	Binding energy E_b (eV)					
Impurity	Native defects in CdTe					
	Te-rich condition			Cd-rich condition		
	V_{Cd}	Te_i	Te_{Cd}	V_{Te}	Cd_i	Cd_{Te}
Cr_{Cd}	0.67	0.21	0.12	-0.13	0.39	0.45
Mn_{Cd}	0.09	0.06	0.02	-0.31	0.23	-0.17

Green - considerable binding with *Eb* > 0.1 eV
Yellow - weak binding with 0 eV < *Eb* < 0.1 eV
Red - binding unfavourable *Eb* < 0 eV

does not induce any significant lattice distortion, and also deep localized defect states do not emerge in the band-gap (Figure 5.6 and 5.7). In contrast, the Cr_{Cd} dopant induces large structural distortion in terms of Jahn-Teller distortion and induces both localized filled and empty defect states in band-gap (comparatively less dispersed than Mn_{Cd}). These defect states can overlap (hybridize) with the intrinsic defect electronic states to form stable defect complexes.

In the case of dopants interaction with the V_{Cd}, the interactions are driven by the double-acceptor character of the V_{Cd}. The electrons from the TM d-type state hybridize with dangling bond Te-p states of V_{Cd}. This orbital interaction/overlapping leads to the transfer of two electrons from the spin-up channel of Cr_{Cd} and Mn_{Cd} impurities to the localized hole levels in the spin-down channel of V_{Cd} with t_2 character (later shown in Figure 5.23). A schematic diagram for such an interaction is shown in Figure 5.12 of sub-section 5.5. This results in the change of spin state for Cr_{Cd} and Mn_{Cd} isolated dopants from S=2 and S=5/2 to S=1 and S=3/2 corresponding to $Cr_{Cd}-V_{Cd}$ and $Mn_{Cd}-V_{Cd}$ respectively on defect complex formation with V_{Cd}. Positive E_b energy values of 0.67 and 0.09 eV for $Cr_{Cd} - V_{Cd}$ and $Mn_{Cd} - V_{Cd}$ defect complexes are calculated, representing the favorable association.

For Mn_{Cd} impurity, all the d-orbitals derived (hybridize with Te-p orbitals) states in the spin-up channel are completely filled, and all the localized spin-down states are empty. Thus, Mn_{Cd} can act as a weak donor by interacting with holes. The reason being the defect states corresponding to Mn_{Cd} are relatively dispersed compared to Cr_{Cd} and are resonant with VBM. In the case of Cr_{Cd} impurity, doubly degenerate filled states and empty states are placed in the band gap and are highly localized (Figure 5.9). Therefore, Cr_{Cd} can accept and as well as donate electrons.

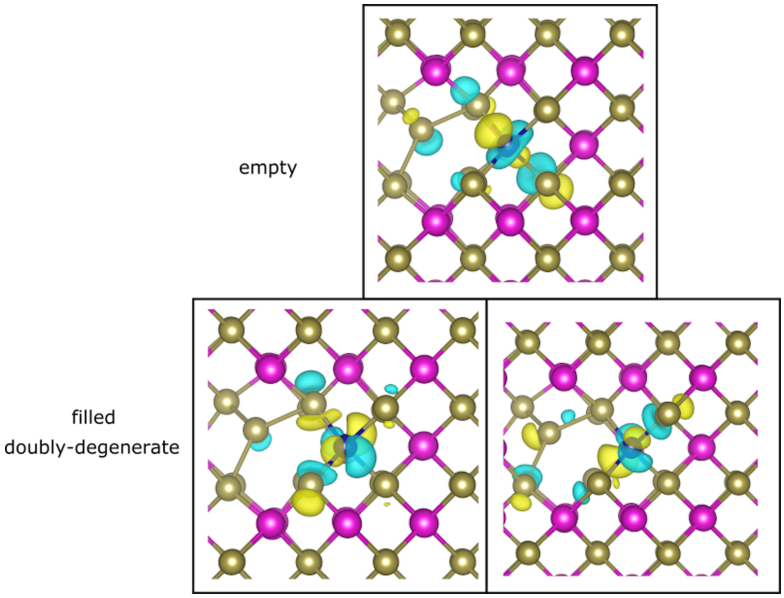

Figure 5.20: Kohn-Sham wavefunction isosurfaces corresponding to the localized states of $Cr_{Cd}-Te_{Cd}$ defect complex present in band-gap showing strong hybridization plotted with the electron-density value of 0.0035 e/Å^3.

Intrinsic defects Te_i and Te_{Cd} both have localized doubly occupied defect states present in the band-gap and are deep donor defects by character. Although these two intrinsic defects are donor defects, the interaction of Te_i and Te_{Cd} defects does not involve charge self-compensation or electron transfer. This is brought by the fact that the Fermi energy of Cr_{Cd} isolated impurity system is placed at 0.52 eV above VBM, and the doubly occupied states from Te_i and Te_{Cd} intrinsic defect lie at a lower energy of 0.3 eV and 0.16 eV above VBM respectively. Although, positive E_b values of 0.21 and 0.12 eV corresponding to $Cr_{Cd} - Te_{Cd}$ and $Cr_{Cd} - Te_i$ defect complexes are calculated respectively. These values suggest a favorable association, resulting from the hybridization of the d-type localized states of Cr_{Cd} and defect-induced localized states of Te_i and Te_{Cd}. This hybridization is driven by the fact that the Cr_{Cd} impurity defect states and native defects Te_i and Te_{Cd} induced states are localized and are present in the band gap. The localized defect states of $Cr_{Cd} - Te_{Cd}$ defect complex present in the band-gap resulting from the hybridization of Cr_{Cd} and Te_{Cd} defect states are shown in the Figure 5.20.

Te_i, in particular, is a fast mobile defect with a low barrier for diffusion of 0.21 eV and is very likely to be not present in CdTe bulk or QDs. Te_i fast converts into the stable Te_{Cd} defect on interaction with V_{Cd} or diffuses to the surface.

We will further discuss in detail the case of V_{Cd} interaction with TM ions in the following sub-section 5.7.3 to understand the dopant-defect interactions in terms of orbital overlap and also explain the reason for large positive E_b value for the case of $Cr_{Cd} - V_{Cd}$ and considerably smaller E_b value in case of $Mn_{Cd} - V_{Cd}$.

5.7.2 Cd-rich limit

In the case of the Cd-rich limit, native defects Te vacancy (V_{Te}) and Cd-interstitial (Cd_i) show a very similar character in terms of interaction with both the Cr_{Cd} and Mn_{Cd} dopants. Large negative E_b values (-0.13 and -0.31 eV) calculated for the TM dopants and Te vacancy interactions imply that there is no signature of association of V_{Te} with Cr_{Cd} and Mn_{Cd} dopants. Although, Te vacancy defect site is adjacent to TM_{Cd} defect site present at a distance of 2.78 Å. Of the two main reasons driving this behavior: *(i)* First one stems from the vacant adjacent Te site, and results in TM_{Cd} dopant having one dangling bond (5.21) leading to energy destabilization *(ii)* Second is the position and character of doubly occupied defect state corresponding to the V_{Te}. The defect a_{1v} state lies well below the VBM by 0.32 eV. The empty e_{2v} and a_{2v} defect states of V_{Te} lie well above CBM. The V_{Te} defect a_{1v} state in terms of symmetry and relative energy does not overlap with t_2 like states of TM localized state. The overlapping and hybridization are not possible, as the V_{Te} defect state is rather dispersed onto the Te-atoms away from the TM dopant and vacancy site. The wavefunction plot corresponding to the case of $Cr_{Cd} - V_{Te}$ defect complex is shown in the Figure 5.21

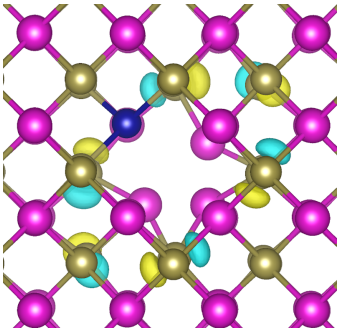

Figure 5.21: Kohn-Sham wavefunction isosurface of a_{1v} defect states of $Cr_{Cd} - V_{Te}$ defect complex with electron-density of 0.002 e/Å^3

For the case of Cd-interstitial (Cd_i) intrinsic defect, the configuration with tetrahedrally coordinated Cd-atoms is the most stable. On the defect complex formation $TM_{Cd} - Cd_i$, TM_{Cd} dopant forms one extra bond and is coordinated with five atoms. Also, the spatial overlap of the orbitals of TM_{Cd} and Cd_i favors a positive E_b value.

Therefor E_b values of 0.39 and 0.23 eV corresponding to $Cr_{Cd} - Cd_i$ and $Mn_{Cd} - Cd_i$ are calculated respectively. Although the Cd_i is a donor defect in character with a doubly occupied state present at 0.42 eV above VBM, the charge transfer to empty Cr_{Cd} defect present at 0.52 eV above VBM is not possible, as the fermi energy corresponding to the isolated Cr_{Cd} defect is higher than the defect level position of Cd_i in the band-gap.

On the other hand, in the case of TM interaction with Cd_{Te}, TM_{Cd} is coordinated with only four atoms (1 Cd atom, 3 Te atoms), as shown in Figure 5.22. The calculated E_b values suggest that dopants Cr_{Cd} and Mn_{Cd} behave in a contrasting manner for dopant-defect interaction with the Cd_{Te} defect. A sufficiently large positive E_b value of 0.45 eV is calculated for $Cr_{Cd} - Cd_{Te}$ defect complex. Whereas, a large negative value of -0.31 eV is calculated for $Mn_{Cd} - Cd_{Te}$ defect complex. In the case of isolated Cd_{Te} intrinsic defect, no defect state lies in the band-gap. The doubly occupied defect a_{1c} state lies deep in the valence band, and the other two electrons are occupied into de-localized CBM. As there are no active electrons present in the band gap, defect interaction driven by an overlap of the localized orbitals of TM_{Cd} and Cd_{Te} defect is not possible.

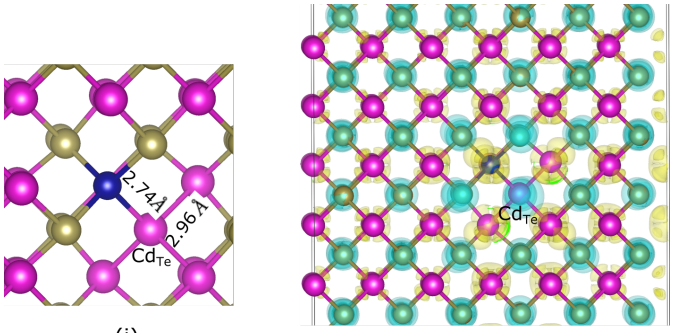

Figure 5.22: (i) $Cr_{Cd} - Cd_{Te}$ defect complex C_{3v} symmetry structure, (ii) wavefunction isosurface of the PHS of $Cr_{Cd} - Cd_{Te}$ with electron-density of 0.0008 e/Å^3

Although the charge compensation interaction of impurity and Cd_{Te} native defect is possible, Mn_{Cd} dopant having no acceptor electronic levels do not show a favorable E_b for association with Cd_{Te} donor defect. Two defect electrons of Cd_{Te} that are present in shallow dispersed state resonant with CdTe bulk CBM are de-localized over the whole supercell in perturbed host state(PHS) shown in Figure 5.22. In the case of isolated Cr_{Cd} impurity, as there is an empty state present at 0.09 eV below CBM, a charge self-compensation interaction between Cr^-_{Cd} and Cd^+_{Te} is possible. In other words, a charge transfer from shallow de-localized Cd_{Te} defect state resonant in CBM is possible to the Cr_{Cd} empty state. This leads to the formation of a strongly bound defect complex

$Cr_{Cd} - Cd_{Te}$ represented by E_b value of 0.45 eV.

Summary of the E_b values calculated for all the considered dopant-defect interactions and the interpretation.

In the case of the Te-rich limit, Cr_{Cd} favorably interact strongly with all three major defects (V_{Cd}, Te_{Cd}, Te_i) and Mn_{Cd}, in contrast, interact weakly. The positive E_b values for these dopant-defect interactions implies that the defect complexes have lower formation energy than the isolated defects. As the possibility of the defect formation is directly related to the formation energy, defect complex formation in the case of Cr-doped CdTe bulk and QDs is very likely. Consequently, in experiments, the isolated Cr_{Cd} dopant concentration in CdTe bulk and single dopant QDs grown under Te-rich conditions is likely to be low in comparison to isolated Mn_{Cd} dopant.

In the case of the Cd-rich limit, both the TM dopants interact strongly with Cd_i intrinsic defect. Although according to previous DFT calculations[104], Cd_i has a very low barrier for diffusion, and it is quite possible during the growth process, Cd_i may diffuse to the surface or present mostly at the CdTe/ZnTe interface in case of CdTe QDs grown over ZnTe. The Cd_{Te} on the other side has contrasting behavior in terms of interaction; the native defect interacts strongly with Cr_{Cd} and does not interact with Mn_{Cd} dopant. Thus, it is very likely that in the Cd-rich limit as well, the concentration of isolated dopant Cr_{Cd} in CdTe bulk and QDs will be low in comparison to Mn_{Cd} and considerably limited by the presence of intrinsic defects.

These results establish strong evidence for the assumption that the intrinsic defects are likely to be the reason for the limited number of isolated Cr-doped QDs, as observed by our experimental collaborators (Besombes *et. al.*) The presence of negatively charged $Cr^+ - hole$ complex as observed in the case of Cr doped CdTe/ZnTe QDs also supports our observation of charge-compensation interaction of Cr_{Cd} and donor Cd_{Te} defect.

In the next section, we will discuss in more detail the dopant-defect interaction of Mn_{Cd} and Cr_{Cd} dopants with the native defects V_{Cd} and Cd_{Te}. These two cases attracted our interest for further analysis for the obvious reason of charge transfer bound defect complexes and high positive E_b values in the case of Cr_{Cd}.

5.7.3 Charge transfer on Cr and Mn impurity interaction with V_{Cd} vacancy

The defect complex formation for $TM_{Cd} - V_{Cd}$ are driven by charge transfer from TM occupied defect levels to empty V_{Cd} defect levels, as explained in the last section. A defect levels diagram showing Kohn-Sham states corresponding to the isolated defects and defect complexes is shown in Figure 5.23.

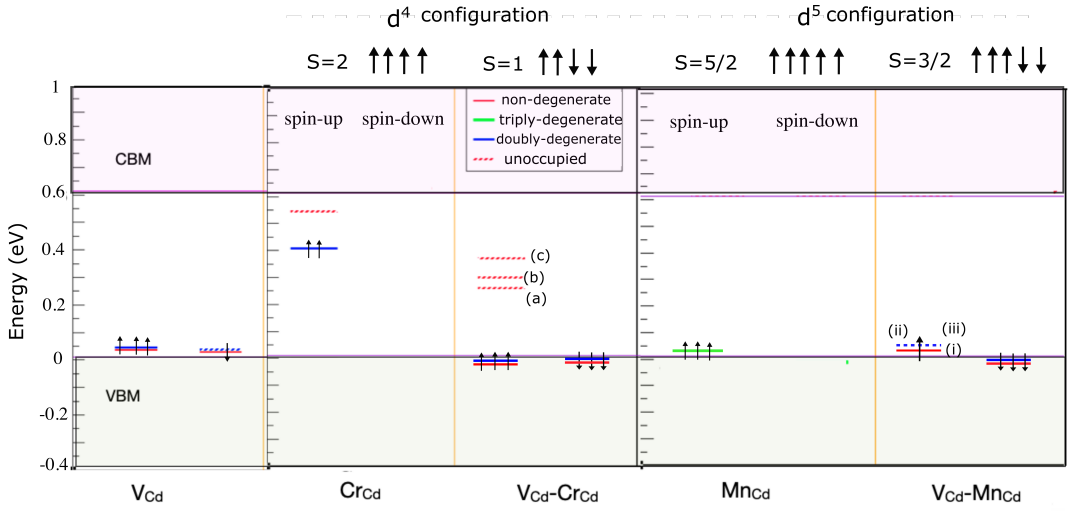

Figure 5.23: Defect levels diagram of isolated defects V_{Cd}, Cr_{Cd}, Mn_{Cd} and defect complexes $Cr_{Cd} - V_{Cd}$ and $Mn_{Cd} - V_{Cd}$. In four of the cases Cr_{Cd}, Mn_{Cd}, $Cr_{Cd} - V_{Cd}$ and $Mn_{Cd} - V_{Cd}$ two filled localized electronic levels contributing to net spin are not shown as they lie resonant in valence band at different positions w.r.t. VBM.

Only the energy levels lying in the band gap or close to the valence band edge with significant localization of electron density around the defect are shown. Energies of the Kohn-Sham states are shown in reference to the pristine CdTe bulk band-edges. A clear result of such an interaction is the change in the number of unpaired electrons for isolated Cr_{Cd} and Mn_{Cd} impurities from 4 and 5 electrons to 2 electrons (S=1) and 3 electrons (S=5/2) respectively on defect complex formation ($TM_{Cd} - V_{Cd}$).

In the case of unperturbed lattice (before the geometry relaxation) for the $TM_{Cd} - V_{Cd}$ defect complexes, both TM_{Cd} and V_{Cd} defects have C_{3v} local site(point) symmetry. At the impurity site, the TM_{Cd} is bonded with 4 Te atoms, of which one is under-coordinated. Due to the same argument, the point symmetry at V_{Cd} site is also C_{3v}. On geometry optimization in the case of $TM_{Cd} - V_{Cd}$, this C_{3v} symmetry on both sites is completely broken as shown in the Figure 5.24 (in case of C_{3v} symmetry Te-Te distances make two triads with 3 Te-Te distances being same).

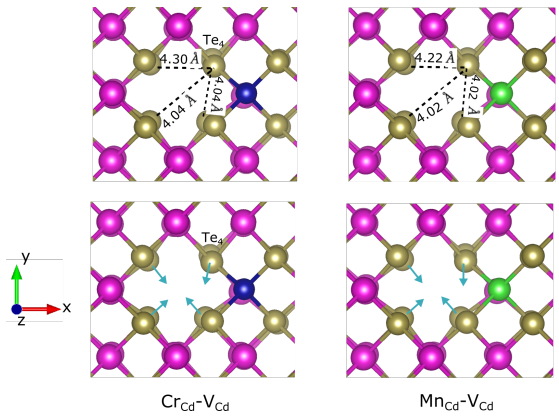

Figure 5.24: Optimized geometry of $Cr_{Cd} - V_{Cd}$ and $Mn_{Cd} - V_{Cd}$ defect complexes with selected Te-Te distances and arrows representing the displacement of four Te atoms at vacancy site. The Te-atom common to both TM_{Cd} and V_{Cd} is marked as Te_4. The displacement arrows reflect the breaking of C_{3v} symmetry.

This symmetry breaking is driven by the displacement of Te-atom, shared by both defect sites considerably in 001 direction by $|\delta z| = 0.32$ Å($|\delta x| = |\delta y| = 0.05$ Å) for $Cr_{Cd} - V_{Cd}$ case, and $|\delta z| = 0.36$ Å($|\delta x| = |\delta y| = 0.0$ Å) for $Mn_{Cd} - V_{Cd}$. In comparison, the other three atoms on the vacancy site in both cases relax inward towards the vacancy site with $|\delta x| = |\delta y| = |\delta z| = 0.22$ Å.

The spatial symmetry breaking around the Cr_{Cd} site also leads to symmetry breaking of defect electronic levels. Three non-degenerate localized empty-states in band-gap are present in case of $Cr_{Cd} - V_{Cd}$, whereas in case of $Mn_{Cd} - V_{Cd}$ one filled and two empty states are present in band-gap (Figure 5.23). The respective positions for the defect levels for $Cr_{Cd} - V_{Cd}$ marked as (a), (b), and (c) in Figure 5.23, are at 0.22 eV, 0.28 eV, 0.35 eV above VBM respectively. In the case of $Mn_{Cd} - V_{Cd}$, the defect states (i), (ii), and (iii) are present at 0.006 eV, 0.011 eV, and 0.011 eV above VBM. Corresponding wavefunction plots of Kohn-Sham states are shown in Figure 5.25.

To understand the charge transfer or/and the hybridization of electronic states of TM_{Cd} and V_{Cd}, we did the charge analysis on the atoms involved in the defect complex based on the radial integration of electron density around the TM_{Cd} and V_{Cd} site (Bader change analysis, in this particular case, did not provide correct Voronoi volume description around the TM defect atom and therefore was not used). The analysis did not show any significant signature of charge transfer from TM_{Cd} site to V_{Cd} (Figure 5.26). Therefore, the difference in the number of unpaired electrons in the case of $TM_{Cd} - V_{Cd}$ defect complexes and isolated TM impurity defect is driven by the hybridization of vacancy and impurity electron levels and passivation of holes due to this hybridization rather

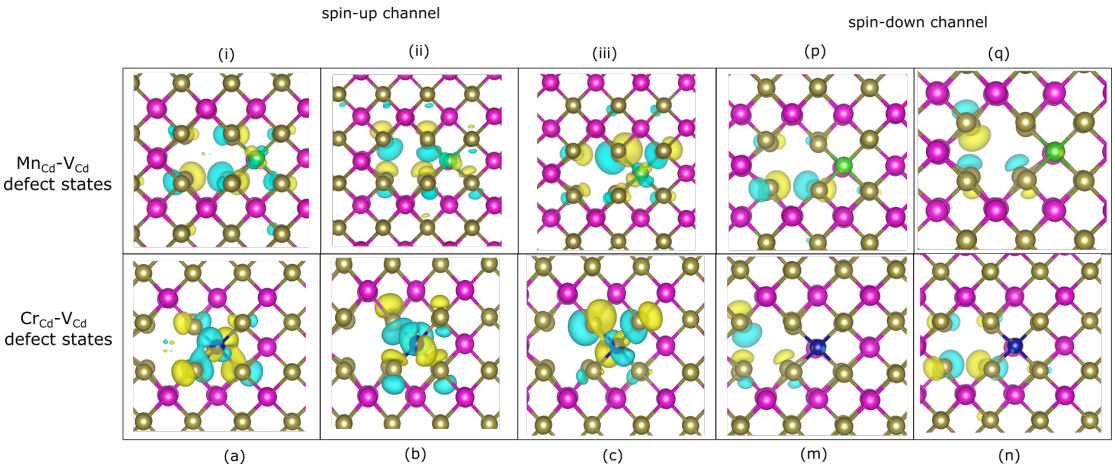

Figure 5.25: Kohn-Sham wavefunction iso-surfaces corresponding to defect states lying in the spin-up channel band-gap for $Mn_{Cd} - V_{Cd}$ (marked as (i), (ii) and (iii))and $Cr_{Cd} - V_{Cd}$ (marked as (a), (b), and (c)) defect complexes with electron-density 0.002 e/Å^3 and 0.0035 e/Å^3 respectively. Along-side doubly degenerate filled defects states of $Mn_{Cd} - V_{Cd}$ (marked as (p) and (q))and $Cr_{Cd} - V_{Cd}$ (marked as (m), and (n)) defect complexes in the spin-down channel are shown with the electron-density value of 0.0025 e/Å^3 for both the cases

than a site to site charge transfer.

Localized defect states in the spin-down channel are present near the top of the valence band for both $Cr_{Cd} - V_{Cd}$ and $Mn_{Cd} - V_{Cd}$ defect complexes. Two filled states at the top of the valence band in the spin-down channel localized on the V_{Cd} defect site show the clear signature of the transfer of electrons from spin-up defect levels to spin-down levels (consistent with the schematic diagram shown in the Figure 5.12). The wavefunction plots of double degenerate states (Figure 5.23) in the spin-down channel for both the defect complex $Cr_{Cd} - V_{Cd}$ (marked as (m) and (n)) and $Mn_{Cd} - V_{Cd}$ (marked as (p) and (q)) indicating a transfer of 2 electrons from spin-up channel to the spin-down channel are shown in the Figure 5.25

The defect complex formation of $Mn_{Cd} - V_{Cd}$ is consistent with the donor character of Mn^{+}_{Cd} and $(Mn^{+} - V^{-}_{Cd})^{-}$ defect complex formation reported in the experiment by Solodin *et al.* [252,254].

We also explored the possibility of change in the spin state of Cr_{Cd} in the presence of V_{Cd} defect, when two defects are present at a farther distance. We considered the case where Cr_{Cd} and V_{Cd} defect are placed at a distance of 9.09 Å. In this configuration as well, we calculated that the spin state changes for Cr_{Cd} impurity (with Cd vacancy in close vicinity) to S=1 relative to isolated Cr_{Cd} impurity spin state of S=2. Although,

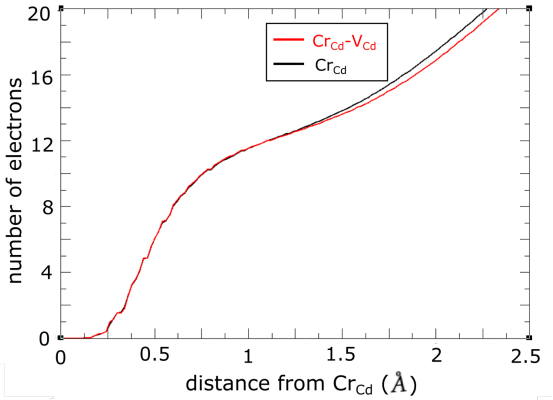

Figure 5.26: Radially integrated electron density around the Cr impurity site for isolated Cr_{Cd} defect (black) and $Cr_{Cd} - V_{Cd}$ defect complex (red)

this configuration is less stable than the bound defect complex configuration by 282 meV.

5.7.4 Oxidation state change on Cr impurity interaction with Cd_{Te} antisite

As discussed previously in this section 5.7, Cr_{Cd} impurity on interaction with Cd_{Te}, changes from d^4 to d^5 configuration. This is driven by the capture of one electron from the shallow native defect state into localized d-type state, on $Cr_{Cd}-Cd_{Te}$ defect complex formation. In this section, we go into further detail to analyze the Kohn-Sham defect eigenstates and their corresponding wavefunction plot for $Cr_{Cd}-CdTe$ defect complex.

In Figure 5.27 Kohn-Sham eigenvalues corresponding to the defect complex $Cr_{Cd}-Cd_{Te}$ and isolated defects are shown. Only defect states in the band gap and close to band edges are shown. For $Cr_{Cd}-Cd_{Te}$, no empty states are present in the band gap. The d-type state, which accommodates an electron captured from the CBM, moves deep in the valence band. The Kohn-Sham wavefunction plots of four localized states of d character (marked in 5.27) corresponding to $Cr_{Cd}-CdTe$ defect complex are shown in the Figure 5.28, after one of the delocalized electrons from the CBM is transferred to the empty Cr_{Cd} localized state.

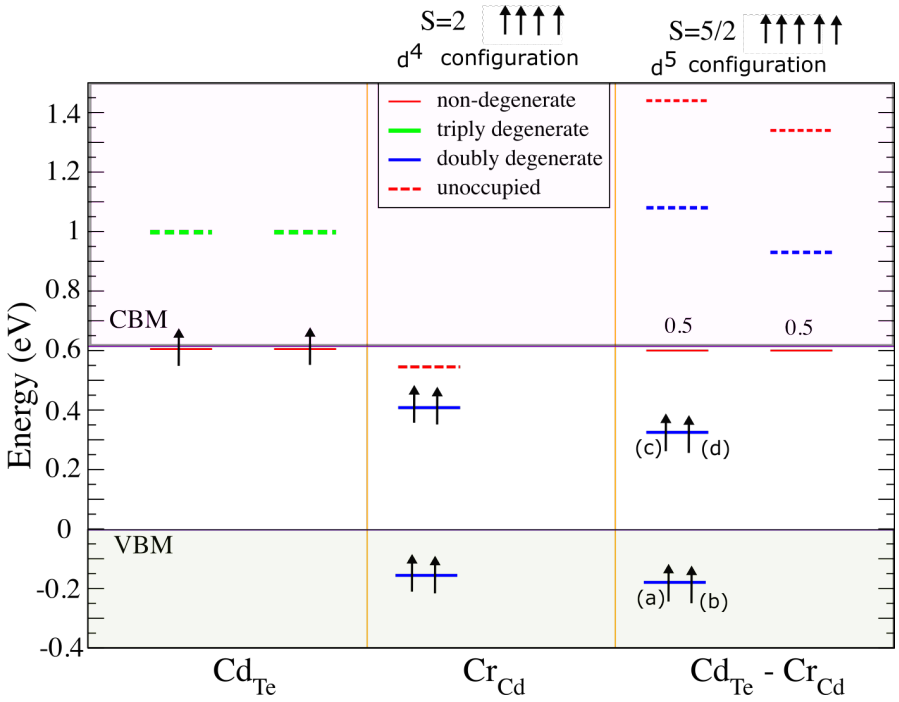

Figure 5.27: Defect level diagram of isolated defects Cr_{Cd}, Cd_{Te} and defect complex $Cr_{Cd}-Cd_{Te}$ showing defect induced states. PHS resonant with CBM in case of defect complex $Cr_{Cd}-Cd_{Te}$, host 0.5 electron in each spin-up and spin-down channel.

The CBM occupies only one electron with a fractional 0.5 electron occupation in each of the spin-up and spin-down states representing the degeneracy resulting from the symmetry. This fractional occupation suggests that the defect complex will preferably be more stable in $(Cr_{Cd} - Cd_{Te})^{+}$ charge state. $Cr_{Cd} - Cd_{Te}$ defect complex is characterised by C_{3v} symmetry. Unlike the case of $Cr_{Cd} - V_{Cd}$, the symmetry at both defect sites is maintained. Bond length of $Cr - Cd_{Te}$ (three), $Cr - Te$ (three), and $Cd_{Te} - Cd$ are 2.74 Å, 2.65 Å, and 2.96 Å respectively. In comparison $Cr - Te$ bond length in isolated Cr_{Cd} (four) are 2.65 Å and $Cd_{Te} - Cd$ (four) bond length in isolated Cd_{Te} defect are 2.93 Å. The t_{2c} defect state present in the conduction band at 0.41 eV above CBM localized in case of isolated Cd_{Te} native defect, on defect complex formation split in to the doubly degenerate e_c and a_{2c} placed at 0.41 eV and 0.82 eV above CBM in spin-up channel respectively (with exchange splitting of 0.13 eV).

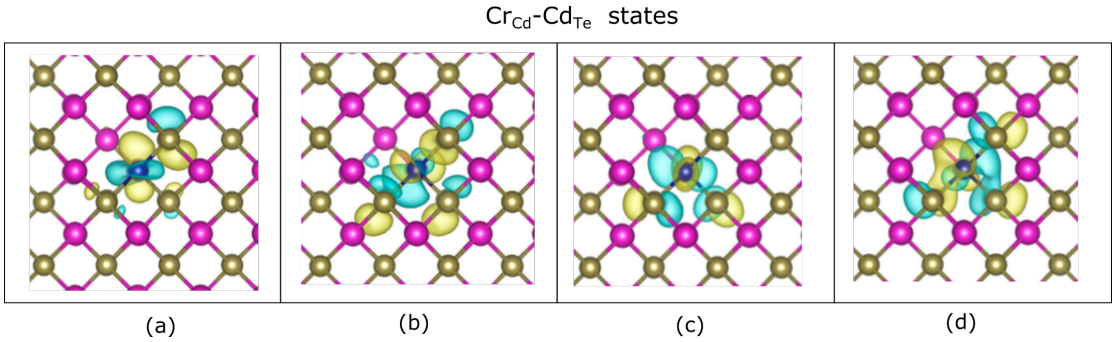

Figure 5.28: Kohn-Sham wavefunction isosurfaces corresponding to defect complex $Cr_{Cd} - Cd_{Te}$ localised defect states lying close to band-edges with electron-density 0.0035 e/Å^3

In the experiments performed on Cr doped CdTe DMSs by Lu *et al.*[255], the signature of negatively charged Cr dopant with +1 oxidation state, $(Cr^{+}(Cr^{-}_{Cd}))$ present in a very low concentration was reported. They suggested that the change in the oxidation state of Cr impurity results from some unknown background donor doping source. Our experimental collobrators, Besombes *et. al.*, highlighted that they stabilized an isolated $Cr^{+} - hole$ complex in CdTe QDs grown over the ZnTe surface. They pointed that results from photoluminescence spectra shows that the Cr^{+} oxidation state does not result from the capture of a free electron from the CdTe host and is rather resulting from the background doping. We, therefore tried to trace the source of this background donor defects using the results of our defect interaction calculations. As observed in our calculations, Cd_{Te} intrinsic defect does change the configuration of dopant Cr_{Cd} from neutral to negatively charged state when placed adjacent in $Cr_{Cd} - Cd_{Te}$ configuration

pointing to $Cr^{-}_{Cd} - Cd^{+}_{Te}$ character. However, the experimental observation of $Cr^{+} - hole$ complex in photoluminescence and opto-magnetic results was attributed to Cr^{-}_{Cd} with a local T_d symmetry. This signature of T_d symmetry is typical of Cr^{-}_{Cd} (Cr^{+}) isolated defect configuration. It was thus assumed by us that the source of background doping to be likely present at some distance from the Cr impurity, such that the intrinsic defect does not perturb the T_d symmetry of the Cr^{+} system with d^5 configuration.

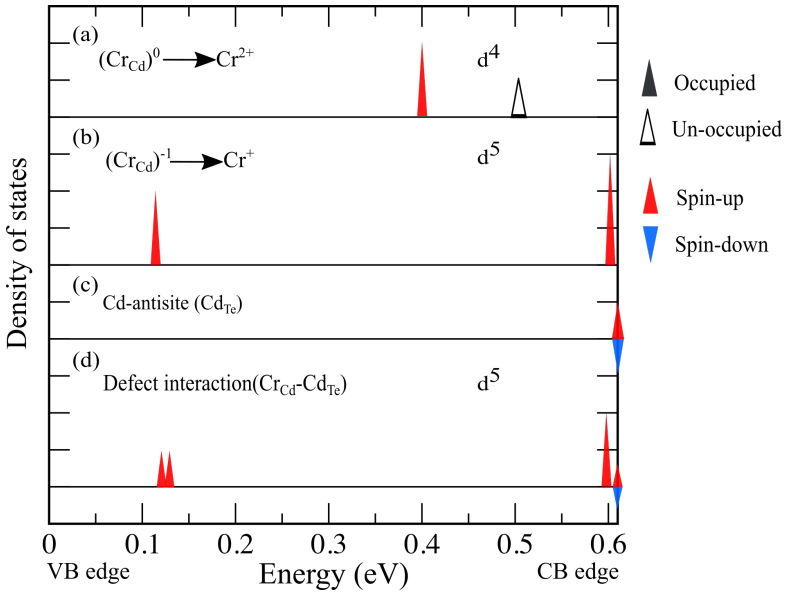

Figure 5.29: Kohn-Sham defect electronic states corresponding to (a) Cr^{0}_{Cd}, (b) Cr^{-}_{Cd}, (c) Cd_{Te}, (d) configuration with Cr_{Cd} and Cd_{Te} present at distance of ~ 9.5 Å.

As the Cd_{Te} is a shallow donor in character with delocalized electrons, it can act as a donor even if present at some distance from the Cr impurity. We, therefore, considered two additional configurations where Cd_{Te} defect is present at a distance of 5.32 Å and 9.49 Å (farthest possible in a 216 atom supercell) from Cr impurity. We realized that the calculated density of states in band-gap (as well as close to band-edges) and the Kohn-Sham eigenvalues for a configuration where Cd_{Te} and Cr_{Cd} are present at a distance of 9.49 Å matches identically with the Cr^{+} isolated defect. The density of states representing eigenvalues of Kohn-Sham states localized on the Cr_{Cd} site in case of isolated impurity in a negative charge state and configuration with Cd_{Te} native defect present in the vicinity are shown in the Figure 5.29. A very small splitting of doubly degenerate states present at the energy of 0.12 eV above VBM by 0.022 eV and triply degenerate state lying 0.03 below CBM by 0.008 eV was also calculated in the case where Cd_{Te} defect is present in the vicinity of Cr_{Cd}. The very small splitting as

calculated for this configuration is consistent with a small divergence from T_d symmetry for the d^5 configuration of Cr^+ as interpreted from the experimental results from our collaborators. However, this configuration with a distance of 9.49 Å between the two defects is less stable than defect bound complex configuration by 419.2 meV. The localized defect state at Cr_{Cd} defect site as calculated for isolated Cr^+ and supercell containing both Cr_{Cd} and Cd_{Te} at a distance 9.49 Å shows identical wavefunction, as shown in the Figure with same energy ordering (Figure 5.29).

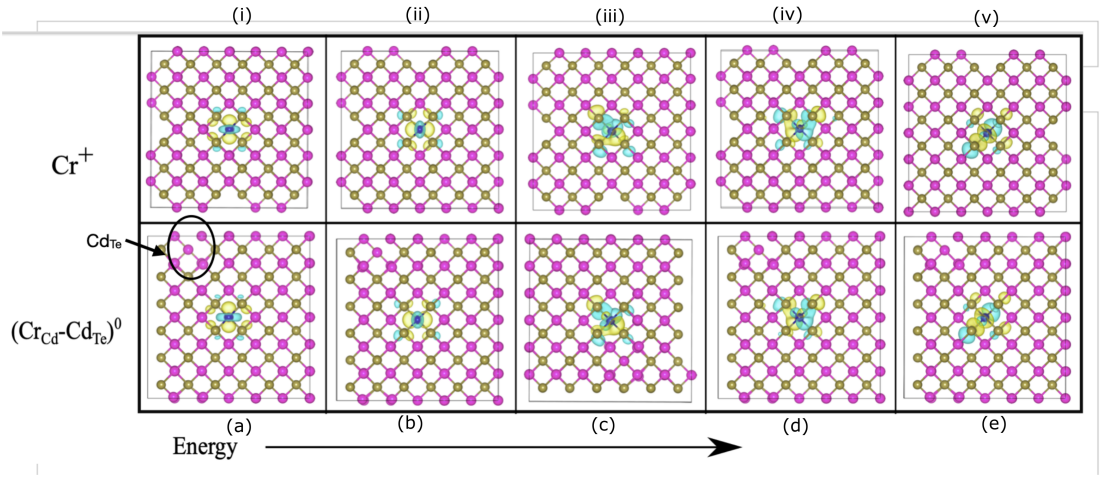

Figure 5.30: Kohn-Sham isosurfaces corresponding to the defect states present in band-gap for the isolated Cr^-_{Cd} and defect interaction configuration of Cr_{Cd} and Cd_{Te} placed at distance of $\sim$ 9.5 Å.

This gives ample support to the argument that the Cd_{Te} intrinsic defect present in the vicinity can donate an electron to Cr_{Cd} and change it to Cr^-_{Cd} state.

5.8 Conclusion

In this chapter, we have presented a detailed analysis of Cr and Mn solitary dopants' ground configuration and the interaction of two dopants with intrinsic defects present in the host CdTe. In the first part, we presented the experimental reported results for the two dopants from the EPR spectroscopy, which reveal the local symmetry of the lattice around the dopant. Then we have discussed the phenomenological models that present the link between the local symmetry present at the impurity site in the tetrahedral crystal field of lattice and the defect electronic states originating from transition metal d-orbitals in terms of Jahn-Teller distortion.

In the second part, we present our DFT calculated results with a discussion on respective ground state rD_{2d} and T_d local symmetry of Cr and Mn impurity defect and the electronic states originating in the band gap due to the presence of TM impurity. We established a one-to-one correspondence between the experimental reported local symmetry from EPR results, crystal field phenomenological models, and the wavefunctions of localized Kohn-Sham eigenstates present in the band gap or close to the band edges.

In the third part, we studied the interaction of TM dopants with the native defects present in the CdTe host, corresponding to both Te-rich and Cd-rich growth conditions. We first provided a brief discussion on the electronic structure of the native defects and their interpretation in terms of the character of defect electronic states. Then, we calculated the binding energies associated with the defect interaction of TM impurities and native defects. The values of binding energies were interpreted in terms of the electronic states corresponding to defect complexes and their comparison with the electronic states of isolated TM impurities and native defects. We proposed a small phenomenological model to guide the analysis of the interaction of TM impurities in II-VI semiconductors with native cation vacancy defects. The binding energy values pointed to a strong contrasting character difference between Cr and Mn impurities. The values suggested a very strong interaction of Cr dopants with the native defects present in CdTe in both Te-rich and Cd-rich conditions. In contrast, Mn interacts weakly with native defects present in the Te-rich conditions and interacts only with Cd interstitial defects under Cd-rich conditions.

Finally, we establish that the interaction of Cr with Cd-vacancy and Cd-antiste, intrinsic defects in Te-irch conditions, and Cd-rich conditions can lead to change in the spin and charge state of Cr, in comparison to the isolated configuration. The electronic structure of Cr impurity present in the vicinity of Cd-antisite (not as in a bound defect complex) showed a very similar signature as of isolated negatively charged Cr configuration. Using this configuration of Cr, we were able to provide reasoning for the Cr+ - hole complex detected in CdTe quantum dots through photoluminescence (PL) experiments by our experimental collaborators (which pointed to a change in the ground oxidation state of Cr from 2+ to +). Based on the electronic structure calculations, we proposed that it is quite probable that the Cr+ - hole complex observed in the experiment results from the charge transfer of an electron from Cd-antisite to Cr impurity.

CHAPTER 6

Conclusion

The need to improve the understanding of native defects, dopants, and defect complexes present in the CdTe devices is gaining a lot of attention. A great deal of interest stem from the application of CdTe in the field of commercial photovoltaics, medical imaging, and nuclear radiation detector semiconductor devices[57,61,128]. The field of Solotronics, in contrast to these well-developed applications of CdTe based devices, is in its initial stage, and there are a lot of open questions that need to be addressed, which are related to growth strategies to have control over a desired isolated defect configuration. Developing an understanding of point defects and growth strategies of semiconductor devices and Solotronics systems requires a combination of a theoretical and experimental approach. The experiments can investigate the full complexity of the real devices and growth process, while in parallel theoretical studies can provide information about the individual defects and defect complexes to build knowledge about the defects associated phenomenon at the atomic scale. Therefore the work presented in this thesis has been conceptualized in a manner to build comprehension of experimental reported results. We primarily focused on the calculation of physical properties associated with point defects, such as migration barriers and binding energies of defect complexes outlined in **Chapter 3**.

The first problem addressed in this thesis was dedicated to photovoltaic applications. In **Chapter 4**, we addressed the role of Selenium (Se) alloying in improving the efficiency of CdTe based solar cells. Specifically, the aim was set to improve the understanding of the effects of selenium related point defects present in CdTe bulk. The

motivation behind the work was the experimentally reported improvement in efficiency from 17 to over 22 percent, achieved through the formation of alloyed $CdSe_xTe_{1-x}$ absorber layer in the polycrystalline CdTe solar cells fabricated in the lab (and commercial modules of over 18 % efficiency)[69]. Cathodoluminescence and Secondary ion mass spectroscopy experiments tracing the Se diffusion profile in CdTe bulk reported a long-range diffusion of Se along the grain boundaries and deep into CdTe grains[86].

The first question that we dealt with was to suggest a diffusion mechanism of Se in CdTe bulk. We using our DFT-based calculations of the electronic structure of point defects, suggested Te self-interstitial and Se-split interstitial as the defects responsible for Te and Se atomic diffusion in the CdTe bulk. We then, through nudged elastic band calculations, identified the diffusion trajectories that can explain the long-range diffusion of chalcogenide Se and Te atoms in the CdTe bulk. A combination of translation and rotation of split-interstitial defects were outlined to explain the diffusion of both the chalcogenides. The values calculated for diffusion energy barriers for both elements were lower than 0.45 eV, these small values explain the long-range diffusion of the Se as observed in the experiments. Another important deduction that we made from diffusion energy barrier calculations is that the presence of Se in CdTe, moderates the otherwise fast Te self-diffusion in the CdTe lattice.

The next question that we addressed was the reported reduction of 60 - 80 % in the non-radiative recombination activity (defects) in both grain boundaries and CdTe interior grain on alloying with Se[6]. In previous DFT calculations, Te-antisite Te_{Cd} and Cd-vacancy V_{Cd} were predicted to have non-radiative recombination character responsible for carrier trap and reducing the photo-voltaic efficiency of CdTe[72,103]. Through the means of electronic structure calculations, we revisited and pointed to the respective electron capture and hole capture characteristic of V_{Cd} and Te_{Cd} critical intrinsic defects, resulting from the presence of defect electronic states in the semiconductor band gap.

We demonstrated, using the defect association calculation of Se diffusing defect with the V_{Cd} and Te_{Cd} defects and the resulting defect complexes formation energies, that these critical defects can be passivated on interaction with Se in the CdTe grain. The interaction of diffusing Se interstitial with the two critical defects in CdTe obliterates their dangling bonds. The defect complexes resulting from such interaction were identified to have a low formation energy and predicted to have low carrier capture rates as the corresponding defect states were calculated to be present close to band edges or in the semiconductor electronic bands.

Summarizing these points, we conclude that the role of Se in the context of defect passivation of critical defects in the CdTe grain is a hybrid one. Firstly, Se moderates

the fast and linear diffusion of Te, promoting isotropic diffusion of both chalcogenides inside the volume of CdTe grain, and secondly, passivation of critical Cd-vacancies and Te anti-sites defects through Se alloying at the Te-substitution site in the first shell of the Cd-site related defects (Cd-vacancy, Te-antisite, chalcogenide dimer). We have published the results from this study in Appl. Phys. Lett. **119**, 062105 (2021).

Our study on the role of Se in CdTe solar cells provides a comprehensive explanation of the atomistic mechanism behind the passivation of critical defects in Se alloyed CdTe absorbers and should allow further improvements alongside with other doping strategies to push efficiencies in the range of 25 % in the coming years. In this study of Se-related defects in CdTe, we have only considered the interaction of Se with major native defects present in Te-rich conditions. However, along with Se alloying of CdTe, treatment with $CdCl_2$ that promotes Cl dopant segregation into CdTe grain is reported to be also responsible for the record-performing CdTe polycrystalline solar cells. In the future, the first principle based calculations focusing on the study of defect complexes to explore the impact of co-doping of Cl and Se in CdTe can provide further insight into the defect physics of CdTe solar cells and future growth strategies. Also, the investigation of Se interaction with dopants introduced for improving hole concentration in CdTe, such as conventional dopant Cu and more recently used dopants As, P, and Sb, could provide direction for further improvements.

The second problem that we addressed was related to quantum applications. Here (**Chapter 5**), we focused on the study of the ground-state electronic structure of solitary transition metal (TM) Mn and Cr dopants in the CdTe host and their interaction with native defects. The aim of this study was to provide an explanation for our collaborators' observation of a low number of quantum dots (QDs) with the correct single dopant configuration for the Cr atom compared to Mn-doped CdTe/ZnTe QDs in photoluminescence (PL) experiments, grown by the same approach. The concentration and character of the solitary impurity can be strongly influenced by the presence of native defects in the host. Therefore, we carried out a detailed analysis of impurities interaction with native defects to explain the difference between the Cr and Mn-doped CdTe solotronics systems.

In the first part, we defined the charge and spin ground state of Cr and Mn dopants in the CdTe host and the defect electronic levels resulting in the host band structure due to the impurities. We highlighted a one-to-one correspondence between the calculated respective rD_{2d} and T_d symmetry of Cr and Mn dopants, with the experimental EPR results, crystal field theory based Jahn-Teller distortion model, and electronic wavefunction of the Kohn-Sham states of the TM d-orbitals derived defect electronic levels

calculated using DFT.

In the second part, we studied the interaction of TM impurities with the CdTe native defects in both Te-rich and Cd-rich growth limits. This comparison allowed the study of defect complexes that can form under different growth strategies. Through the calculation of binding energies associated with defect complexes formation, we explored the possibility of deviation of the Cr and Mn impurities from their ground state configuration, brought by interaction with native defects.

The calculated binding energies suggested a strong interaction of Cr with all the native defects present in CdTe in both Cd-rich limits and Te-rich limits, except for the Te-vacancy. In particular, high binding energy values of 0.65 eV of Cr with Cd-vacancy and 0.45 eV of Cr with Cd-antisite defect, corresponding to Te-rich and Cd-rich conditions, pointed to a strong interaction. In contrast, binding energies corresponding to Mn interaction with native defects pointed to weak binding or no interaction (with values less than 0.1 eV), except for Cd-interstitial (with a binding energy of 0.23 eV). We propose that the high binding energy values calculated in the case of Cr interaction with the native defects in both Te-rich and Cd-rich conditions could explain the low number of single Cr-doped QDs presenting isolated Cr atom ground state in PL experiments.

The next experimental observation that we were able to provide reasoning for was the Cr+ - hole complex nano-magnet detected in CdTe QDs, through photoluminescence (PL) experiments. This configuration was reported to result from the change of the +2 oxidation ground state to a +1 oxidation state. However, the experimental results did not provide an explanation for the source of the doping or the extra electron. In the final part of this study, we provided a comprehensive explanation of the possible source of the electron donated to the Cr solitary dopant from the CdTe surrounding matrix. Based on the electronic structure calculations, we proposed that it is quite probable that the Cr+ - hole complex observed in the experiment results from the charge transfer of an electron from Cd-antisite to Cr impurity. This final part of the study was presented in the publication, Phys. Rev. B **104**, L041301 (2021), with our experimental collaborators.

Our work on solitary dopants in CdTe points to the fact that interaction of dopants with the native defects could be really challenging for the fabrication of such systems. In parallel, such interactions could also provide new defect systems with unique functionalities, such as observed in the case of Cr^{+}-hole nanomagnet. Therefore careful investigation of such interactions with DFT calculations could prove useful insight for growth strategies. We suggest the possibility of such interactions should not be overlooked while designing growth strategies. In future work related to Cr and Mn solitary dopants in CdTe, a practical next step for DFT-based calculations could be to define

the migration process of dopants from the CdTe surface to the bulk region. Another possible direction is to study the dopant defect system using a cluster approach with QM/MM approach, with the QM region defined with higher accuracy hybrid exchange-correlation functional that could provide a more accurate description of the system.

In conclusion, the work presented in this thesis showed that the first principle based calculations could provide a good qualitative description and help in the explanation of experimentally observed phenomena and devising growth strategies for semiconductor-based devices. The results were interpreted in a manner that they can be applied to future engineering of semiconductor devices and experimental setup of the related systems.

References

[1] Riordan, M.; Hoddeson, L.; Herring, C. In *More Things in Heaven and Earth: A Celebration of Physics at the Millennium*; Bederson, B., Ed.; Springer New York: New York, NY, 1999; pp 563–578.

[2] McCluskey, M. D.; Haller, E. E. *Dopants and defects in semiconductors*; CRC press, 2018.

[3] Agrinskay, N. V.; Arkadeva, E. N. Fermi Level Pinning in the Middle of the Band Gap in CdTe:Cl Crystals-Role of Deep Localized States. *physica status solidi (b)* **1987**, *143*, K103–K106.

[4] Yang, J.-H.; Park, J.-S.; Kang, J.; Metzger, W.; Barnes, T.; Wei, S.-H. Tuning the Fermi level beyond the equilibrium doping limit through quenching: The case of CdTe. *Phys. Rev. B* **2014**, *90*, 245202.

[5] Paudel, N. R.; Yan, Y. Enhancing the photo-currents of CdTe thin-film solar cells in both short and long wavelength regions. *Applied Physics Letters* **2014**, *105*, 183510.

[6] Fiducia, T. The effects of chlorine and selenium in cadmium telluride solar cells. **2021**,

[7] Koenraad, P. M.; Flatté, M. E. Single dopants in semiconductors. *Nature materials* **2011**, *10*, 91–100.

[8] Bassett, L. C.; Alkauskas, A.; Exarhos, A. L.; Fu, K.-M. C. Quantum defects by design. *Nanophotonics* **2019**, *8*, 1867–1888.

[9] Kobak, J.; Smoleński, T.; Goryca, M.; Papaj, M.; Gietka, K.; Bogucki, A.; Koperski, M.; Rousset, J.-G.; Suffczyński, J.; Janik, E., et al. Designing quantum dots for solotronics. *Nature communications* **2014**, *5*, 1–8.

[10] Besombes, L.; Léger, Y.; Maingault, L.; Ferrand, D.; Mariette, H.; Cibert, J. Probing the Spin State of a Single Magnetic Ion in an Individual Quantum Dot. *Phys. Rev. Lett.* **2004**, *93*, 207403.

[11] Besombes, L.; Léger, Y.; Maingault, L.; Ferrand, D.; Bougerol, C.; Mariette, H.; Cibert, J. Optical properties of manganese-doped individual CdTe quantum dots. *ACTA PHYSICA POLONICA SERIES A* **2005**, *108*, 527.

[12] Besombes, L.; Boukari, H.; Tiwari, V.; Lafuente-Sampietro, A.; Kuroda, S.; Makita, K. Optical control of an individual Cr spin in a semiconductor quantum dot. *Semiconductor Science and Technology* **2019**, *34*, 063001.

[13] Kudelski, A.; Lemaitre, A.; Miard, A.; Voisin, P.; Graham, T.; Warburton, R.; Krebs, O. Optically probing the fine structure of a single Mn atom in an InAs quantum dot. *Physical review letters* **2007**, *99*, 247209.

[14] Bathen, M.; Lew, C.-K.; Woerle, J.; Dorfer, C.; Grossner, U.; Castelletto, S.; Johnson, B. Characterization methods for defects and devices in silicon carbide. *Journal of Applied Physics* **2022**, *131*, 140903.

[15] De Souza, R.; Martin, M. Secondary ion mass spectrometry: A powerful tool for diffusion studies in solids. *Archives of Metallurgy and Materials* **2004**, *49*, 431–446.

[16] Broberg, D. P. *Point Defect Engineering of Energy Materials from First-Principles Calculations*; University of California, Berkeley, 2019.

[17] Shockley, W.; Read, W. T. Statistics of the Recombinations of Holes and Electrons. *Phys. Rev.* **1952**, *87*, 835–842.

[18] Hall, R. N. Electron-Hole Recombination in Germanium. *Phys. Rev.* **1952**, *87*, 387–387.

[19] Frodason, Y.; Johansen, K.; Bjørheim, T.; Svensson, B.; Alkauskas, A. Zn vacancy as a polaronic hole trap in ZnO. *Physical Review B* **2017**, *95*, 094105.

[20] Pampili, P.; Parbrook, P. J. Doping of III-nitride materials. *Materials Science in Semiconductor Processing* **2017**, *62*, 180–191.

[21] Orellana, W.; Menéndez-Proupin, E.; Flores, M. A. Self-compensation in chlorine-doped CdTe. *Scientific Reports* **2019**, *9*, 9194.

[22] Van de Walle, C. G.; Neugebauer, J. First-principles calculations for defects and impurities: Applications to III-nitrides. *Journal of applied physics* **2004**, *95*, 3851–3879.

[23] Pohl, R. Electron conductivity and photochemical processes in alkali-halide crystals. *Proceedings of the Physical Society* **1937**, *49*, 3.

[24] Watkins, G. D. Electron paramagnetic resonance of point defects in solids, with emphasis on semiconductors. *Point Defects in Solids: Volume 2 Semiconductors and Molecular Crystals* **1975**, 333–392.

[25] Lang, D. Deep-level transient spectroscopy: A new method to characterize traps in semiconductors. *Journal of applied physics* **1974**, *45*, 3023–3032.

[26] Born, M.; Oppenheimer, R. Zur Quantentheorie der Molekeln. *Annalen der Physik* **1927**, *389*, 457–484.

[27] Hohenberg, P.; Kohn, W. Inhomogeneous electron gas. *Physical review* **1964**, *136*, B864.

[28] Kohn, W.; Sham, L. J. Self-consistent equations including exchange and correlation effects. *Physical review* **1965**, *140*, A1133.

[29] Von Barth, U.; Hedin, L. A local exchange-correlation potential for the spin polarized case. i. *Journal of Physics C: Solid State Physics* **1972**, *5*, 1629.

[30] Langreth, D. C.; Mehl, M. Beyond the local-density approximation in calculations of ground-state electronic properties. *Physical Review B* **1983**, *28*, 1809.

[31] Perdew, J. P. Accurate density functional for the energy: Real-space cutoff of the gradient expansion for the exchange hole. *Physical Review Letters* **1985**, *55*, 1665.

[32] Perdew, J. P.; Burke, K.; Ernzerhof, M. Generalized Gradient Approximation Made Simple. *Phys. Rev. Lett.* **1996**, *77*, 3865–3868.

[33] Adamo, C.; Barone, V. Toward reliable density functional methods without adjustable parameters: The PBE0 model. *The Journal of Chemical Physics* **1999**, *110*, 6158–6170.

[34] Payne, M. C.; Teter, M. P.; Allan, D. C.; Arias, T.; Joannopoulos, a. J. Iterative minimization techniques for ab initio total-energy calculations: molecular dynamics and conjugate gradients. *Reviews of modern physics* **1992**, *64*, 1045.

[35] Schwerdtfeger, P. The pseudopotential approximation in electronic structure theory. *ChemPhysChem* **2011**, *12*, 3143–3155.

[36] Hartwigsen, C.; Goedecker, S.; Hutter, J. Relativistic separable dual-space Gaussian pseudopotentials from H to Rn. *Phys. Rev. B* **1998**, *58*, 3641–3662.

[37] Bitzek, E.; Koskinen, P.; Gähler, F.; Moseler, M.; Gumbsch, P. Structural Relaxation Made Simple. *Phys. Rev. Lett.* **2006**, *97*, 170201.

[38] Zhang, S.; Northrup, J. E. Chemical potential dependence of defect formation energies in GaAs: Application to Ga self-diffusion. *Physical review letters* **1991**, *67*, 2339.

[39] Baraff, G.; Schlüter, M. Electronic structure, total energies, and abundances of the elementary point defects in GaAs. *Physical review letters* **1985**, *55*, 1327.

[40] Freysoldt, C.; Grabowski, B.; Hickel, T.; Neugebauer, J.; Kresse, G.; Janotti, A.; Van de Walle, C. G. First-principles calculations for point defects in solids. *Rev. Mod. Phys.* **2014**, *86*, 253–305.

[41] Lany, S.; Zunger, A. Assessment of correction methods for the band-gap problem and for finite-size effects in supercell defect calculations: Case studies for ZnO and GaAs. *Physical Review B* **2008**, *78*, 235104.

[42] Anderson, P. Model for the electronic structure of amorphous semiconductors. *Physical Review Letters* **1975**, *34*, 953.

[43] Vineyard, G. H. Frequency factors and isotope effects in solid state rate processes. *Journal of Physics and Chemistry of Solids* **1957**, *3*, 121–127.

[44] Henkelman, G.; Uberuaga, B. P.; Jónsson, H. A climbing image nudged elastic band method for finding saddle points and minimum energy paths. *The Journal of Chemical Physics* **2000**, *113*, 9901–9904.

[45] Henkelman, G.; Jónsson, H. Improved tangent estimate in the nudged elastic band method for finding minimum energy paths and saddle points. *The Journal of chemical physics* **2000**, *113*, 9978–9985.

[46] Pulay, P. Convergence acceleration of iterative sequences. the case of scf iteration. *Chemical Physics Letters* **1980**, *73*, 393–398.

[47] Jahn, H. A.; Teller, E. Stability of polyatomic molecules in degenerate electronic states-I—Orbital degeneracy. *Proceedings of the Royal Society of London. Series A-Mathematical and Physical Sciences* **1937**, *161*, 220–235.

[48] Coulson, C. A.; Kearsley, M. J. Colour centres in irradiated diamonds. I. *Proceedings of the Royal Society of London. Series A. Mathematical and Physical Sciences* **1957**, *241*, 433–454.

[49] Segall, B.; Lorenz, M. R.; Halsted, R. E. Electrical Properties of *n*-Type CdTe. *Phys. Rev.* **1963**, *129*, 2471–2481.

[50] Marfaing, Y. Impurity doping and compensation mechanisms in CdTe. *Thin Solid Films* **2001**, *387*, 123–128, Proceeedings of Symposium N on Thin Film Photovoltaicmaterials of the E-MRS Spring Conference.

[51] Fulop, G.; Doty, M.; Meyers, P.; Betz, J.; Liu, C. H. High-efficiency electrodeposited cadmium telluride solar cells. *Applied Physics Letters* **1982**, *40*, 327–328.

[52] Chu, T. Thin film cadmium telluride solar cells by two chemical vapor deposition techniques. *Solar Cells* **1988**, *23*, 31–48, Special Issue on Cadmium Telluride.

[53] Britt, J.; Ferekides, C. Thin-film CdS/CdTe solar cell with 15.8% efficiency. *Applied Physics Letters* **1993**, *62*, 2851–2852.

[54] Bonnet, D.; Meyers, P. Cadmium-telluride—Material for thin film solar cells. *Journal of Materials Research* **1998**, *13*, 2740–2753.

[55] Fiederle, M.; Ebling, D.; Eiche, C.; Hofmann, D.; Salk, M.; Stadler, W.; Benz, K.; Meyer, B. Comparison of CdTe, Cd0.9Zn0.1Te and CdTe0.9Se0.1 crystals: application for - and X-ray detectors. *Journal of Crystal Growth* **1994**, *138*, 529–533.

[56] Bradford Barber, H. Applications of semiconductor detectors to nuclear medicine. *Nuclear Instruments and Methods in Physics Research Section A: Accelerators, Spectrometers, Detectors and Associated Equipment* **1999**, *436*, 102–110.

[57] Schlesinger, T.; Toney, J.; Yoon, H.; Lee, E.; Brunett, B.; Franks, L.; James, R. Cadmium zinc telluride and its use as a nuclear radiation detector material. *Materials Science and Engineering: R: Reports* **2001**, *32*, 103–189.

[58] Józwikowska, A.; Józwikowski, K.; Rogalski, A. Performance of mercury cadmium telluride photoconductive detectors. *Infrared Physics* **1991**, *31*, 543–554.

[59] Gravrand, O.; Rothman, J.; Cervera, C.; Baier, N.; Lobre, C.; Zanatta, J. P.; Boulade, O.; Moreau, V.; Fieque, B. HgCdTe Detectors for Space and Science Imaging: General Issues and Latest Achievements. *Journal of Electronic Materials* **2016**, *45*, 4532–4541.

[60] Pidancier, P.; Delannoy, A.; Madet, K.; Chorier, P.; Remoué, N.; Dartois, T. Sofradir detectors for MTG FCI application. **2017**, *10563*, 105631V.

[61] Bordonne, M.; Chawki, M. B.; Marie, P.-Y.; Zaragori, T.; Roch, V.; Grignon, R.; Imbert, L.; Verger, A. High-quality brain perfusion SPECT images may be achieved with a high-speed recording using 360° CZT camera. *EJNMMI Physics* **2020**, *7*, 65.

[62] Henzlova, M. J.; Duvall, L. Is the CZT technology the future of nuclear cardiology? *Journal of Nuclear Cardiology* **2022**, *29*, 737–740.

[63] Munshi, A. H.; Sasidharan, N.; Pinkayan, S.; Barth, K. L.; Sampath, W.; Ongsakul, W. Thin-film CdTe photovoltaics – The technology for utility scale sustainable energy generation. *Solar Energy* **2018**, *173*, 511–516.

[64] Shockley, W.; Queisser, H. J. Detailed Balance Limit of Efficiency of p-n Junction Solar Cells. *Journal of Applied Physics* **1961**, *32*, 510–519.

[65] Rühle, S. Tabulated values of the Shockley–Queisser limit for single junction solar cells. *Solar Energy* **2016**, *130*, 139 – 147.

[66] Chu, T. L.; Chu, S. S. Thin film II–VI photovoltaics. *Solid-State Electronics* **1995**, *38*, 533–549.

[67] Arkhipov, V.; Poortmans, J. *Thin Film Solar Cells: Fabrication, Characterization and Applications*; Wiley, 2007.

[68] Bai, Z.; Yang, J.; Wang, D. Thin film CdTe solar cells with an absorber layer thickness in micro- and sub-micrometer scale. *Applied Physics Letters* **2011**, *99*, 143502.

[69] Green, M. A.; Hishikawa, Y.; Dunlop, E. D.; Levi, D. H.; Hohl-Ebinger, J.; Ho-Baillie, A. W. Solar cell efficiency tables (version 51). *Progress in Photovoltaics: Research and Applications* **2018**, *26*, 3–12.

[70] Wilson, G. M. et al. The 2020 photovoltaic technologies roadmap. *Journal of Physics D: Applied Physics* **2020**, *53*, 493001.

[71] Kirchartz, T. High open-circuit voltages in lead-halide perovskite solar cells: experiment, theory and open questions. *Philosophical Transactions of the Royal Society A: Mathematical, Physical and Engineering Sciences* **2019**, *377*, 20180286.

[72] Yang, J.-H.; Yin, W.-J.; Park, J.-S.; Ma, J.; Wei, S.-H. Review on first-principles study of defect properties of CdTe as a solar cell absorber. *Semiconductor Science and Technology* **2016**, *31*, 083002.

[73] Sites, J.; Pan, J. Strategies to increase CdTe solar-cell voltage. *Thin Solid Films* **2007**, *515*, 6099–6102, Proceedings of Sympodium O on Thin Film Chalcogenide Photovoltaic Materials, EMRS 2006 Conference.

[74] Kanevce, A.; Gessert, T. A. Optimizing CdTe Solar Cell Performance: Impact of Variations in Minority-Carrier Lifetime and Carrier Density Profile. *IEEE Journal of Photovoltaics* **2011**, *1*, 99–103.

[75] Kanevce, A.; Reese, M. O.; Barnes, T. M.; Jensen, S. A.; Metzger, W. K. The roles of carrier concentration and interface, bulk, and grain-boundary recombination for 25% efficient CdTe solar cells. *Journal of Applied Physics* **2017**, *121*, 214506.

[76] Rein, S.; Rehrl, T.; Warta, W.; Glunz, S. W. Lifetime spectroscopy for defect characterization: Systematic analysis of the possibilities and restrictions. *Journal of Applied Physics* **2002**, *91*, 2059–2070.

[77] Bridge, C. J.; Dawson, P.; Buckle, P. D.; Özsan, M. E. Photoluminescence spectroscopy and decay time measurements of polycrystalline thin film CdTe/CdS solar cells. *Journal of Applied Physics* **2000**, *88*, 6451–6456.

[78] Swanson, D.; Sites, J.; Sampath, W. Co-sublimation of CdSexTe1-x layers for CdTe solar cells. *Solar Energy Materials and Solar Cells* **2017**, *159*.

[79] Poplawsky, J. D.; Guo, W.; Paudel, N.; Ng, A.; More, K.; Leonard, D.; Yan, Y. Structural and compositional dependence of the CdTexSe1-x alloy layer photoactivity in CdTe-based solar cells. *Nature Communications* **2016**, *7*, 12537.

[80] Munshi, A. H.; Kephart, J.; Abbas, A.; Raguse, J.; Beaudry, J.; Barth, K.; Sites, J.; Walls, J.; Sampath, W. Polycrystalline CdSeTe/CdTe Absorber Cells With 28 mA/cm2 Short-Circuit Current. *IEEE Journal of Photovoltaics* **2018**, *8*, 310–314.

[81] Green, M. A.; Emery, K.; Hishikawa, Y.; Warta, W.; Dunlop, E. D. Solar cell efficiency tables (version 40). *Progress in Photovoltaics: Research and Applications* **2012**, *20*, 606–614.

[82] Green, M. A.; Emery, K.; Hishikawa, Y.; Warta, W.; Dunlop, E. D. Solar cell efficiency tables (version 46). *Progress in Photovoltaics: Research and Applications* **2015**, *23*, 805–812.

[83] Zheng, X.; Kuciauskas, D.; Moseley, J.; Colegrove, E.; Albin, D. S.; Moutinho, H.; Duenow, J. N.; Ablekim, T.; Harvey, S. P.; Ferguson, A.; Metzger, W. K. Recombination and bandgap engineering in CdSeTe/CdTe solar cells. *APL Materials* **2019**, *7*, 071112.

[84] Yang, J.; Wei, S.-H. First-principles study of the band gap tuning and doping control in CdSe x Te1-x alloy for high efficiency solar cell. *Chinese Physics B* **2019**, *28*, 086106.

[85] Watts, M. J.; Fiducia, T. A. M.; Sanyal, B.; Smith, R.; Walls, J. M.; Goddard, P. Enhancement of photovoltaic efficiency in CdSe x Te1-x (where $0 \leqslant x \leqslant 1$):

insights from density functional theory. *Journal of Physics: Condensed Matter* **2019**, *32*, 125702.

[86] Fiducia, T. A. M.; Mendis, B. G.; Li, K.; Grovenor, C. R. M.; Munshi, A. H.; Barth, K.; Sampath, W. S.; Wright, L. D.; Abbas, A.; Bowers, J. W.; Walls, J. M. Understanding the role of selenium in defect passivation for highly efficient selenium-alloyed cadmium telluride solar cells. *Nature Energy* **2019**, *4*, 504–511.

[87] Fiederle, M.; Feltgen, T.; Meinhardt, J.; Rogalla, M.; Benz, K. State of the art of (Cd,Zn)Te as gamma detector. *Journal of Crystal Growth* **1999**, *197*, 635–640.

[88] Gul, R.; Bolotnikov, A.; Kim, H. K.; Rodriguez, R.; Keeter, K.; Li, Z.; Gu, G.; James, R. B. Point Defects in CdZnTe Crystals Grown by Different Techniques. *Journal of Electronic Materials* **2011**, *40*, 274–279.

[89] Lindström, A.; Mirbt, S.; Sanyal, B.; Klintenberg, M. High resistivity in undoped CdTe: carrier compensation of Te antisites and Cd vacancies. *Journal of Physics D: Applied Physics* **2015**, *49*, 035101.

[90] Li, C.; Hao, X.; He, Y.; Zhang, J.; Wu, L.; Li, W.; Wang, W.; Feng, L.; Monirul, I. M.; Akimoto, K.; Sakurai, T. Identification of deep level defects in CdTe solar cells using transient photo-capacitance spectroscopy. *Japanese Journal of Applied Physics* **2020**, *60*, SBBF01.

[91] Guo, J.; Mannodi-Kanakkithodi, A.; Sen, F. G.; Schwenker, E.; Barnard, E. S.; Munshi, A.; Sampath, W.; Chan, M. K. Y.; Klie, R. F. Effect of selenium and chlorine co-passivation in polycrystalline CdSeTe devices. *Applied Physics Letters* **2019**, *115*, 153901.

[92] Ablekim, T.; Duenow, J. N.; Zheng, X.; Moutinho, H.; Moseley, J.; Perkins, C. L.; Johnston, S. W.; O'Keefe, P.; Colegrove, E.; Albin, D. S.; Reese, M. O.; Metzger, W. K. Thin-Film Solar Cells with 19% Efficiency by Thermal Evaporation of CdSe and CdTe. *ACS Energy Letters* **2020**, *5*, 892–896.

[93] Mohr, S.; Ratcliff, L. E.; Genovese, L.; Caliste, D.; Boulanger, P.; Goedecker, S.; Deutsch, T. Accurate and efficient linear scaling DFT calculations with universal applicability. *Phys. Chem. Chem. Phys.* **2015**, *17*, 31360–31370.

[94] Genovese, L.; Videau, B.; Ospici, M.; Deutsch, T.; Goedecker, S.; Méhaut, J.-F. Daubechies wavelets for high performance electronic structure calculations: The BigDFT project. *Comptes Rendus Mécanique* **2011**, *339*, 149–164, High Performance Computing.

[95] von Barth, U.; Hedin, L. A local exchange-correlation potential for the spin polarized case. i. *Journal of Physics C: Solid State Physics* **1972**, *5*, 1629–1642.

[96] Strauss, A.J., The physical properties of cadmium telluride. *Rev. Phys. Appl. (Paris)* **1977**, *12*, 167–184.

[97] Elber, R.; Karplus, M. A method for determining reaction paths in large molecules: Application to myoglobin. *Chemical Physics Letters* **1987**, *139*, 375–380.

[98] Szeles, C.; Shan, Y. Y.; Lynn, K. G.; Moodenbaugh, A. R.; Eissler, E. E. Trapping properties of cadmium vacancies in $Cd_{1-x}Zn_xTe$. *Phys. Rev. B* **1997**, *55*, 6945–6949.

[99] Flores, M. A.; Orellana, W.; Menéndez-Proupin, E. First-principles DFT+GW study of the Te antisite in CdTe. *Computational Materials Science* **2016**, *125*, 176–182.

[100] Yang, J.-H.; Shi, L.; Wang, L.-W.; Wei, S.-H. Non-Radiative Carrier Recombination Enhanced by Two-Level Process: A First-Principles Study. *Scientific Reports* **2016**, *6*, 2045–2322.

[101] Wei, S.-H.; Zhang, S. B. Chemical trends of defect formation and doping limit in II-VI semiconductors: The case of CdTe. *Phys. Rev. B* **2002**, *66*, 155211.

[102] Krasikov, D. N.; Scherbinin, A. V.; Knizhnik, A. A.; Vasiliev, A. N.; Potapkin, B. V.; Sommerer, T. J. Theoretical analysis of non-radiative multiphonon recombination activity of intrinsic defects in CdTe. *Journal of Applied Physics* **2016**, *119*, 085706.

[103] Kavanagh, S. R.; Walsh, A.; Scanlon, D. O. Rapid Recombination by Cadmium Vacancies in CdTe. *ACS Energy Letters* **2021**, *6*, 1392–1398.

[104] Roehl, J.; Khare, S. Diffusion of Te vacancy and interstitials of Te, Cl, O, S, P and Sb in CdTe: A density functional theory study. *Solar Energy Materials and Solar Cells* **2014**, *128*, 343–350.

[105] Ma, J.; Yang, J.; Wei, S.-H.; Da Silva, J. L. F. Correlation between the electronic structures and diffusion paths of interstitial defects in semiconductors: The case of CdTe. *Phys. Rev. B* **2014**, *90*, 155208.

[106] Lordi, V. Point defects in Cd(Zn)Te and TlBr: Theory. *Journal of Crystal Growth* **2013**, *379*, 84–92, Compound Semiconductors and Scintillators for Radiation Detection Applications: A Special Tribute to the Research of Michael Schieber.

[107] Watkins, G. D. EPR of defects in semiconductors: Past, present, future. *Physics of the Solid State* **1999**, *41*, 746–750.

[108] Carvalho, A.; Tagantsev, A. K.; Öberg, S.; Briddon, P. R.; Setter, N. Cation-site intrinsic defects in Zn-doped CdTe. *Phys. Rev. B* **2010**, *81*, 075215.

[109] Watkins, G. Intrinsic defects in II–VI semiconductors. *Journal of Crystal Growth* **1996**, *159*, 338–344, Proceedings of the seventh international conference on II-VI compouds and devices.

[110] Shepidchenko, A.; Sanyal, B.; Klintenberg, M.; Mirbt, S. Small hole polaron in CdTe: Cd-vacancy revisited. *Scientific Reports* **2015**, *5*, 14509.

[111] Becerril, M.; Zelaya-Angel, O.; Vargas-García, J.; Ramírez-Bon, R.; González-Hernández, J. Effects of Cd vacancies on the electrical properties of polycrystalline CdTe sputtered films. *Journal of Physics and Chemistry of Solids* **2001**, *62*, 1081–1085.

[112] Scholz, K.; Stiens, H.; Müller-Vogt, G. Investigations on the effect of contacts on p-type CdTe DLTS-measurements. *Journal of Crystal Growth* **1999**, *197*, 586–592.

[113] Clouet, E.; Varvenne, C.; Jourdan, T. Elastic modeling of point-defects and their interaction. *Computational Materials Science* **2018**, *147*, 49–63.

[114] Du, M.-H.; Takenaka, H.; Singh, D. J. Native defects and oxygen and hydrogen-related defect complexes in CdTe: Density functional calculations. *Journal of Applied Physics* **2008**, *104*, 093521.

[115] Du, M.-H. What causes high resistivity in CdTe. *New Journal of Physics* **Jun 2012**, 063020, INSTRUMENTATION RELATED TO NUCLEAR SCIENCE AND TECHNOLOGY.

[116] Lindström, A.; Mirbt, S.; Sanyal, B.; Håkansson, A.; Klintenberg, M. Tailoring of defect levels by deformations: Te-antisite in CdTe. *Journal of physics. Condensed matter : an Institute of Physics journal* **2013**, *25*, 415801.

[117] Du, M.-H.; Takenaka, H.; Singh, D. J. Carrier compensation in semi-insulating CdTe: First-principles calculations. *Phys. Rev. B* **2008**, *77*, 094122.

[118] Davis, C. B.; Allred, D. D.; Reyes-Mena, A.; González-Hernández, J.; González, O.; Hess, B. C.; Allred, W. P. Photoluminescence and absorption studies of defects in CdTe and $Zn_xCd_{1-x}Te$ crystals. *Phys. Rev. B* **1993**, *47*, 13363–13369.

[119] Gessert, T.; Wei, S.-H.; Ma, J.; Albin, D.; Dhere, R.; Duenow, J.; Kuciauskas, D.; Kanevce, A.; Barnes, T.; Burst, J.; Rance, W.; Reese, M.; Moutinho, H. Research strategies toward improving thin-film CdTe photovoltaic devices beyond 20% conversion efficiency. *Solar Energy Materials and Solar Cells* **2013**, *119*, 149–155, Thin-film Photovoltaic Solar Cells.

[120] Kuciauskas, D.; Krasikov, D. Spectroscopic and Microscopic Defect and Carrier-Lifetime Analysis in Cadmium Telluride. *IEEE Journal of Photovoltaics* **2018**, *8*, 1754–1760.

[121] Yang, J.-H.; Park, J.-S.; Kang, J.; Wei, S.-H. First-principles multiple-barrier diffusion theory: The case study of interstitial diffusion in CdTe. *Phys. Rev. B* **2015**, *91*, 075202.

[122] Colegrove, E.; Zheng, X.; Ablekim, T.; Duenow, J. N.; Perkins, C. L.; Moutinho, H. R.; Metzger, W. K. Se diffusion in CdTe thin films for photovoltaics. *Journal of Physics D: Applied Physics* **2020**, *54*, 025501.

[123] James, R. B. et al. Material properties of large-volume cadmium zinc telluride crystals and their relationship to nuclear detector performance. *Journal of Electronic Materials* **1998**, *27*, 788–799.

[124] Consonni, V.; Baier, N.; Renet, S.; Brambilla, A.; Feuillet, G. Compensation and defect passivation processes in polycrystalline CdTe: Cl layers. *physica status solidi c* **2006**, *3*, 807–811.

[125] Alkauskas, A.; Broqvist, P.; Pasquarello, A. Defect Energy Levels in Density Functional Calculations: Alignment and Band Gap Problem. *Phys. Rev. Lett.* **2008**, *101*, 046405.

[126] Munshi, A. H.; Kephart, J. M.; Abbas, A.; Danielson, A.; Glinas, G.; Beaudry, J.-N.; Barth, K. L.; Walls, J. M.; Sampath, W. S. Effect of CdCl2 passivation treatment on microstructure and performance of CdSeTe/CdTe thin-film photovoltaic devices. *Solar Energy Materials and Solar Cells* **2018**, *186*, 259–265.

[127] Paul, S.; Sohal, S.; Swartz, C.; Li, D.-B.; Bista, S. S.; Grice, C. R.; Yan, Y.; Holtz, M.; Li, J. V. Effects of post-deposition CdCl2 annealing on electronic properties of CdTe solar cells. *Solar Energy* **2020**, *211*, 938–948.

[128] Romeo, A.; Artegiani, E. CdTe-Based Thin Film Solar Cells: Past, Present and Future. *Energies* **2021**, *14*.

[129] Vogl, P. In *Festkörperprobleme 25: 5th General Conference of the Condensed Matter Division (CMD) 18…22 March 1985, Technische Universität Berlin*

(West) Plenary Lectures and Lectures held at the Symposia Sections of the CMD: Liquids Low Temperature Macromolecular Physics Magnetism Metals Semiconductors and Insulators Surfaces and Interfaces; Grosse, P., Ed.; Springer Berlin Heidelberg: Berlin, Heidelberg, 1985; pp 563–571.

[130] Kreissl, J.; Schulz, H.-J. Transition-metal impurities in II–VI semiconductors: characterization and switching of charge states. *Journal of Crystal Growth* **1996**, *161*, 239–249, Purification, Doping and Defects in II-VI Materials.

[131] Schulz, H.-J. Transition metal impurities in compound semiconductors: Experimental situation. *Materials Chemistry and Physics* **1987**, *16*, 373–384.

[132] Delerue, C.; Lannoo, M.; Allan, G. New theoretical approach of transition-metal impurities in semiconductors. *Phys. Rev. B* **1989**, *39*, 1669–1681.

[133] Tersoff, J.; Harrison, W. A. Transition-Metal Impurities in Semiconductors—Their Connection with Band Lineups and Schottky Barriers. *Phys. Rev. Lett.* **1987**, *58*, 2367–2370.

[134] Tian, Z.; Shen, X. Defect-molecule model calculations of 3d transition metal ions in II-VI semiconductors. *Journal of Applied Physics* **1989**, *66*, 2414–2419.

[135] Lechner, H.; Hofmann, D.; Meyer, B.; Azoulay, M.; Krambrock, K.; Spaeth, J.-M.; Döornen, A.; Kaufmann, B.; Omling, P.; Salk, M., et al. Electrical and optical properties of the transition metal iron in ZnTe and CdTe. *Advanced Materials for Optics and Electronics* **1994**, *3*, 223–232.

[136] Fleurov, V. N.; Kikoin, K. A. *Transition Metal Impurities in Semiconductors*; WORLD SCIENTIFIC, 1994.

[137] Lu, L.; Xia, X.; Luo, J. K.; Shao, G. Mn-doped TiO2 thin films with significantly improved optical and electrical properties. *Journal of Physics D: Applied Physics* **2012**, *45*, 485102.

[138] Wang, C.; Chen, Z.; Jin, H.; Cao, C.; Li, J.; Mi, Z. Enhancing visible-light photoelectrochemical water splitting through transition-metal doped TiO2 nanorod arrays. *J. Mater. Chem. A* **2014**, *2*, 17820–17827.

[139] Martinez, A.; Martyshkin, D.; Camata, R.; Fedorov, V.; Mirov, S. Crystal field engineering of transition metal doped II-VI ternary and quaternary semiconductors for mid-IR tunable laser applications. *Opt. Mater. Express* **2015**, *5*, 2036–2046.

[140] Pradhan, N.; DasAdhikari, S.; Nag, A.; Sarma, D. D. Luminescence, Plasmonic, and Magnetic Properties of Doped Semiconductor Nanocrystals. *Angewandte Chemie International Edition* **2017**, *56*, 7038–7054.

[141] Patle, U. S.; Ahirwar, R. K.; Bhatt, A.; Arya, B. S. Enhanced photoluminescence properties of Mn doped CdS nanocrystals. *AIP Conference Proceedings* **2019**, *2100*, 020165.

[142] Žutić, I.; Fabian, J.; Das Sarma, S. Spintronics: Fundamentals and applications. *Rev. Mod. Phys.* **2004**, *76*, 323–410.

[143] Awschalom, D. D.; Flatté, M. E. Challenges for semiconductor spintronics. *Nature Physics* **2007**, *3*, 153–159.

[144] Dietl, T.; Ohno, H. Dilute ferromagnetic semiconductors: Physics and spintronic structures. *Rev. Mod. Phys.* **2014**, *86*, 187–251.

[145] Yun, J. H.; Kim, K. H.; Lee, D. Y.; Ahn, B. T. Back contact formation using Cu2Te as a Cu-doping source and as an electrode in CdTe solar cells. *Solar Energy Materials and Solar Cells* **2003**, *75*, 203–210.

[146] Tang, M.; He, B.; Dou, D.; Liu, Y.; Duan, J.; Zhao, Y.; Chen, H.; Tang, Q. Toward efficient and air-stable carbon-based all-inorganic perovskite solar cells through substituting CsPbBr3 films with transition metal ions. *Chemical Engineering Journal* **2019**, *375*, 121930.

[147] Biglari, B.; Samimi, M.; Hage-Ali, M.; Koebel, J.; Siffert, P. The interaction of copper with structural defects in THM grown cadmium telluride. *Nuclear Instruments and Methods in Physics Research Section A: Accelerators, Spectrometers, Detectors and Associated Equipment* **1989**, *283*, 249–254.

[148] von Windheim, J. A.; Cocivera, M. Variation of resistivity of copper-doped cadmium telluride prepared by electrodeposition. *Journal of Physics D: Applied Physics* **1990**, *23*, 581.

[149] Hossain, A.; Cui, Y.-g.; Bolotnikov, A.; Camarda, G.; Yang, G.; Kochanowska, D.; Witkowska-Baran, M.; Mycielski, A.; James, R. Vanadium-Doped Cadmium Manganese Telluride (Cd1- x Mn x Te) Crystals as X-and Gamma-Ray Detectors. *Journal of Electronic Materials* **2009**, *38*, 1593–1599.

[150] Perrenoud, J.; Kranz, L.; Gretener, C.; Pianezzi, F.; Nishiwaki, S.; Buecheler, S.; Tiwari, A. N. A comprehensive picture of Cu doping in CdTe solar cells. *Journal of Applied Physics* **2013**, *114*, 174505.

[151] Kranz, L. et al. Doping of polycrystalline CdTe for high-efficiency solar cells on flexible metal foil. *Nature Communications* **2013**, *4*, 2306.

[152] Kuciauskas, D.; Dippo, P.; Zhao, Z.; Cheng, L.; Kanevce, A.; Metzger, W. K.; Gloeckler, M. Recombination analysis in cadmium telluride photovoltaic solar cells with photoluminescence spectroscopy. *IEEE Journal of Photovoltaics* **2015**, *6*, 313–318.

[153] Başol, B. M.; McCandless, B. Brief review of cadmium telluride-based photovoltaic technologies. *Journal of photonics for Energy* **2014**, *4*, 040996.

[154] Burger, A.; Chattopadhyay, K.; Chen, H.; Ndap, J. O.; Ma, X.; Trivedi, S.; Kutcher, S. W.; Chen, R.; Rosemeier, R. D. Crystal growth, fabrication and evaluation of cadmium manganese telluride gamma ray detectors. *Journal of crystal growth* **1999**, *198*, 872–876.

[155] Adams, A. L.; Agbalagba, E. O.; Jow, J. O.; Mwathi, J. G.; Egarievwe, A. A.; Chan, W.; Dowdell, M. C.; Roy, U. N.; Egarievwe, S. U. Thermal annealing of CdMnTe material being developed for nuclear radiation detection applications. *IOSR Journal of Mechanical and Civil Engineering* **2016**, *13*, 1–5.

[156] Mycielski, A.; Wardak, A.; Kochanowska, D.; Witkowska-Baran, M.; Szot, M.; Jakieła, R.; Domagała, J. Z.; Kowalczyk, L.; Kochański, M.; Janusz, G., et al. CdTe-based crystals with Mg, Se, or Mn as materials for X and gamma ray detectors: Selected physical properties. *Progress in Crystal Growth and Characterization of Materials* **2021**, *67*, 100543.

[157] Egarievwe, S. U.; Lukosi, E. D.; James, R. B.; Roy, U. N.; Derby, J. J. Advances in CdMnTe Nuclear Radiation Detectors Development. 2018 IEEE Nuclear Science Symposium and Medical Imaging Conference Proceedings (NSS/MIC). 2018; pp 1–3.

[158] Brovko, A.; Ruzin, A. Study of material uniformity in high-resistivity Cd1-xZnxTe and Cd1-xMnxTe crystals. *Nuclear Instruments and Methods in Physics Research Section A: Accelerators, Spectrometers, Detectors and Associated Equipment* **2020**, *958*, 161996, Proceedings of the Vienna Conference on Instrumentation 2019.

[159] Brovko, A.; Rusian, P.; Chernyak, L.; Ruzin, A. High quality planar Cd1-xMnxTe room-temperature radiation detectors. *Applied Physics Letters* **2021**, *119*, 062103.

[160] Mirov, S.; Moskalev, I.; Fedorov, V.; Martyshkin, D.; Mirov, M.; Myoung, N. Mid-Infrared transition metal doped II-VI semiconductor lasers. Frontiers in Optics 2011/Laser Science XXVII. 2011; p LThA3.

[161] Trivedi, S.; Kutcher, S.; Wang, C.; Jagannathan, G.; Hömmerich, U.; Bluiett, A.; Turner, M.; Seo, J. T.; Schepler, K. L.; Schumm, B., et al. Transition metal doped cadmium manganese telluride: A new material for tunable mid-infrared lasing. *Journal of Electronic Materials* **2001**, *30*, 728–732.

[162] Sorokina, I. T. Cr2+-doped II–VI materials for lasers and nonlinear optics. *Optical Materials* **2004**, *26*, 395–412.

[163] Hömmerich, U.; Wu, X.; Davis, V.; Trivedi, S.; Grasza, K.; Chen, R.; Kutcher, S. Demonstration of room-temperature laser action at 2.5 μm from Cr 2+: Cd 0.85 Mn 0.15 Te. *Optics Letters* **1997**, *22*, 1180–1182.

[164] Podlipensky, A.; Shcherbitsky, V.; Demchuk, M.; Kuleshov, N.; Levchenko, V.; Yakimovich, V.; Girard, S.; Moncorgé, R. Cr2+:Cd0.55Mn0.45Te crystal as a new saturable absorber for 2 m lasers. *Optics Communications* **2001**, *192*, 65–68.

[165] Aikawa, S.; Yumoto, M.; Saitoh, T.; Wada, S. Mid-infrared tunable pulsed laser based on Cr2+-doped II–VI chalcogenide. *Journal of Crystal Growth* **2021**, *575*, 126341.

[166] Goryca, M.; Kazimierczuk, T.; Nawrocki, M.; Golnik, A.; Gaj, J. A.; Kossacki, P.; Wojnar, P.; Karczewski, G. Optical Manipulation of a Single Mn Spin in a CdTe-Based Quantum Dot. *Phys. Rev. Lett.* **2009**, *103*, 087401.

[167] Le Gall, C.; Besombes, L.; Boukari, H.; Kolodka, R.; Cibert, J.; Mariette, H. Optical Spin Orientation of a Single Manganese Atom in a Semiconductor Quantum Dot Using Quasiresonant Photoexcitation. *Phys. Rev. Lett.* **2009**, *102*, 127402.

[168] Munekata, H. Optical manipulation of coupled spins in magnetic semiconductor systems: A path toward spin optoelectronics. *Physica E: Low-dimensional Systems and Nanostructures* **2005**, *29*, 475–482, nanoPHYS'05.

[169] Hanson, R.; Awschalom, D. D. Coherent manipulation of single spins in semiconductors. *Nature* **2008**, *453*, 1043–1049.

[170] Wolf, S. A.; Awschalom, D. D.; Buhrman, R. A.; Daughton, J. M.; von Molnár, S.; Roukes, M. L.; Chtchelkanova, A. Y.; Treger, D. M. Spintronics: A Spin-Based Electronics Vision for the Future. *Science* **2001**, *294*, 1488–1495.

[171] Awschalom, D. D.; Flatté, M. E.; Samarth, N. Spintronics. *Scientific American* **2002**, *286*, 66–73.

[172] Awschalom, D. D.; Bassett, L. C.; Dzurak, A. S.; Hu, E. L.; Petta, J. R. Quantum spintronics: engineering and manipulating atom-like spins in semiconductors. *Science* **2013**, *339*, 1174–1179.

[173] Hirohata, A.; Yamada, K.; Nakatani, Y.; Prejbeanu, I.-L.; Diény, B.; Pirro, P.; Hillebrands, B. Review on spintronics: Principles and device applications. *Journal of Magnetism and Magnetic Materials* **2020**, *509*, 166711.

[174] Awschalom, D. D.; Hanson, R.; Wrachtrup, J.; Zhou, B. B. Quantum technologies with optically interfaced solid-state spins. *Nature Photonics* **2018**, *12*, 516–527.

[175] Narang, P.; Ciccarino, C. J.; Flick, J.; Englund, D. Quantum Materials with Atomic Precision: Artificial Atoms in Solids: Ab Initio Design, Control, and Integration of Single Photon Emitters in Artificial Quantum Materials. *Advanced Functional Materials* **2019**, *29*, 1904557.

[176] Gaj, J. A.; Kossut, J. *Introduction to the physics of diluted magnetic semiconductors*; Springer Science & Business Media, 2011; Vol. 144.

[177] Dietl, T. A ten-year perspective on dilute magnetic semiconductors and oxides. *Nature materials* **2010**, *9*, 965–974.

[178] Sato, K.; Bergqvist, L.; Kudrnovskỳ, J.; Dederichs, P. H.; Eriksson, O.; Turek, I.; Sanyal, B.; Bouzerar, G.; Katayama-Yoshida, H.; Dinh, V., et al. First-principles theory of dilute magnetic semiconductors. *Reviews of modern physics* **2010**, *82*, 1633.

[179] Theodoropoulou, N.; Hebard, A.; Overberg, M.; Abernathy, C.; Pearton, S.; Chu, S.; Wilson, R. Unconventional carrier-mediated ferromagnetism above room temperature in ion-implanted (Ga, Mn) P: C. *Physical Review Letters* **2002**, *89*, 107203.

[180] Calderon, M.; Sarma, S. D. Theory of carrier mediated ferromagnetism in dilute magnetic oxides. *Annals of Physics* **2007**, *322*, 2618–2634.

[181] Muralidharan, M.; Anbarasu, V.; Elaya Perumal, A.; Sivakumar, K. Carrier mediated ferromagnetism in Cr doped SrTiO3 compounds. *Journal of Materials Science: Materials in Electronics* **2015**, *26*, 6352–6365.

[182] Ando, K.; Saito, H.; Jin, Z.; Fukumura, T.; Kawasaki, M.; Matsumoto, Y.; Koinuma, H. Large magneto-optical effect in an oxide diluted magnetic semiconductor Zn 1- x Co x O. *Applied Physics Letters* **2001**, *78*, 2700–2702.

[183] Pacuski, W.; Ferrand, D.; Cibert, J.; Deparis, C.; Gaj, J. A.; Kossacki, P.; Morhain, C. Effect of the s, p- d exchange interaction on the excitons in Zn 1- x Co x O epilayers. *Physical Review B* **2006**, *73*, 035214.

[184] Pacheco, J. L.; Singh, M.; Perry, D. L.; Wendt, J. R.; Ten Eyck, G.; Manginell, R. P.; Pluym, T.; Luhman, D. R.; Lilly, M. P.; Carroll, M. S.; Bielejec, E. Ion implantation for deterministic single atom devices. *Review of Scientific Instruments* **2017**, *88*, 123301.

[185] Hundt, A.; Puls, J.; Henneberger, F. Spin properties of self-organized diluted magnetic Cd 1- x Mn x Se quantum dots. *Physical Review B* **2004**, *69*, 121309.

[186] Bacher, G.; Schömig, H.; Scheibner, M.; Forchel, A.; Maksimov, A.; Chernenko, A.; Dorozhkin, P.; Kulakovskii, V.; Kennedy, T.; Reinecke, T. Spin–spin interaction in magnetic semiconductor quantum dots. *Physica E: Low-dimensional Systems and Nanostructures* **2005**, *26*, 37–44.

[187] Ovartchaiyapong, P.; Lee, K. W.; Myers, B. A.; Jayich, A. C. B. Dynamic strain-mediated coupling of a single diamond spin to a mechanical resonator. *Nature Communications* **2014**, *5*, 4429.

[188] Taylor, J. M.; Cappellaro, P.; Childress, L.; Jiang, L.; Budker, D.; Hemmer, P. R.; Yacoby, A.; Walsworth, R.; Lukin, M. D. High-sensitivity diamond magnetometer with nanoscale resolution. *Nature Physics* **2008**, *4*, 810–816.

[189] Maze, J. R.; Stanwix, P. L.; Hodges, J. S.; Hong, S.; Taylor, J. M.; Cappellaro, P.; Jiang, L.; Dutt, M.; Togan, E.; Zibrov, A., et al. Nanoscale magnetic sensing with an individual electronic spin in diamond. *Nature* **2008**, *455*, 644–647.

[190] Toyli, D. M.; de Las Casas, C. F.; Christle, D. J.; Dobrovitski, V. V.; Awschalom, D. D. Fluorescence thermometry enhanced by the quantum coherence of single spins in diamond. *Proceedings of the National Academy of Sciences* **2013**, *110*, 8417–8421.

[191] Waldherr, G.; Wang, Y.; Zaiser, S.; Jamali, M.; Schulte-Herbrüggen, T.; Abe, H.; Ohshima, T.; Isoya, J.; Du, J.; Neumann, P., et al. Quantum error correction in a solid-state hybrid spin register. *Nature* **2014**, *506*, 204–207.

[192] Bäuerle, C.; Glattli, D. C.; Meunier, T.; Portier, F.; Roche, P.; Roulleau, P.; Takada, S.; Waintal, X. Coherent control of single electrons: a review of current progress. *Reports on Progress in Physics* **2018**, *81*, 056503.

[193] Nowack, K. C.; Koppens, F.; Nazarov, Y. V.; Vandersypen, L. Coherent control of a single electron spin with electric fields. *Science* **2007**, *318*, 1430–1433.

[194] Balasubramanian, G.; Neumann, P.; Twitchen, D.; Markham, M.; Kolesov, R.; Mizuochi, N.; Isoya, J.; Achard, J.; Beck, J.; Tissler, J., et al. Ultralong spin coherence time in isotopically engineered diamond. *Nature materials* **2009**, *8*, 383–387.

[195] Maurer, P. C.; Kucsko, G.; Latta, C.; Jiang, L.; Yao, N. Y.; Bennett, S. D.; Pastawski, F.; Hunger, D.; Chisholm, N.; Markham, M., et al. Room-temperature quantum bit memory exceeding one second. *Science* **2012**, *336*, 1283–1286.

[196] Zhang, G.; Cheng, Y.; Chou, J.-P.; Gali, A. Material platforms for defect qubits and single-photon emitters. *Applied Physics Reviews* **2020**, *7*, 031308.

[197] Oberbeck, L.; Curson, N.; Simmons, M.; Brenner, R.; Hamilton, A.; Schofield, S.; Clark, R. Encapsulation of phosphorus dopants in silicon for the fabrication of a quantum computer. *Applied physics letters* **2002**, *81*, 3197–3199.

[198] Morello, A.; Pla, J. J.; Zwanenburg, F. A.; Chan, K. W.; Tan, K. Y.; Huebl, H.; Möttönen, M.; Nugroho, C. D.; Yang, C.; Van Donkelaar, J. A., et al. Single-shot readout of an electron spin in silicon. *Nature* **2010**, *467*, 687–691.

[199] Zwanenburg, F. A.; Dzurak, A. S.; Morello, A.; Simmons, M. Y.; Hollenberg, L. C.; Klimeck, G.; Rogge, S.; Coppersmith, S. N.; Eriksson, M. A. Silicon quantum electronics. *Reviews of modern physics* **2013**, *85*, 961.

[200] Acosta, V.; Hemmer, P. Nitrogen-vacancy centers: Physics and applications. *MRS bulletin* **2013**, *38*, 127–130.

[201] Lafuente-Sampietro, A.; Boukari, H.; Besombes, L. Resonant photoluminescence and dynamics of a hybrid Mn hole spin in a positively charged magnetic quantum dot. *Phys. Rev. B* **2017**, *95*, 245308.

[202] Léger, Y.; Besombes, L.; Maingault, L.; Mariette, H. Valence-band mixing in neutral, charged, and Mn-doped self-assembled quantum dots. *Phys. Rev. B* **2007**, *76*, 045331.

[203] Tiwari, V. Contrôle optique et dynamique de spin d'un Cr individuel dans un semi-conducteur : vers un contrôle cohérent mécanique avec des ondes acoustiques de surface. Ph.D. thesis, 2021; Thèse de doctorat dirigée par Besombes, Lucien et Boukari, Hervé Nanophysique Université Grenoble Alpes 2021.

[204] Lee, D.; Lee, K. W.; Cady, J. V.; Ovartchaiyapong, P.; Jayich, A. C. B. Topical review: spins and mechanics in diamond. *Journal of Optics* **2017**, *19*, 033001.

[205] Golter, D. A.; Oo, T.; Amezcua, M.; Stewart, K. A.; Wang, H. Optomechanical quantum control of a nitrogen-vacancy center in diamond. *Physical review letters* **2016**, *116*, 143602.

[206] Satzinger, K. J.; Zhong, Y.; Chang, H.-S.; Peairs, G. A.; Bienfait, A.; Chou, M.-H.; Cleland, A.; Conner, C. R.; Dumur, É.; Grebel, J., et al. Quantum control of surface acoustic-wave phonons. *Nature* **2018**, *563*, 661–665.

[207] Lafuente-Sampietro, A.; Boukari, H.; Besombes, L. Strain-induced coherent dynamics of coupled carriers and Mn spins in a quantum dot. *Phys. Rev. B* **2015**, *92*, 081305.

[208] Kolkowitz, S.; Bleszynski Jayich, A. C.; Unterreithmeier, Q. P.; Bennett, S. D.; Rabl, P.; Harris, J.; Lukin, M. D. Coherent sensing of a mechanical resonator with a single-spin qubit. *Science* **2012**, *335*, 1603–1606.

[209] Lafuente-Sampietro, A.; Utsumi, H.; Boukari, H.; Kuroda, S.; Besombes, L. Resonant optical control of the spin of a single Cr atom in a quantum dot. *Phys. Rev. B* **2017**, *95*, 035303.

[210] Tiwari, V.; Makita, K.; Arino, M.; Morita, M.; Kuroda, S.; Boukari, H.; Besombes, L. Influence of nonequilibrium phonons on the spin dynamics of a single Cr atom. *Phys. Rev. B* **2020**, *101*, 035305.

[211] Chen, I.; Kikuchi, C.; Watanabe, H. Superhyperfine structures in ESR and ENDOR of cubic CdTe: Mn2+. *The Journal of Chemical Physics* **1965**, *42*, 189–195.

[212] Vallin, J.; Watkins, G. EPR of Cr 2+ in II-VI lattices. *Physical Review B* **1974**, *9*, 2051.

[213] Ludwig, G.; Lorenz, M. Paramagnetic resonance of chromium in CdTe. *Physical Review* **1963**, *131*, 601.

[214] Smith, L.; Wolverson, D.; Bingham, S.; Davies, J. Electron paramagnetic resonance of Mn2+ ions in CdTe detected by coherent Raman spectroscopy. *physica status solidi (b)* **2006**, *243*, 892–896.

[215] Li, D.-H.; Li, F.-Z.; Zhou, Y.-Y. EPR parameters of Cr2+ ions in semiconductors CdS and CdTe. *Solid state communications* **1998**, *105*, 59–63.

[216] Bhattacharyya, S.; Zitoun, D.; Gedanken, A. Magnetic properties of Cd1- xMnxTe/C nanocrystals. *Nanotechnology* **2011**, *22*, 075703.

[217] Willardson, R. K.; Beer, A. C. *Semiconductors and semimetals*; Academic press, 1977.

[218] Vallin, J. T.; Slack, G. A.; Roberts, S.; Hughes, A. E. Infrared Absorption in Some II-VI Compounds Doped with Cr. *Phys. Rev. B* **1970**, *2*, 4313–4333.

[219] Shayesteh, S. F.; Hidari, M.; Parker, T. J. Far Infrared Characterization of Semimagnetic Semiconductor CdTe-Cd1xMnxTe Multi Quantum Wells. 2006 Joint 31st International Conference on Infrared Millimeter Waves and 14th International Conference on Teraherz Electronics. 2006; pp 365–365.

[220] Pekarek, T.; Miotkowski, I.; Crooker, B. Magnetic measurements on Cd1- x Cr x Te and Zn1- x Cr x Te. *Journal of applied physics* **1996**, *79*, 6436–6438.

[221] Fernández-Rossier, J.; Aguado, R. Mn-doped II-VI quantum dots: artificial molecular magnets. *physica status solidi c* **2006**, *3*, 3734–3739.

[222] Lu, X.; Tsoi, S.; Miotkowski, I.; Rodriguez, S.; Ramdas, A.; Alawadhi, H. Raman electron paramagnetic resonance in Zn 1- x Cr x Te and Cd 1- x Cr x Te. *Physical Review B* **2007**, *75*, 155206.

[223] Li, T.; Lozykowski, H.; Reno, J. L. Optical properties of CdTe/Cd 1- x Zn x Te strained-layer single quantum wells. *Physical Review B* **1992**, *46*, 6961.

[224] Cieplak, M.; Godlewski, M.; Baranowski, J. Optical Charge Transfer Spectra and EPR Spectra of Cr2+ (d4) and Cr1+ (d5) in CdTe. *physica status solidi (b)* **1975**, *70*, 323–331.

[225] Godlewski, M.; Baranowski, J. EPR measurements of chromium impurity photoionization transitions in CdTe. *physica status solidi (b)* **1980**, *97*, 281–287.

[226] Tiwari, V.; Arino, M.; Gupta, S.; Morita, M.; Inoue, T.; Caliste, D.; Pochet, P.; Boukari, H.; Kuroda, S.; Besombes, L. Hole-Cr^{+} nanomagnet in a semiconductor quantum dot. *Phys. Rev. B* **2021**, *104*, L041301.

[227] Woodbury, H.; Ludwig, G. Spin resonance of transition metals in silicon. *Physical review* **1960**, *117*, 102.

[228] Ludwig, G.; Woodbury, H. *Solid State Physics*; Elsevier, 1962; Vol. 13; pp 223–304.

[229] Ludwig, G.; Woodbury, H. Electronic structure of transition metal ions in a tetrahedral lattice. *Physical Review Letters* **1960**, *5*, 98.

[230] DeLeo, G. G.; Watkins, G. D.; Fowler, W. B. Level positions of interstitial transition-metal impurities in silicon. *Phys. Rev. B* **1982**, *25*, 4972–4980.

[231] Köppel, H.; Yarkony, D. R.; Barentzen, H. *The Jahn-Teller Effect: Fundamentals and Implications for Physics and Chemistry*; Springer Science & Business Media, 2009; Vol. 97.

[232] Mizokawa, T.; Fujimori, A. p- d exchange interaction for 3 d transition-metal impurities in II-VI semiconductors. *Physical Review B* **1997**, *56*, 6669.

[233] Zhang, Z.; Partoens, B.; Chang, K.; Peeters, F. First-principles study of transition metal impurities in Si. *Physical Review B* **2008**, *77*, 155201.

[234] Picoli, G.; Chomette, A.; Lannoo, M. Renormalized-defect-molecule approach to the theory of substitutional transition-metal ions in semiconductors. *Physical Review B* **1984**, *30*, 7138.

[235] Beeler, F.; Andersen, O.; Scheffler, M. Electronic and magnetic structure of 3d–transition-metal point defects in silicon calculated from first principles. *Physical Review B* **1990**, *41*, 1603.

[236] Kugel, K. I.; Khomskiĭ, D. The Jahn-Teller effect and magnetism: transition metal compounds. *Soviet Physics Uspekhi* **1982**, *25*, 231.

[237] Herrero-Saboya, G.; Martin-Samos, L.; Richard, N.; Hémeryck, A. Common defects in diamond lattices as instances of the general T(e+ t 2) Jahn-Teller effect. *Physical Review Materials* **2022**, *6*, 034601.

[238] Wang, Y.; Zhang, R.; Li, J.; Li, L.; Lin, S. First-principles study on transition metal-doped anatase TiO2. *Nanoscale research letters* **2014**, *9*, 1–8.

[239] Heald, S. M. In *X-Ray Absorption Spectroscopy of Semiconductors*; Schnohr, C. S., Ridgway, M. C., Eds.; Springer Berlin Heidelberg: Berlin, Heidelberg, 2015; pp 339–353.

[240] Kobayashi, M.; Ishida, Y.; Hwang, J.; Song, G.; Fujimori, A.; Yang, C.; Lee, L.; Lin, H.; Huang, D.; Chen, C., et al. Local electronic structure of Cr in the II–VI diluted ferromagnetic semiconductor Zn1-xCrxTe. *New Journal of Physics* **2008**, *10*, 055011.

[241] Hwang, Y.; Shen, S.; Liu, X.; Furdyna, J.; Dobrowolska, M.; Um, Y. Room-temperature ferromagnetism in highly Cr-doped II-Mn-VI magnetic semiconductor Cd 1- x- y Mn x Cr y Te. *Physical Review B* **2013**, *88*, 075205.

[242] Larson, P.; Satpathy, S. Effect of vacancies on ferromagnetism in GaN: Mn dilute magnetic semiconductors from first-principles. *Physical Review B* **2007**, *76*, 245205.

[243] Xue-Chao, L.; Hua-Wei, Z.; Tao, Z.; Bo-Yuan, C.; Zhi-Zhan, C.; Li-Xin, S.; Er-Wei, S. Magnetic properties of Mn-doped ZnO diluted magnetic semiconductors. *Chinese Physics B* **2008**, *17*, 1371.

[244] Zhang, Z.; Schwingenschlögl, U.; Roqan, I. S. Vacancy complexes induce long-range ferromagnetism in GaN. *Journal of Applied Physics* **2014**, *116*, 183905.

[245] Pemmaraju, C.; Hanafin, R.; Archer, T.; Braun, H.; Sanvito, S. Impurity-ion pair induced high-temperature ferromagnetism in Co-doped ZnO. *Physical Review B* **2008**, *78*, 054428.

[246] Hu, L.; Huang, J.; He, H.; Zhu, L.; Liu, S.; Jin, Y.; Sun, L.; Ye, Z. Dual-donor (Zn i and VO) mediated ferromagnetism in copper-doped ZnO micron-scale polycrystalline films: a thermally driven defect modulation process. *Nanoscale* **2013**, *5*, 3918–3930.

[247] Kuroda, S.; Nishizawa, N.; Takita, K.; Mitome, M.; Bando, Y.; Osuch, K.; Dietl, T. Origin and control of high-temperature ferromagnetism in semiconductors. *Nature materials* **2007**, *6*, 440–446.

[248] Raebiger, H.; Nakayama, H.; Fujita, T. Control of defect binding and magnetic interaction energies in dilute magnetic semiconductors by charge state manipulation. *Journal of Applied Physics* **2014**, *115*, 012008.

[249] Gallino, F.; Di Valentin, C. Copper impurities in bulk ZnO: A hybrid density functional study. *The Journal of chemical physics* **2011**, *134*, 144506.

[250] Wickramaratne, D.; Shen, J.-X.; Dreyer, C. E.; Alkauskas, A.; Van de Walle, C. G. Electrical and optical properties of iron in GaN, AlN, and InN. *Physical Review B* **2019**, *99*, 205202.

[251] Xing, H.-Y.; Chen, Y.; Ji, C.; Jiang, S.-X.; Yuan, M.-Y.; Guo, Z.-Y.; Li, K.; Cui, M.-Q.; Zhang, G.-Y. Role of vacancy-type defects in magnetism of GaMnN. *Chinese Physics B* **2016**, *25*, 067503.

[252] Solodin, S.; Panchuk, O.; Fochuk, P. Quasi-chemical analysis of point defect structure n Mn-doped CdTe single crystals. *Journal of Physics and Chemistry of Solids* **2020**, *138*, 109290.

[253] Roehl, J.; Khare, S. Diffusion of Cd vacancy and interstitials of Cd, Cu, Ag, Au and Mo in CdTe: A first principles investigation. *Solar Energy* **2014**, *101*, 245–253.

[254] Solodin, S.; Resch, L.; Klinser, G.; Sprengel, W.; Nykoniuk, Y.; Zakharuk, Z.; Panchuk, O.; Fochuk, P.; James, R. Study of point defects in CdTe:Mn crystals by electrical measurements supported by positron lifetime spectroscopy. 2018 IEEE Nuclear Science Symposium and Medical Imaging Conference Proceedings (NSS/MIC). 2018; pp 1–5.

[255] Lu, X.; Tsoi, S.; Miotkowski, I.; Rodriguez, S.; Ramdas, A.; Alawadhi, H. Raman electron paramagnetic resonance in Zn 1- x Cr x Te and Cd 1- x Cr x Te. *Physical Review B* **2007**, *75*, 155206.

Publications

- Selva Chandrasekaran Selvaraj, Sameer Gupta, Damien Caliste, and Pascal Pochet , "Passivation mechanism in CdTe solar cells: The hybrid role of Se", Appl. Phys. Lett. **119**, 062105 (2021)
- V. Tiwari, M. Arino, S. Gupta, M. Morita, T. Inoue, D. Caliste, P. Pochet, H. Boukari, S. Kuroda, and L. Besombes, "Hole- Cr+ nanomagnet in a semiconductor quantum dot", Phys. Rev. B **104**, L041301 (2021)